ABSTRACT

Title of Document: SELF-ASSEMBLY OF INORGANIC NANOPARTICLE AMPHIPHILES FOR BIOMEDICAL APPLICATIONS

Yijing Liu, Doctor of Philosophy, 2015

Directed By: Professor Zhihong Nie,
Department of Chemistry and Biochemistry

Ensembles of interacting nanoparticles (NPs) can exhibit novel collective properties ─ arising from the coupling between NPs ─ that can be radically different from individuals. Realizing the enormous potential of NPs in biomedical applications requires the organization of NPs into hierarchically ordered structures. My dissertation is focused on the design of NP amphiphiles (NPAMs) and the use of NPAMs as building blocks to construct polymer-inorganic hybrid materials. The NPAMs are made from NPs surface-grafted with amphiphilic block copolymers (BCPs). In this way, the NPAMs synergistically combine the properties of both inorganic NPs and grafted BCPs, such as optical and magnetic properties of NPs, and flexibility of BCPs.

First, we demonstrated that NPAMs with relatively low polymer ligand densities (~0.03 chain/nm^2) self-assembled into vesicular nanostructures composed of a single layer of NP chains in the membrane. The decrease in the interparticle distance between NPAMs in the chain vesicles led to strong plasmon coupling of NPs and hence enhanced efficiency in photoacoustic imaging.

Second, we fabricated hybrid vesicles with well-defined shapes and surface patterns by co-assembling amphiphilic BCPs and NPAMs, which include Janus-like vesicles (JVs) with different shapes, patchy vesicles, and homogeneous vesicles.

Third, we prepared magneto-plasmonic hybrid vesicles with various structures through concurrent self-assembly of NPAMs, free BCPs, and hydrophobic magnetic NPs. The hybrid vesicles were demonstrated for both light-triggered release of payload and magnetic resonance imaging. Particularly, the magnetic manipulation of vesicles to specific location can be used to enhance the photothermal effect of the vesicles in cancer imaging and therapy.

Finally, we reported that the use of a microfluidic flow-focusing device for the self-assembly of JVs that can act as vesicular motors. The vesicles can be used to encapsulate active compounds, and the release of this payload can be effected using near-infrared light.

This systematic study will help us gain deeper understanding of the self-assembly of NPAMs into controllable nanostructures and control the collective properties of NP ensembles for various applications. This research will also provide new insights into the fundamental questions that must be overcome before the hybrid materials can be utilized in effective cancer imaging and treatment.

SELF-ASSEMBLY OF INORGANIC NANOPARTICLE AMPHIPHILES FOR BIOMEDICAL APPLICATIONS

By

Yijing Liu

Dissertation submitted to the Faculty of the Graduate School of the
University of Maryland, College Park, in partial fulfillment
of the requirements for the degree of
Doctor of Philosophy
2015

Advisory Committee:
Professor Zhihong Nie, Chair
Professor Janice Reutt-Robey
Professor Yuhuang Wang
Professor Paul Paukstelis
Professor Srinivasa R Raghavan, Dean's representative

Dedication

To my parents and my wife

Acknowledgements

This work was made possible by the support of many people. I'd like to express my sincere appreciation to all of them

My deepest gratitude must go to my advisor Dr. Zhihong Nie. He led me into the world of nanotechnology. Without his invaluable advices, careful guidance and continuous support in my PhD study, I would be able to get here. His professionalism, expertise, and his enthusiasm towards science set a good example for me to follow in the future. I sincerely appreciate for everything Dr. Nie has done for me.

I would also like to thank Dr. Xiaoyuan Chen for leading me into field of biomedical research. His guidance, support, and helpful conversations gave me a lot inspirations on my future career.

I also wish to thank all of the members in Dr. Nie's group for their valuable discussions on my research and bringing me a lot of joyful moments in my graduate study. Especially, I would like to thank Dr. Jie He who mentored me when I joined the group. He gave enormous suggestions, and help to me for academics, and also for normal life. I would like to thank Maria Teresa Perez who joined our group with me together. She is a good friend and helps me a lot to get used to the graduate life in the USA. I would like to thank Zhiqi Huang for his help on TEM characterizations. I would like to thank Dr. Lei Wang for his help on experiments with microfluidics. I am grateful to Matt J. Hourwitz's help on experiments with laser. I would like to thank Dr. Chenglin Yi for his help with polymer synthesis. I appreciate Marcus Carter and Dr. Yang Yang for their help with my writing.

I would also like to thank all the group members in Dr. Chen's group. I learned a lot from them and they offered me many valuable suggestions. Especially, I would like to thank Dr. Xinglu Huang, Dr. Liming Nie, Dr. Xiaolian Sun, and Xiangyu Yang for their contributions to our research projects.

I also got a lot help from outside group on my research. I would like to thank Dr. Xin Zhang for helping me with microtoming and Wonseok Hwang for GPC measurement. I would like to thank Dr. Yanchun Li's help on modeling. I would like to thank our nanocenter for helping me with SEM and TEM characterizations.

I would also like to thank Professor Yuhuang Wang, Professor Janice Reutt-Robey, Professor Paul Paukstelis, and Professor Srinivasa R. Raghavan to serve on my committee and their support, guidance, and helpful suggestions.

Financially, this research was supported by many sources which I would like to thank. Most of research was supported by the NSF Career Award (DMR-1255377) and startup funds. In addition, I acknowledge support from following fellowships: Millard & Lee Alexander Fellowship, Merit Fellowships, Ann G Wylie Dissertation Fellowship, Jacob K. Goldhaber travel grant, and NIH pre-doctoral research fellowship.

Last but not least, I would like to thank my family for all their deepest love and endless support. I am indebted to my parents for bringing me up and their continuous support. Thanks goes to my wife Siqi Chen for her positive encouragement and selfless support at the lowest point of my life. I could not have finished this piece of work without their love, patience and friendship.

Table of Contents

List of Figures

List of Tables

List of Abbreviations

1 D	One dimensional
AFM	Atomic force microscopy
AgNP	Silver nanoparticle
AIBN	Azobis(isobutyronitrile)
AuNB	Gold nanodumbells
AuNP	Gold nanoparticle
AuNR	Gold nanorods
AuNW	Au nanowires
BCPs	Blockcopolymers
CPPA	4-cyano-4-(phenylcarbonothioylthio) pentanoic acid
CTAB	Hexadecyltrimethylammonium bromide
Cryo-TEM	Cryogenic TEM
CW	Continuous waveform
DLS	Dynamic light scattering
DMF	N,N-Dimethylformamide
DPD	Dissipative particle dynamics
D_{emt}	Effect membrane thickness
EDX	Energy dispersive X-ray spectrometry
FEG	Field-emission gun
FITC	Fluorescein isothiocyanate
GPC	Gel permeation chromatography
$HAuCl_4$	Gold(III) chloride trihydrate

HVs	Homogeneous vesicles
JSVs	Janus spherical vesicles
JHVs	Janus hemispherical vesicles
JVs	Janus-like vesicles
LSPR	Localized surface plasmon resonance
MAM	Molecular amphiphile
MNP	Iron oxide nanoparticle
NIR	Near-infrared
NPs	Nanoparticles
NaOL	Sodium oleate
NPAM	Nanoparticle amphiphile
$NaBH_4$	Sodium borohydride
PA	Photoacoustic
PAA	Poly(acrylic acid)
PVA	Poly(vinyl alcohol)
PMMA	Poly(methyl methacrylate)
P(LAMP)-co-(GMA)	Poly(lipoic acid 2-hydroxy-3-(methacryloyloxy)-propyl ester-co-glycidyl methacrylate)
$PEMO_2MA$	Poly(2(2-methoxyethoxy)ethyl methacrylate)
P4VP	Poly(4-vinylpyridine)
PC	Phosphatidylcholine
PEO	Poly ethylene glycol
PDP	Pentadecylphenol

PVs	Patchy vesicles
PS	Polystyrene
QD	Quantum dots
RAFT	Reversible addition-fragmentation chain transfer
SEM	Scanning electron microscope
TGA	Thermal gravimetric analysis
THF	Tetrahydrofuran
TEM	Transmission electron microscope
μFFD	Microfluidic flow-focusing device

Chapter 1: Introduction

Part of this chapter is adapted from the manuscript published in the following article: Liu, Y.; Liu, B.; Nie, Z., Concurrent self-assembly of amphiphiles into nanoarchitectures with increasing complexity, *Nano Today*, **2015**, 136, 2602-2610.

Self-assembly refers to the spontaneous organization of small building blocks, such as molecules and colloid particles, into larger or ordered structures without external intervention.[1] This phenomenon is extraordinarily common in nature, as it is observed from the smallest structure, such as virus, to big plants, such as trees.[2] The formation of basic components of life (*e.g.*, DNA, RNA, protein, and cells) is also involved with self-assembly, which results from the delicate balance of non-covalent interactions among biomolecules. These facts reveal nature's powerful ability to build things with substantial structural diversity and stimulate our interest in understanding the principles underlying self-assembly. Inspired by nature, the fabrication of complex nanoscale structures or structures with larger dimensions through self-assembly is a promising research direction. Compared to top-down methods such as photo- lithography, self-assembly is a simple yet versatile bottom-up approach to create complex nano- or micro-sized materials with high efficiency. With the rapid development of nanotechnology, researchers have become increasingly fascinated by the nanoscale world, where distinct size-dependent properties lead to ongoing revolution in technologies in the fields of medicine, electronics, and catalysts.[3] Due to the tremendous progress in colloidal particle synthesis, researchers have access to a huge library of colloidal particles as assembly building blocks. The organization of these colloidal particles into desired structures remains a challenge to be solved.

Therefore, It is important to design new self-assembly systems and understand fundamentals behind the assembly, in order to meet the rising demand for advanced materials.

1.1 Molecular self-assembly

Understanding the principles of molecular self-assembly is the foundation for studying more complex assembly systems. There are plenty of examples of molecular self-assembly. For instance, multiple types of phospholipids self-assemble into lipid bilayers which form the basis of cell membranes. Detergents, of which most components are surfactants, are able to form micelles or stabilize gas bubbles when they are used in washing. These molecules, which have a hydrophilic head and one or more hydrophobic tails,[4-6] are called molecular amphiphiles (MAMs) and their assembly have been studied for decades. The amphiphilic nature of these molecules enables their self-assembly into a wide range of nanostructures, such as vesicles, micelles with different shapes (*e.g.*, rods, disks, branched chains), and bicontinuous sponge-like structures. The formation of structures with various morphologies can be semi-quantitatively described by the simple geometric property of molecules, *i.e.*, the packing parameter of amphiphiles. The packing parameter (p) is defined as $p = v/a_o l_c$, where v is the volume of the hydrophobic segment, a_o is the cross-sectional area of the head group, and l_c is the length of the hydrophobic segment. In general, the morphologies are spheres when p is less than 1/3; cylinders when $1/3 < p < 1/2$; flexible lamellae or vesicles when $1/2 < p < 1$; and planar lamellae when $p = 1$. If p is

larger than 1, inverted structures can be obtained.[7-9]

1.1.1. Self-assembly of block copolymers (BCPs)

Amphiphilic BCPs, in which hydrophobic and hydrophilic polymer blocks are covalently linked to each other, is one type of MAMs with higher molecular weight. Figure 1.1 is a schematic illustration of the structures of BCPs consist of two different blocks.[10]

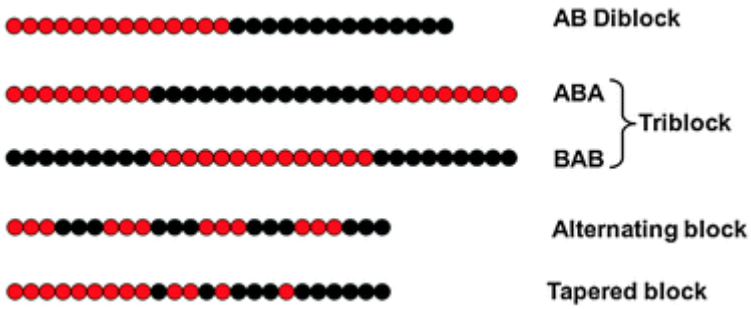

Figure 1.1 Schematic illustration of BCP structures containing two types of blocks (A and B).[10] Reproduced from Ref. [10] with permission of The Royal Society of Chemistry

The self-assembly of amphiphilic BCPs in selective solvents generates assemblies with a variety of morphologies including, but not limited to, spherical micelles, cylindrical micelles, and vesicular micelles (Figure 1.2).[11] Similar to lipids or surfactants, the formation of the different assembled structures can also be related to the packing parameters, which determines the thermodynamic parameters introduced below. Thanks to the advances in the polymerization techniques, BCPs with significant chemical and structural diversity have been synthesized.[12] In

addition, the flexibility and deformability of BCP chains enable them to assembly into complex structures that cannot be obtained from lipid or surfactants, such as helix chains.

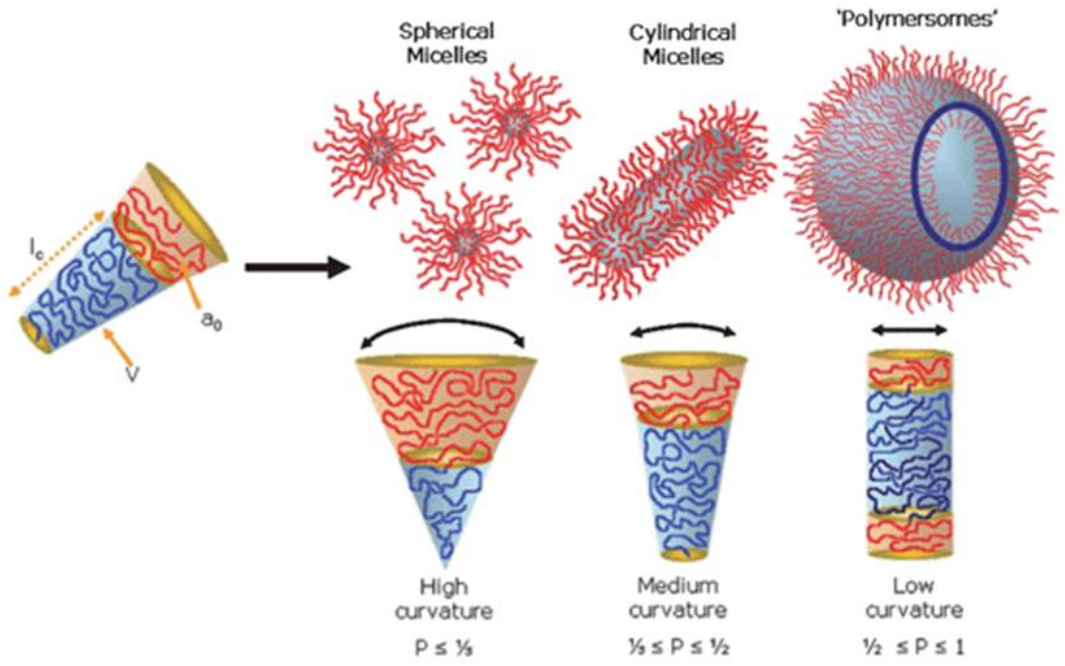

Figure 1.2. Schematic illustration of self-assembling of amphiphilic BCPs into spherical micelles, cylindrical micelles, and vesicles according to their packing parameter.[9] Reproduced from Ref. [9] with permission of The Royal Society of Chemistry

1.1.2 The definition of hydrophobicity and the origin of hydrophobic interaction

Self-assembly of BCPs is an interplay of different non-covalent interactions, including hydrophobic interactions, van der Waals interactions, and electrostatic interactions.[10,13] In terms of self-assembly of amphiphilic BCPs, the most important

interaction is the hydrophobic interaction. The term “hydrophobicity” refers to the reluctance of nonpolar chemicals to interact with water.[14] The literal meaning of hydrophobicity (the fear of water) is misleading. The van der Waals interactions between water molecules and hydrocarbon solutes are actually favorable as a result of the caging of the solute molecules by water molecules. In a more precise manner, hydrophobicity can be defined as a positive change in Gibbs free energy when a substance is transferred from a nonpolar solvent to water.[15] Both enthalpy and entropy contribute to the positive change in free energy. Once hydrocarbon solutes are in contact with water molecules, the hydrocarbon solutes will interrupt the hydrogen bonding between water molecules. The water molecules prefer to maintain as many hydrogen bonds as possible, thus leading to the reorganization of water molecules into water cages surrounding the solute molecules. This process is accompanied with a negative change in entropy, due to the local organization of water molecules, which gives us an overall positive change in free energy. Due to the hydrophobicity of hydrocarbon solutes, the dispersion of hydrocarbon solutes in water is not stable. The hydrocarbon solutes in water will aggregate to lower the free energy, driven by the hydrophobic interaction.[16] The aggregation of hydrocarbon molecules in water will release water molecules to the environment since less water molecules will be needed to form the cages (Figure 1.3). Therefore, the net entropy change will be favorable because of the increase in free water molecules. On the other hand, the enthalpy change during aggregation can be either positive or negative; however, entropy still plays a dominant role in forming aggregates. This explains the

hydrophobic interactions, in general.

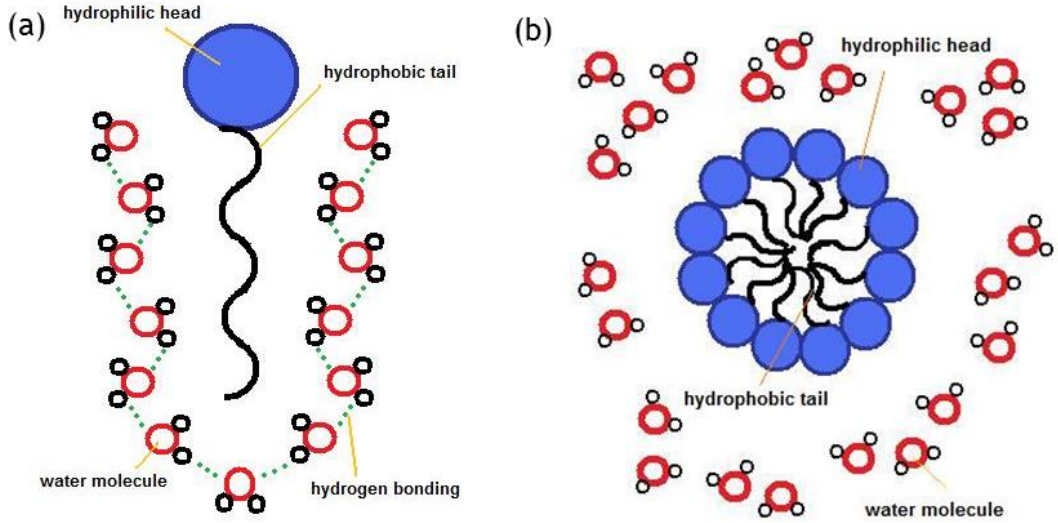

Figure 1.3. The schematic illustration of self-assembly of surfactants triggered by hydrophobic interactions.[17,18] Licence: https://creativecommons.org/licenses/by-sa/3.0/legalcode

1.1.3 Thermodynamics of the self-assembly of amphiphiles

The hydrophobic interaction is the driving force for micellization of amphiphiles.[19] Micellization of BCPs is a prime example that illustrates this process. The self-assembly of amphiphilic BCPs in selective solvents generates assemblies with morphologies such as, spherical micelles, cylindrical micelles, and vesicular micelles.[11] The formation of micelles with different morphologies is determined by the free energy of micellization, which consists of three parts: the free energy of the hydrophobic core(G_{core}); the interfacial free energy between the hydrophobic part

and the solvent ($G_{interface}$); and the free energy of the corona (G_{corona}).[20]

Taking a spherical micelle of BCPs as an example, a spherical micelle contains a hydrophobic core that is stabilized by a hydrophilic corona. The three key parameters that affect the three free energy components (*i.e.* G_{core}, $G_{interface}$, G_{corona}) are the radius of the micelle core (R_{core}), the degree of stretching of the core-forming block compared to its unperturbed state (S_c), and the area per corona chain (A_c).[11] G_{core} of a spherical micelle is mainly determined by S_c and $\mathrm{R_{core}}$. S_c is defined as the ratio of the $\mathrm{R_{core}}$ to the end-to-end distance of the core-forming polymer. A higher value of S_c or $\mathrm{R_{core}}$ indicates a higher G_{core}. Inside the core of a structure, some of the core-forming polymers have to span the distance from the core center to the edge, which is entropically unfavorable. $G_{interface}$ and G_{corona} *are* mainly determined *by the* A_c. A smaller value of A_c indicates less contact between the hydrophobic core and the solvent, resulting in a lower $G_{interface}$. However, as Ac decreases in value, the steric repulsion among hydrophilic chains increases, thus increasing G_{corona}.

When the assembled morphology changes from a spherical micelle to a cylindrical micelle, and to a vesicular micelle, both A_c *and* S_c decrease.[10] Let us assume the thickness of the hydrophobic wall of a vesicular micelle is comparable to the radius of a micelle core. Comparing vesicular micelles with spherical micelles, vesicular micelles have a lower value of S_c. Since the hydrophobic membrane of a vesicular micelle is made of a bilayer of polymers, the polymers only span half the distance from the center of the membrane to the interface, as compared to the a

spherical micelle. On the other hand, A_c of a spherical micelle is smaller than a vesicular micelle. For a spherical micelle, A_c is given by

$$A_c = 4\pi R_{\mathrm{core}}^2/\mathrm{N}_{agg} = 4\pi R_{\mathrm{core}}^2/(\frac{\frac{4}{3}\pi R_{core}^3}{V_s N_{core}}) = 3V_s N_{core}/R_{core} \qquad \text{(Eq. 1.1)}$$

where N_{agg}, V_s , and N_{core} represent the aggregation number of BCPs per micelle, volume per repeat unit of hydrophobic block, and the degree of polymerization of the hydrophobic block, respectively. As indicated in the equation above, $\mathrm{A_c}$ is proportional to $3/R_{core}$. Similarly, A_c of a vesicular micelle is proportional to $1/R_{core}$ (where R_{core} is half of hydrophobic thickness) due to the geometrical effect on the volume of hydrophobic part.[11] Thus, spherical micelles have a lower value of A_c than vesicular micelles. This demonstrates that BCPs in selective solvents can balance different parts of free energy by changing $\mathrm{R_{core}}$, A_c and S_c to form the most stable structures.

From a thermodynamic point of view, the tendency of increasing the radius of cores to form spherical micelles is favorable because it lowers $G_{interface}$ by minimizing the overall interfacial area between solvent and hydrophobic core. The radius of cores can't grow indefinitely because of its tendency towards growth is balanced by the positive change in G_{core} and G_{corona} due to the increased value of S_c, and stronger steric repulsion among hydrophilic corona chains, respectively. This balance can be broken if the reaction conditions are changed (*e.g.* solution conditions). Therefore, the most thermodynamically stable structure will change from

spherical micelles to other morphologies, such as vesicular micelles.

1.1.4 The control over self-assembly morphologies

The parameters (R_{core}, A_c and S_c) depend on the composition of BCPs (*e.g.*, chain length of each block), or the solution conditions (*e.g.*, type of common solvent to dissolve BCPs). The morphologies of assemblies can be tuned by varying these conditions.[10]

1.1.5 The effect of chain length on self-assembly morphologies

Let us define l as the hydrophilic chain length in BCPs and assume that the hydrophobic chain length of BCPs is constant. BCPs with a longer l form spherical micelles, where corona chains are crowded, resulting in stronger steric repulsion among corona chains and a smaller core dimension. In this case, $G_{interface}$ *and* G_{corona} dominate the free energy of micellization, and G_{core} becomes less important compared to G_{corona} since a smaller dimension of core indicates weaker S_c. The large G_{corona} is mainly balanced by the tendency of minimizing $G_{interface}$. When l decreases, transitional morphologies like cylindrical micelles start to appear. If l decreases further, spherical vesicles or other assembled morphologies form. In this case, G_{corona} decreases because the steric repulsion among hydrophilic chains becomes weaker, and $G_{interface}$ *and* G_{core} dominate the free energy of micellization. Hence, amphiphilic BCPs with different l adapt to different morphologies in selective solvents to minimize overall free energy.

1.1.6 The effect of common solvent on self-assembly morphologies

The interaction between solvent and polymer can change the parameters (R_{core}, A_c *and* S_c) associated with free energy.[20] The interaction between a hydrophobic polymer and a good solvent, such as tetrahydrofuran (THF) and N,N-dimethylformamide (DMF), can be evaluated by using solubility parameters (δ). In a good solvent, the polymer chains will adopt their conformations to maximize the interactions between polymers and the solvent As the difference between the values of δ for two species decrease, the strength of the interaction between the two species increase.[21] For example, poly(acrylic acid)-block-polystyrene (PAA_{390}-*b*-PS_{41}) form spherical micelles in DMF, but vesicular micelles in THF. The δ of PS, THF, and DMF are 16.6-20.2, 18.6, and 24.8, respectively. PS has stronger interaction with THF than with DMF leading to a higher mobility of the PS chains in THF, and a significant swelling of the hydrocarbon core. Therefore, the size of the micelles of PAA-*b*-PS in THF is bigger than that in DMF. Bigger micelles have stronger S_c, leading to a higher G_{core}. If the difference in the overall free energy is sufficient to overcome the energy barriers between different morphological states, then morphological transition will occur.

1.2 Self-assembly of inorganic nanoparticles

The developments in nanotechnology have witnessed the shift of general interest from preparation of individual component nanoparticles (NPs) to controllable assemblies to meet the demands for multicomponent hierarchical functional materials.

Even though NPs and MAMs usually have different dimensions, we can still learn from and even make use of the molecular self-assembly principles to guide the organization of inorganic NPs into ordered structures. Self-assembly of inorganic NPs are valuable to the field of nanoscience, as ensembles of NPs can create spectacular collective properties due to the coupling of plasmons, exactions, or magnetic moments, which are distinct from the properties of individual particles and bulk materials.[22] The collective properties of NP assemblies are influenced by arrangement of NPs, interparticle distances, and overall sizes.[23-25] For example, the plasmon peak of the Au nanorods (AuNRs) will shift as they aggregate. The end to end coupling between AuNRs will induce a red-shift in the longitudinal localized surface plasmon resonance (LSPR), while the side to side coupling will induce a red-shift in transverse mode but a blue-shift in longitudinal mode of LSPR.[23,26] Therefore, it is critical to have delicate control over the assembly structures in order to achieve desired properties. Various strategies have been developed to organize inorganic NPs into ordered structures. They include self-assembly in solution, self-assembly at the interface, or self-assembly on a template.[22] With these strategies, 1D chain structure, 2D film, and 3D structures have been generated (Figure 1.4).[27-33] Both the magnitude and the length scale of these forces can influence the final assembly structures.[34] Despite tremendous progress in NP self-assembly, our ability of assembling NPs is still limited compared to molecular self-assembly. The present dissertation is focusing on developing new strategies for NP assembly and understanding the fundamental principles underlying the self-assembly.

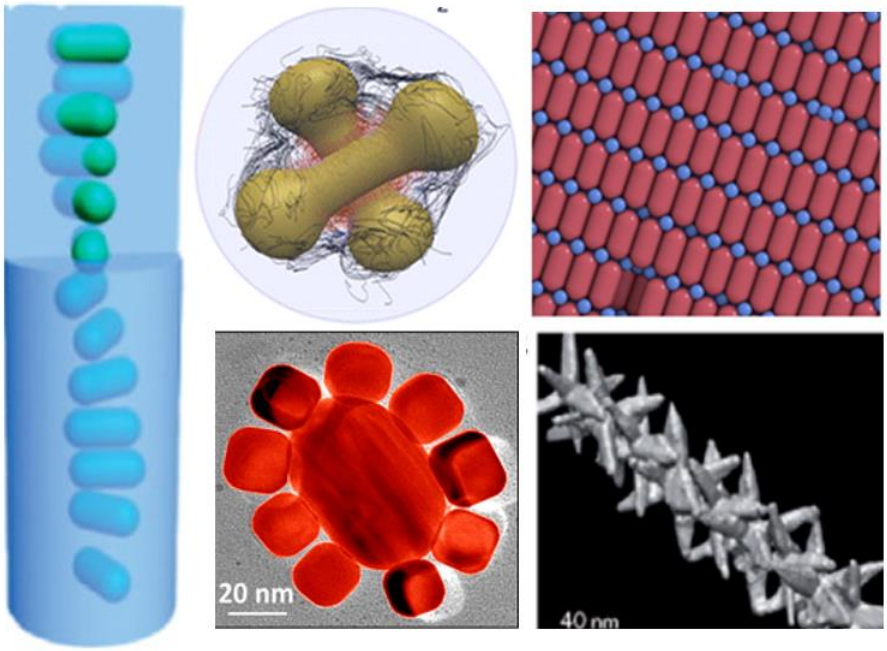

Figure 1.4. Schematic illustration of 1D, 2D, and 3D assembly structures, including clusters, films, and helix chains.[28-31,33] Reproduced with permission from Ref. [28], [29], [30], [31], and [33]. Copyright American Chemical Society.

1.2.1. Biomedical applications of assembled Inorganic nanoparticles

Nanotechnology has great potential to positively impact the evolution of health care related biomedical applications, including imaging, drug delivery, and diagnostics.[24,35,36] The motivation of using inorganic NPs in biomedical applications comes from their intrinsic optical, magnetic, and electronic properties. These properties can be further enhanced by means of assembling inorganic NPs into ordered aggregations. The LSPR coupling is among the most frequently used properties of inorganic NPs for biomedical applications. The sensitivity of LSPR peak to interparticle distance and the strongly enhanced electromagnetic field in the small

gaps between NPs make plasmonic assemblies good candidates for imaging probes, sensors, and therapeutic materials.[37-40]

Plasmonic assemblies can enhance the contrast or the resolution of different types of imaging modalities, including photothermal imaging, surface-enhanced raman scattering (SERs) imaging, photoacoustic imaging (PA), and two-photon luminescence imaging due to the strong LSPR coupling of the assemblies.[41-43] PA imaging is a high spatial resolution biomedical imaging modality that relies on the detection and conversion of ultrasound wave signal generated from tissue upon laser irradiation.[44] Plasmonic assemblies with NIR absorption can enhance the contrast of PA imaging, as the heat generated from assemblies upon absorption of NIR light is transferred to surrounding tissue, leading to stronger thermalelastic expansion of that area. The Nie group reported the self-assembly of AuNPs into vesicular assemblies for the PA imaging of breast cancer in vivo.[45] The strong coupling between AuNPs induced the red-shift of plasmon peaks to NIR range, which facilitated their use as PA imaging materials. As a result, 3.8 times of contrast enhancement in tumor was achieved compared to that without injection of vesicles.

The SERs imaging has also received great attention as a powerful tool to detect molecules, cells and in vivo target.[38,46,47] The Raman signal of molecules close to plasmonic NPs are enhanced because the molecules are subjected to strong electromagnetic field enhancement when the LSPR of NPs are excited by laser light. The LSPR coupling can generate strong electromagnetic field leading to a 10 times enhancement in SERs intensity of molecules between adjacent plasmonic NPs.[48] Still,

the control over the assembly structures is crucial in achieving stronger SERs intensity. For example, it has been reported that SERs intensity of molecules located in the gaps of 1D AuNR chains was not only related to the gap distances, but also to the collinearity and aggregation number of the chain assemblies.[49,50] Duan's group studied the pH-sensitive SERS-active plasmonic vesicles for SERs imaging in SKBR-3 breast cancer cells.[42] The intensity of SERs signal gradually decreased along with the dissociation of vesicles under acidic pH, which was used to monitor the release of payload from vesicles in the target area.

The LSPR coupling can also be used in sensors as a new transduction technique or a way to amplify the signals.[24,51] A color change from red to blue is observed when individual AuNPs aggregated in the solution, due to the stronger LSPR coupling. The Chen group reported an ultrasensitive colorimetric enzyme-linked immunosorbent assay for rapid detection of pathogens, in which the signal transduction and amplification was realized by the aggregation of negative charged AuNPs triggered by the generation of positive thiocholines.[52] The sensitivity of the method is comparable to that of real time polymerase chain reaction, while the operation conditions were simplified. Besides the color change, the strong electromagnetic field within plasmonic assemblies can also improve the detection limit of sensors. For instance, the Au-silver (Au-Ag) core-satellites nanostructures with strong coupling were formed in a Cu^{2+} mediated self-assembly process, leading to 1000 times reduction in the limit of detection (LOD) of analytes.[27]

In addition, the AuNPs assemblies have served as therapeutic materials in cancer

treatment due to their photothermal effect. When AuNPs are irradiated by continuous wave (CW) laser with its wavelength in consistent with the absorption of assemblies, the energy of light will be converted into localized heat, as the result of the nonradioactive decay of free electrons from excited state to ground state.[53] With AuNP assemblies inside tumors, the heat generated from photothermal effect increases the temperature of the surrounding environment of the assemblies to eliminate the tumors. In this process, strong LSPR coupling is needed in the therapy as it increases the photothermal efficiency and induces NIR absorption. The Kim group reported the smart AuNPs with their ligands switching charge from negative to positive in acidic pH condition, leading to aggregation of AuNPs and a shift of the absorption peak from 524 nm to 600 nm.[54] This pH responsiveness enabled the successful photothermal therapy of smart AuNPs in three types of tumor cells, as the strong LSPR coupling due to the spontaneous aggregation of AuNPs increased the efficiency of the therapy. Our group reported the utilization of photosensitizer Ce6 loaded Au vesicles for the cancer treatment both in vivo and in vitro. The absorption peak of the assemblies was tuned to 671 nm, which was the absorption peak of Ce6. With laser irradiation, the photodynamic therapy and photothermal therapy can be simultaneously conducted.[45] The efficiency of the synergistic treatment was higher than that of conducting each separately. To further improve the therapeutic efficiency of plasmonic assemblies, biodegradable assemblies are preferred. The Nie group and Duan group reported the biodegradable AuNPs vesicles as therapeutic materials, independently.[55,56] The vesicles from the Nie group were made from PEG-*b*-poly(ε-caprolactone) (PEG-*b*-PCL)-tethered AuNPs, while the vesicles from the Duan group

were composite of AuNRs tethered with mix PEG and polylactide (PLA). Both vesicles were dissociated into small AuNPs upon NIR irradiation or enzyme degradation, which might facilitate the clearance of NPs from kidney after the treatment.

Iron oxide NPs (MNPs) assemblies have also been widely used in biomedical application such as magnetic resonance imaging (MRI) contrast agents, drug delivery and therapeutic agents.[57-60] The MRI technique uses non-invasive resonant radiofrequency wave as the external energy to generate high spatial resolution images, which overcomes the short tissue penetration problem of lasers.[61] The sensitivity of MRI, which is determined by relaxation rate of surrounding water molecules, can be improved by adjusting the assembly structures of MNPs. For example, it has been reported that the one dimensional MNP assemblies can enhance the saturation magnetization, which improves the sensitivity of MRI.[62-66] The Park group prepared a series of MNP assemblies, such as magneto-polymersomes, magneto-core shell micelles, magnetic micelles and compared their proton transverse relaxation rates (R_2). The magneto-polymersomes showed highest R_2 due to their larger water accessibility than the other two structures.[60] In addition, the Park group has reported that R_2 is also dependent on the size of vesicular assemblies, as it first increases with the sizes and then decreases.[25]

Most of examples discussed above are based on polymer/inorganic NP hybrid assemblies. The combination of polymers and inorganic NPs can improve the performance of materials in biomedical applications. On one hand, compared to

inorganic NPs, organic molecules usually do not possess comparable optical, electronic, and magnetic properties, thus limiting their applications in different areas. The incorporation of inorganic NPs into polymers provide the hybrid materials with new or advanced physical or chemical properties (*e.g.* plasmonic, fluorescence and magnetic properties).[67-71] On the other hand, polymers offers us a tool to precisely control the organization of NP building blocks, leading to desired collective properties for advanced applications. Compared to small molecules like, lipid, the use of polymers in self-assembly can potentially make more complex structures due to the superior chemical and physical stability, mechanical strength, ductility, elasticity, and compositional and structural diversity of polymers. For example, the LSPR of AuNPs can enhance or quench the florescence of quantum dots (QDs) depending on the separation distance between AuNPs and QDs. The smaller separation distance (below 5 nm) induces the quench of the florescence, while larger separation distance (10~20 nm) enhances the fluorescence intensity.[72] The Farinha group reported the self-assembly of well-defined core-satellite structures in which coronas of BCP micelle with a single QD in the core were attached to various number of AuNP.[73] The separation distances between QDs and AuNPs were controlled by the length of PS chain. With a defined separation distance of ~20 nm between AuNPs and QDs, the enhancement in the emission of the CdS QDs increased with the number of AuNPs on the coronas, reaching a maximum of eight times in the enhancement of fluorescence compared to pure QDs. In addition, the presence of BCPs can improve the stability and biocompatibility of the hybrid materials. Some highly monodisperse inorganic NPs like MNPs or QDs are often stabilized by hydrophobic ligands with small

molecular weight. The poor solubility of NPs in aqueous solution or biological fluids limits their applications in biomedicine. Moreover, some ligands such as hexadecyltrimethylammonium bromide (CTAB) on the surface of AuNRs have proven to be biologically toxic. Furthermore, some water soluble inorganic NPs, like QDs, are unstable upon the surface oxidation, generating heavy metal ions toxic to the biological environment.[74] These problems can be solved by encapsulation of inorganic NPs into polymer assemblies. The encapsulation of NPs into polymer materials not only can improve the circulation of NPs in blood vessels and stability of NPs in biological system, but also reduce the toxicity of NP itself and improve the biocompatibility of NPs while not sacrificing their original properties. Therefore, the controllable self-assembly of polymeric/inorganic NP hybrid materials is a promising research direction to reach the goal of biomedical applications.

1.2.2. Self-assembly of polymer/inorganic NP hybrid materials in solutions

The common strategies for the self-assembly of polymer/inorganic NP hybrid materials in solutions can be tentatively classified into two groups based on the number of types of building blocks: i) self-assembly of single type of building blocks into hybrid assemblies, and ii) concurrent self-assembly of multiple types of building blocks into hybrid assemblies.

In the first group, as the hybrid materials are made from a single type of building blocks comprising inorganic NPs grafted with polymers. In the light of the self-assembly ability of MAMs, the building blocks are designed to achieve

amphiphilic feature for triggering the assembly; they are referred to as inorganic NP amphiphiles (NPAMs).[75] The advantages of using NPAMs as assembly building blocks include: i) inorganic NPAMs can exhibit intrinsic optical, electronic, and magnetic properties that are unattainable by their organic counterparts,[39,75,76] and ii) the polymeric ligands with designed chemical compositions maximize our capability of controlling the interactions between NPAMs to assemble into well-defined structures. On one hand, NPAMs can self-assemble as better-studied molecules into defined nanostructures with various morphologies such as chains, micelles, vesicles, and tubules.[39,75-82] On the other hand, the differences between NPAMs and BCP amphiphiles in terms of dimensions, structures, and interactions lead to new assembly mechanism and unforeseeable assembly structures. Compared to BCP amphiphiles, the kinetic factors are more important in the self-assembly of NPAMs as the mobility of NPAMs is much slower than that of their organic counterparts. In addition, the more complex and stronger interactions are involved in the self-assembly of NPAMs due to their larger dimensions, structural complexity, and multiple length scale interactions.[83] These differences offer us the possibility to precisely control the hybrid assemblies with increasing complexity. It is crucial to understand the fundamental principles of the self-assembly of NPAMs, in order to meet our demands for advanced materials.[60]

The NPAMs can be classified into two major categories based on the sources of amphiphilicity. In the category I, the amphiphilicity of NPAMs comes from the combined effect of original ligands and newly introduced polymers on the surfaces of

NPs. The amphiphilicity of category II NPAMs is entirely originated from newly introduced polymers. One typical example of NPAMs in the category I, mentioned above was reported by Nie et al., in which the assembly structures of NPAMs and the resulting collective properties can be tuned by designing NPAMs with defined interactions. In this work, the NPAMs were produced by selectively attaching hydrophobic thiol-terminated polystyrene (PS) molecules onto both ends of hydrophilic CTAB-covered AuNRs, of which the diameter and length are 10 nm and 40 nm, respectively, by taking advantage of the weaker affinity of CTAB towards AuNR (111) end than (100) side.[84-86] The entire hybrid building blocks were analogous to ABA linear triblock copolymers in which a hydrophilic block is linked between two hydrophobic PS blocks. By tuning the polarity of solvents, the aggregation between PS induced the association of NPAMs into a range of nanostructures including rings, nanochains, raft-like disks, and bundles (Figure 1.5). The gap distance between AuNRs in the chain can be finely tuned by changing polymer lengths and water content, which was accompanied with the shift of LSPR peaks.

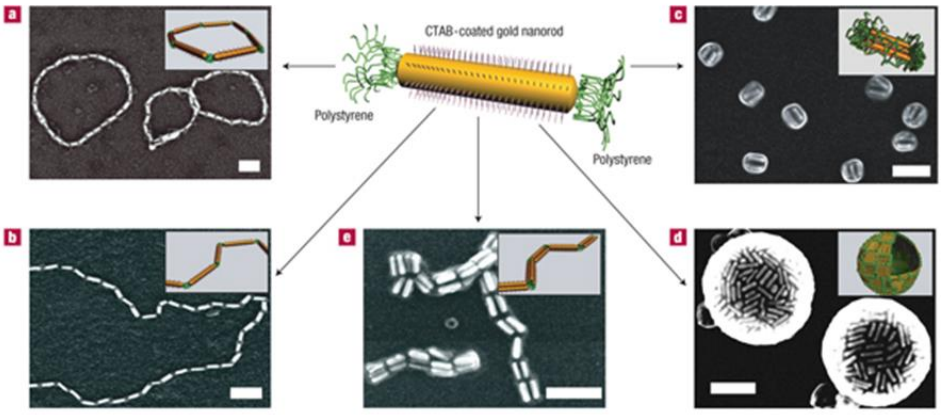

Figure 1.5. Self-assembly of AuNR carrying PS on both ends and CTAB on the side and CTAB on the side. a–e, SEM images of the assembly structures: (a) rings, (b) chains, (c) side-to-side aggregated bundles, (d) nanospheres, and (e) bundled nanorod chains. The scale bars are 100 nm. The insets show corresponding schematic diagrams of the nanorod assemblies.[87] Reprinted by permission from Macmillan Publishers Ltd. [Nature] (Ref. [87]), copyright (2007).

The amphiphilicity of second category of NPAMs originates entirely from polymer ligands. The polymers on the surfaces of NPs can be either a mix of hydrophobic and hydrophilic polymers or amphiphilic BCPs.[39,78,91,92] Even though the polymer ligands are isotopically attached on the surfaces of NPs, the directional interactions can be generated due to the flexibility and compatibility of polymer chains. The Duan group reported the self-assembly of NPAMs with mixed hydrophobic and hydrophilic ligands into vesicles through film rehydration method.[39] The NPAMs were created by attaching PEO to AuNPs and growing poly(methyl methacrylate) PMMA or random copolymer of poly(methyl methacrylate-co-4-

vinylpyridine) (PMMAVP) from the surfaces of AuNPs. The self-assembly of NPAMs was achieved by rehydrating a thin film of NPAMs in water. In this system, two requirements need to be reached to induce the self-assembly. First, the polymer density on the surfaces of NPs need to be high enough (0.4 chain/nm^2) to provide enough free energy that is favorable for the association of NPAMs. Second, external energy is needed to trigger the formation of vesicles. In order to maximize our capability to assemble NPAMs, more thermodynamic controlled systems are preferred. The thermodynamic parameters that control the assembly of NPAMs include the repulsions between the hydrophilic blocks, the favorable or unfavorable interactions between polymer blocks and solvents, and entropy terms related to hydrophobic effect and stretching and compressing of polymer chains. More variety of theoretically predicated assembly structures can be realized by balancing these energy related parameters through different ways such as, changing the structures of NPAMs or preparation method. For example, compared to the film rehydration method, self-assembly of NPAMs by means of gradually changing the polarity of the solvents (*i.e*. solvent exchange method) gives rise to more thermodynamically stable structures.

NPAMs with amphiphilic BCPs on the surfaces have shown outstanding self-assembly abilities through solvent exchange method.[81,93] The Zubarev group designed NPAMs comprising 2 nm AuNPs modified with V-shaped PS-*b*-PEO BCPs containing a carboxylic group at the junction of two blocks.[93] By increasing the water content in the THF solution of NPAMs, the NPAMs associated into cylindrical

wormlike micelles with 18 ± 2 nm in diameter and ~ 100 nm in length and AuNPs located at the interface of hydrophilic PEO shells and hydrophobic PS cores (Figure 1.6). The Liu group developed another interesting strategy to prepare anisotropic NPAMs containing AuNP core with a diameter of 5 nm and tri-BCPs of PEO-*b*-poly(lipoic acid 2-hydroxy-3-(methacryloyloxy)-propyl ester-co-glycidyl methacrylate)-*b*-PS (PEO-*b*-[P(LAMP-co-GMA)]-*b*-PS).[81] The steric effect of polymer chains and small AuNP sizes ensured that only a single chain was attached to each AuNPs through the lipoic acid function groups in the middle block of the tri-BCPs. The resulting NPAMs was asymmetric and amphiphilic. As each hydrophobic AuNP was encapsulated inside a single BCP chain, the self-assembly of NPAMs was similar to that of linear amphiphilic di-BCPs, in which the assembly structures were determined by the packing parameter of the molecules. The packing parameter of NPAMs was controlled by changing the polymer block lengths or sizes of AuNPs, leading to the formation of vesicles, spherical micelles, and cylindrical micelles (Figure 1.6).

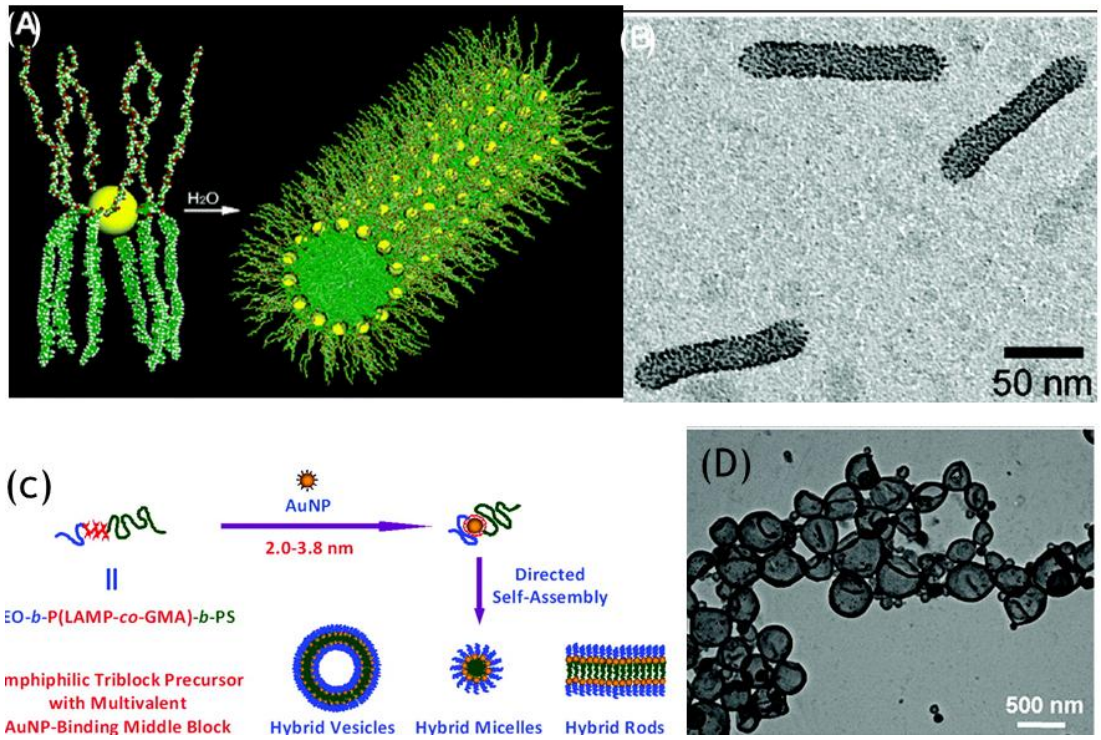

Figure 1.6. Schematic illustration of self-assembly of NPAMs in solution and corresponding TEM. (a) The schematic representation of self-assembly of NPAMs with V-shaped BCP ligands into cylindrical micelles and (b) corresponding TEM image.[93] (c) Schematic illustration of the NPAMs with ultrasmall AuNP core (2.0–3.8 nm) modified with a single tri BCP chain and the hierarchical self-assembly of the resulting NPAMs into various assemblies and (d) corresponding TEM image.[81] A-B reproduced from Ref [93] Copyright © 2006, American Chemical Society. C-D reproduced from Ref [81] Copyright © 2012, American Chemical Society.

Though various hybrid nanostructures have been prepared from the self-assembly of NPAMs, the properties of these materials are limited due to the use of small AuNPs (less than 5 nm). The optical, electronic, and magnetic properties of

inorganic NPs are strongly dependent on their sizes. To achieve desired properties of the assemblies, it is crucial to develop methodology that allows the assembly of NPs with a broad range of dimensions (preferentially larger NPs with a diameter in the range of 10 nm to 100 nm). Our group developed a strategy to prepare NPAMs with core sizes ranging from 5 nm to 70 nm.[76,94] The NPAMs were prepared by attaching thiol terminated amphiphilic BCPs such as PEO-*b*-PS or poly(2(2-methoxyethoxy)ethyl methacrylate)-*b*-PS (PMEO$_2$MA-*b*-PS), directly onto the surfaces of AuNPs. As water was added into the THF solution of NPAMs, various nanostructures of NPAMs, including unimolecular micelles, clusters, and vesicular structures to minimize unfavorable interfacial energy were obtained (Figure 1.7). Simulation results indicated that deformability of NPAMs (including both AuNP cores and BCP ligands) determined the assembly morphologies. The deformability can be characterized by the ratio of the root mean square end-to-end distance of BCP chains (R_0) to the diameter of AuNPs (d_{Au}). $R_0/d_{Au} \sim 0.4$ is the boundary between clusters and vesicles. We proposed that the relative short BCP chains compared to AuNP cores limited the redistribution of polymer ligands on NPAMs, leading to the formation of clusters or unimolecular micelles. NPAMs with relative long BCP chains assembled into vesicles due to the directional hydrophobic interactions generated after the redistribution of PEO beads on the NP surface.

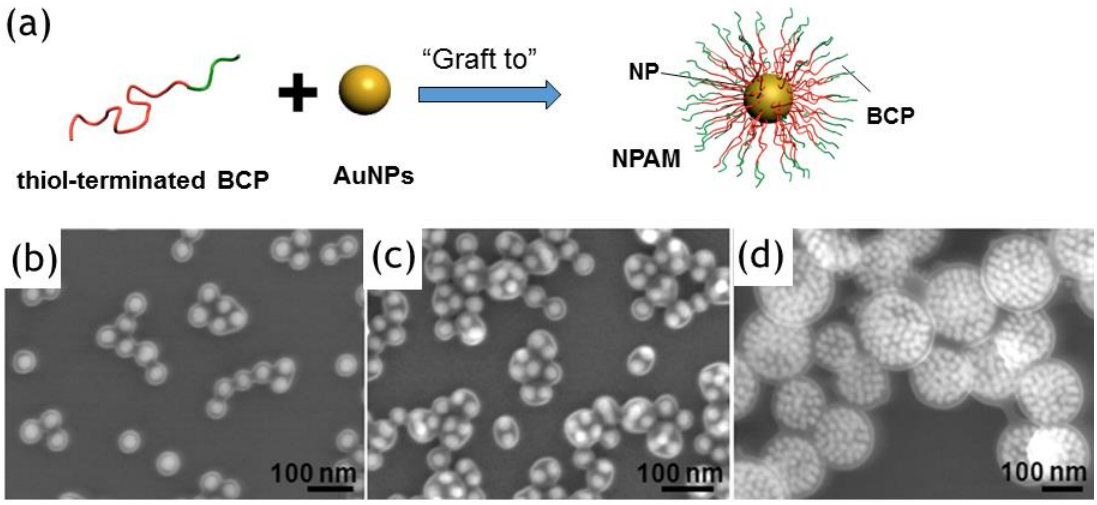

Figure 1.7. Self-assembly of NPAMs with amphiphilic linear BCP ligands (a) The schematic representation of preparation of NPAMs by attaching thiol terminated BCPs onto the surfaces of AuNPs. (b-d) Self-assembly of resulting NPAMs into (b) unimolecular micelles, (b) clusters, and (c) vesicles.[76] Reproduced from Ref. [76] Copyright © 2013, American Chemical Society.

The grafting of pre-synthesized linear amphiphilic BCP ligands to the surfaces of NPs is a general and easier method to prepare NPAMs in comparison to methods of growing polymers from surfaces of NPs or using V-shaped polymer as ligands, which needs complex synthetic procedures. The various assembly structures made from NPAMs suggest that *NPAMs are promising self-assembly building blocks for making hybrid materials. How to further improve properties of NPAMs assemblies remain as challenge.*

1.2.3. Concurrent self-assembly of multiple types of building blocks into hybrid assemblies.

The concurrent self-assembly of multiple types of building blocks into a single nanostructure, as it was previously mentioned in 1.2.2 (group ii), is a promising strategy in making hybrid materials with improved physical and chemical properties. Although the assembly of single type of building blocks has led to a rich variety of nanostructures, it is unlikely to meet all the demand for new functional materials in various fields. As we are interested in polymeric/inorganic hybrid materials, the concurrent assembly of inorganic NPs and BCPs allows us to use relative easily obtained building blocks to make complex structures.[95-100] In general, the concurrent self-assembly can be understood in terms of the minimization of free energy which comprises enthalpy terms and entropy terms. The concurrent self-assembly of multiple types of building blocks often involves (i) the competitive interactions such as molecular immiscibility that often results in phase separation of the amphiphiles, (ii) the cooperative interactions such as geometric packing, hydrogen bonding and electrostatic interactions that often lead to the formation of combined building blocks to participate in the assembly process, and (iii) stronger role of entropy in the structural formation, due to the entropy loss during the stretching and compressing of MAMs. In the concurrent self-assembly of BCPs, it is crucial to fine tune the delicate balance of interactions involved in the assembly to achieve desired complexity of nanostructures; otherwise, macrophase separation may take place, resulting in the formation of completely segregated phase domains. Furthermore, to achieve

functional nanostructures with desired properties, it is crucial to address critical questions regarding the concurrent assembly of NPs and polymers. For example, how NPs and polymers interact with each other to give rise to specific structures? How to control the spatial location of inorganic NPs within assemblies, as the collective properties of NP ensembles are strongly dependent on interparticle spacing and relative position?

The concurrent self-assembly of hydrophobic inorganic NPs and BCPs into hybrid micelles can transfer hydrophobic NPs into aqueous solutions.[100-106] Even though hybrid micelles are formed due to hydrophobic interactions, the assembly processes are not trivial. The micelle structures, including the assembly sizes, morphologies, and average NP encapsulation number, are influenced by the ligands on the NPs, NP sizes, and BCP lengths. Highly uniform inorganic NPs (*e.g*, MNPs or QDs) with great therapeutic potential, synthesized by thermal decomposition method,[107,108] are usually covered by hydrophobic ligands. Therefore, the surface of these NPs must be modified to be dispersed into water before they can be use in biomedical applications. With the addition of polar solvent, like water, into a mix solution of hydrophobic NPs and BCPs, the hydrophobic NP will be encapsulated in the hydrophobic polymer domain to minimize the interfacial energy between polar solvent and hydrophobic surfaces of NPs. For instance, the Taton group reported the preparation of Au@polymer core shell NPs,[109,110] by adding water into a solution of 1-dodecanethiol, AuNPs, and BCPs in THF. In this work, 1-dodecanethiol, a hydrophobic ligands were attached to the surfaces of AuNPs before the AuNPs were

encapsulated by BCPs micelles (Figure 1.8). The number of AuNPs encapsulated in individual micelles can be controlled by varying the size of AuNPs and the relative length of BCPs.

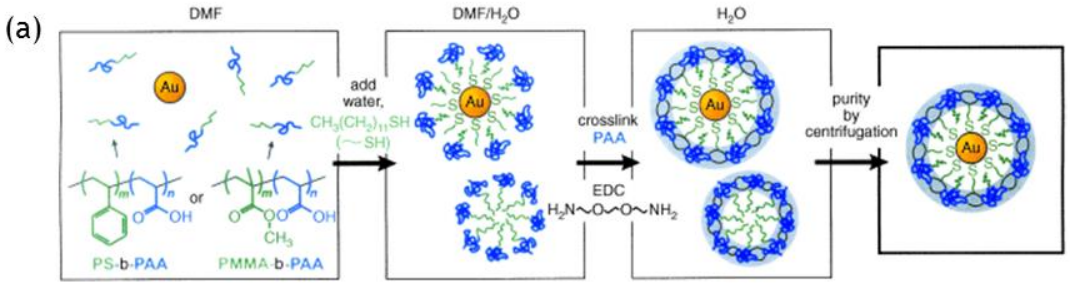

Figure 1.8. The schematic illustration of preparation of Au@polymer core shell NPs through self-assembly.[109] Reproduced from Ref. [109]. Copyrights 2005 Wiley

The addition of NPs or the loading content of NPs can induce the morphological transition of BCP assemblies. The NPs inserted into polymeric assemblies can affect the previously mentioned free energy related parameters and the packing parameter of BCP amphiphiles. The Park group systematically studied the effect of the content of hydrophobic magnetic NPs on the self-assembly behaviors of micelle forming PS-*b*-PAA (Figure 1.9 a).[60] When the weight percent of NPs increased from 0% to 10%, and finally to 35.8%, the morphology of assemblies transited from polymeric micelles (Figure 1.9 b), to mixture of magnetic micelles and magneto-polymersomes (Figure 1.9 c and d), and eventually to pure magneto-polymersomes (Figure 1.9 e). This morphology transition was explained by the increase in the hydrophobic volume upon the addition of hydrophobic NPs, which

increased the packing parameter of the polymer building blocks (Figure 1.9 h).

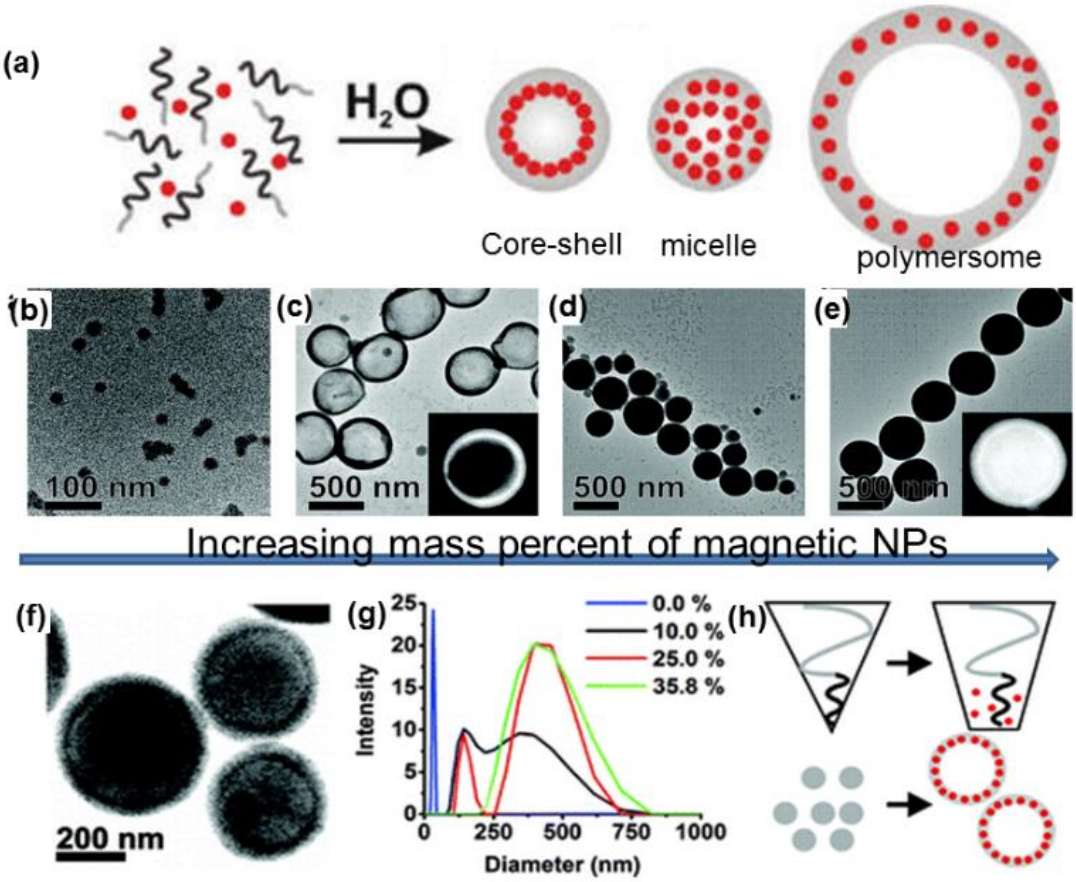

Figure 1.9. (a) Schematic illustration of concurrent self-assembly of NPs and BCPs into magneto-core shell assemblies, magneto-micelles, and magneto-polymersomes. (b-e) TEM image of the (b) polymer micelles, (c,d) mixture of magneto-micelles and magneto-polymersomes, and (e) pure magneto-polymersomes. From (b-d) the mass percent of the magnetic NPs are 0%, 10%, 20%, and 35%, respectively. (f) A bright field STEM image of maneto-polymersomes. (g) DLS data of the four different samples. (h) Schematic illustration of the morphology transition caused by the addition of magnetic NPs.[60] Reproduced from Ref. [60] copyright © 2011, American

Chemical Society.

In another example, the Zhu and Nie groups demonstrated that the loading content of NPs can influence the assembly morphology in concurrent self-assembly of PS-modified AuNPs and supramolecules of PS-*b*-P4VP (pentadecylphenol (PDP)) (Figure 1.10 a).[111] The morphologies of hybrid assemblies transitioned from spherical micelles to cylindrical micelles, and to nanosheet with the increasing the mass ratio of AuNPs to polymers. The structural transitions are explained by the change in the relative volume between PS and P4VP (PDP) in micelles upon the addition of AuNPs. The same group further assembled Au nanorods (AuNRs) modified with a mixture of PS with different lengths into the cylindrical micelles core of PS-b-P4VP (PDP) using the same approach.[31] With the increase in the content of AuNRs, the hybrid assemblies underwent morphological transitions from cylindrical hybrid micelles with nanorods aligned along the long axis of the micelles, to cylindrical hybrid micelles with nanorods perpendicular to the long axis of the micelles, and eventually to hybrid micelles with helical arrangements of nanorods that are perpendicular to the long axis of the micelles (Figure 1.10 b).

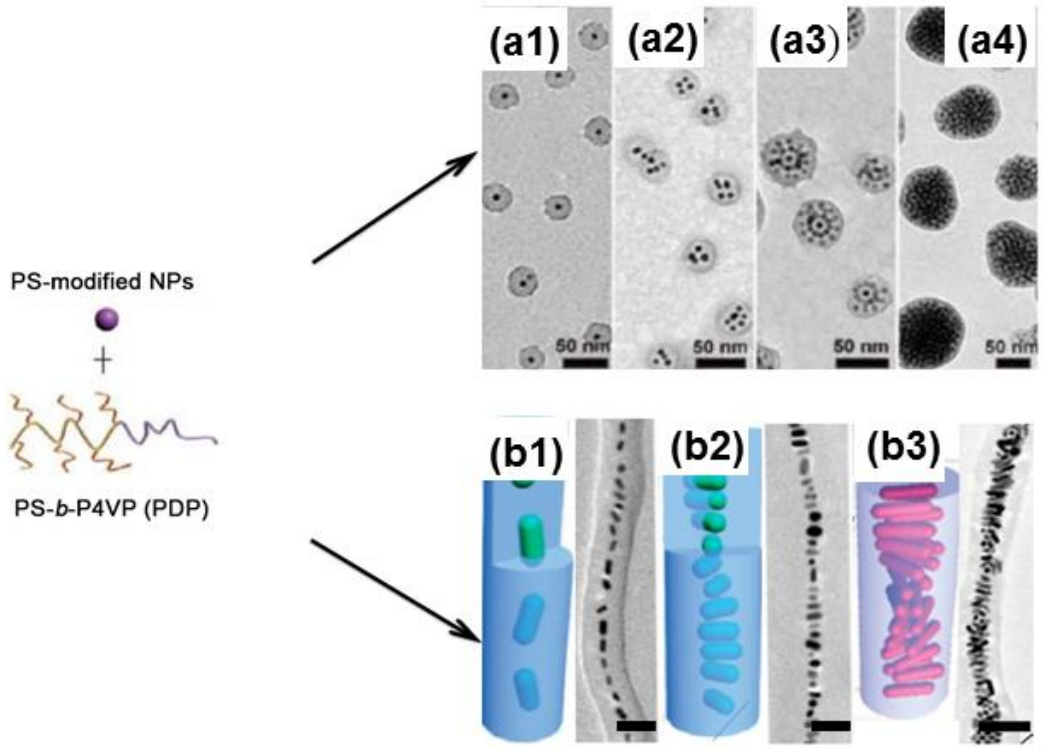

Figure 1.10 . Schematic illustration of concurrent self-assembly between PS-modified NPs and PS-b-P4VP (PDP). (a) Hybrid clusters with increasing AuNPs contents through increasing the content of AuNPs or adjusting the content of PDP (the size of AuNPs is 7.5 nm);[111] (b) Hierarchical AuNRs arrangements with end-to-end/side-by-side orientation encapsulated in discrete cylindrical domain.[31] Scale bars: 50 nm in (a1), (a2), and (a3) and 100 nm in (b1), (b2), and (b3). Reproduced from Ref. [31] and [111] Copyright © 2013, American Chemical Society

The spatial distribution or orientation of NPs within polymer micelles can be also controlled by various means.[112] The Chen group pioneered the strategy of concurrent self-assembly of free BCPs of PS-*b*-PAA and AuNPs modified by mixed

hydrophilic and hydrophobic small ligands to generate hybrid micelles with eccentrically encapsulated NPs. By adjusting the ratio of two small molecular ligands, the location of AuNPs can be shifted from the center of the polymer micelles to the edge of the polymer micelles. The eccentric hybrid micelles can form dimmers via salt induced aggregation (Figure 1.11 a and b).[113] In a following study by the Chen group, the AuNPs (AuNRs)/PS-b-PAA hybrid micelles were placed in an acidic DMF/H_2O mixture. The structural transformation of the polymer micelles from spheres to cylinders in such mixed solvents forced the embedded AuNPs to form cylindrical chains. The morphology transition is a result of the interplay of the degree of stretching of PS in the core, the repulsion force between PAA corona, as well as polymer solvent interfacial tension.[114] The Chen group further demonstrated that the concurrent self-assembly of the AuNPs(AuNRs)/PS-PAA hybrid particle and PS-b-PAA spheres through a similar method, mentioned above, led to cylindrical micellar structures containing both AuNPs blocks and empty polymer domains.[96] Furthermore, the orientation of NPs can be also tuned by controlling the interactions between NPs and polymers. For example, the Liz-Marzan group produced hybrid PS-b-PAA assemblies loaded with cross-like orientation of gold nanodumbells (AuNB) in hydrophobic cores using a combination of space confinement and steric hindrance.[29] Compared to AuNRs, AuNBs' ends are both bigger, resembling dumbbell structure. By adding water into a solution of AuNBs with end functionalized by PS in DMF/THF mixture (THF:DMF=1:3 v/v), the AuNBs formed side-to-side arrangement. With the addition of PS-b-PAA and increase in the water content followed by thermal treatment, the side-by-side arrangement of AuNBs gradually

changed into cross-like orientation (Figure 1.11 c and d). In an additional study from Chen group, spherical polymer micelles of PS-b-PAA were used to induce the coiling of ultrathin Au nanowires (AuNWs) embedded in the hydrophobic core.[115] The AuNWs were encapsulated inside the hydrophobic domains of polymer micelles through the hydrophobic interaction. To minimize the interfacial energy between PS and solvent, the spherical micelles formed, which generated a compression force to induce the coiling of embedded AuNWs. Interestingly, because of the relative low attractive interaction between the AuNWs, the loops of AuNWs could spring back into straight wires by swelling or removing the polymer shells.

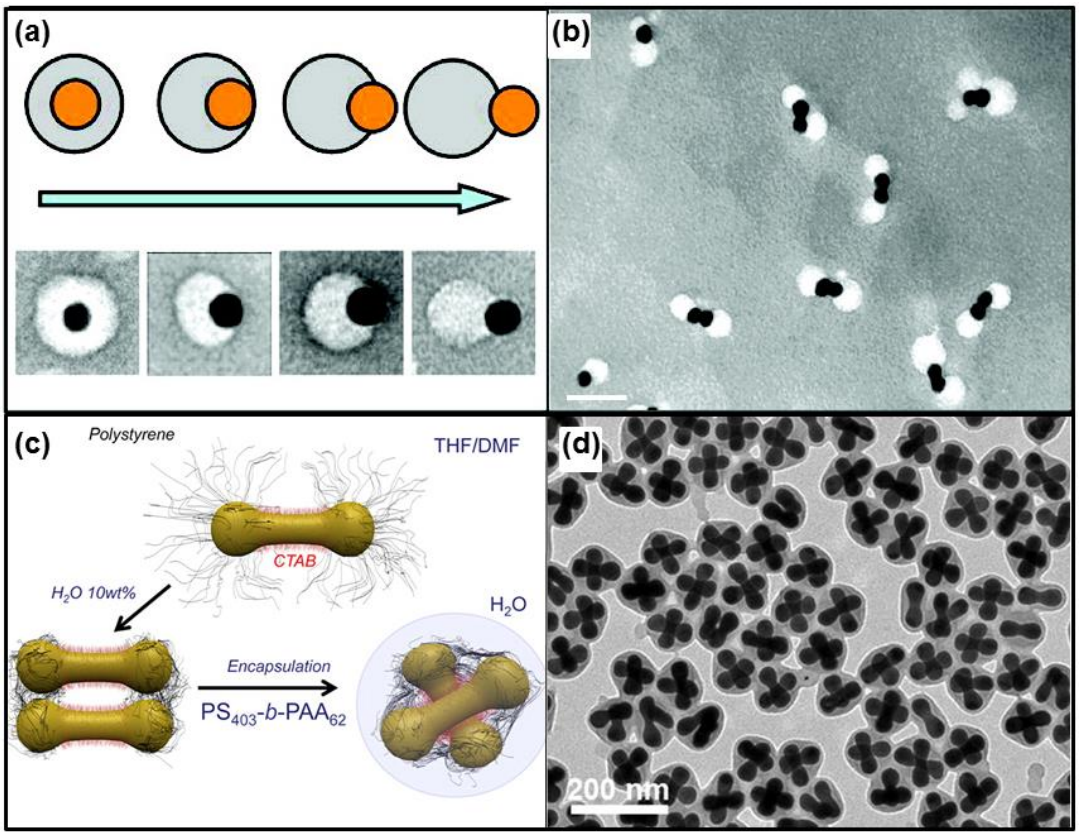

Figure 1.11. To control the spatial distribution and orientation of NPs through

concurrently self-assembly (a) Schematic illustration and corresponding TEM images of concentric and eccentric hybrid micelles. (b) The eccentric hybrid micelles were able to form dimmers via salt induced aggregation. Scale bar: (b) 50 nm.[113] (c) Schematic illustration and (d) corresponding TEM images of the cross-like orientation of AuNB within polymer micelles.[29] (a and b) Reproduced from Ref. [113] Copyright © 2008, American Chemical Society. (c and d) Reproduced from Ref. [29] Copyright © 2012, American Chemical Society.

The concurrent assembly of NP and MAMs is an efficient way to fabricate hybrid materials. Previous examples have already shown that concurrent assembly of two types of BCPs amphiphiles or two types of amphiphiles with different dimensions (lipids and BCPs) greatly enlarge the library of assembly structures.[95-100] As I mentioned in the section 1.22, NPAMs with amphiphilic linear BCPs on the surfaces have emerged as promising hybrid building blocks due their controllable self-assembly behaviors. *As NPAMs can self-assembly as MAMs do*, t*he concurrent self-assembly of MAMs and NPAMs are expected to form complex assemblies*. *However, to understand the concurrent self-assembly mechanism and to increase our control over the assembly morphologies need more systemic study.*

1.3. Scope of the dissertation

As discussed in the previous sections, the formation of ordered assembly structure is the prerequisite for achieving desired properties for various applications. I have chosen NPAMs as the starting building blocks for i) *intrinsic physical properties*

needed in biomedical applications and ii) *capacity to mimic molecular self-assembly and potentially improve control over the assembly structures.* The objective of this dissertation is to study the *self-assembly of NPAMs by themselves and the concurrent self-assembly of NPAMs with MAMs and NPs, and to improve the performance of the materials in various biomedical applications*. Compared to MAM self-assembly, the self-assembly of NPAMs is more challenging due to the more complex interactions involved in the system. However, we can also make use of these complex interactions to prepare multicomponent assembly structures with unique properties.

Chapter 2 describes the step-wise hierarchical self-assembly NPAMs into chain vesicles to enhance the plasmon coupling between NPs. The stronger coupling in the chain vesicles led to the NIR absorption and a higher photoacoustic efficiency than non-chain. Chapter 3 is concerned with the concurrent self-assembly of BCPs and NPAMs. This strategy increased our controllability over the vesicles shapes and NPs distributions. Chapter 4 describes a method to prepare MNPs/AuNPs hybrid vesicles. The hydrophobic MNPs played an important role in determining the assembly morphologies. The hybrid multicomponent vesicles are promising multimodal imaging and drug delivery materials. Chapter 5 presents a Janus nanomotor system based on the phase separation between NPAMs and free BCPs, which contain both Au NPs and Pt NPs. The autonomous propulsion of Janus vesicles was realized with the presence of chemical fuel H_2O_2 and controlled release of payloads triggered by NIR laser irradiation was demonstrated. A summary of the works done in this dissertation and recommendations for the future work are presented in Chapter 6.

Chapter 2: Hierarchical self-assembly of vesicles of nanoparticle chains for enhanced photoacoustic imaging

Overview. We reported the self-assembly of hybrid vesicles containing chains of AuNPs in the hydrophobic membrane. The chain vesicle formation can be controlled by tuning the polymer ligand density on the surface of AuNPs. The strong coupling of AuNPs in the chain vesicles leads to the red-shift of LSPR to the NIR range. We demonstrated strong coupling of chain vesicles enhanced the photoacoustic (PA) efficiency.

A manuscript based on this chapter is in preparation and to be submitted to *Angew. Chem. Int. Ed.*

2.1 Introduction

Controlled self-assembly of inorganic NPs into larger or ordered structures is crucial to their applications ranging from nanomedicine[116,42] to optoelectronics,[117] and to energy production and storage.[118] The organization of inorganic NPs gives rise to new collective properties that are distinct from their individual or bulk counterparts due to the coupling between inorganic NPs.[22,76,87] These properties are generally dependent on the size and shape of NPs and the spatial arrangement of NPs within ensembles. For instance, one dimensional (1D) organization of AuNPs leads to the splitting of plasmonic band into two distinct peaks corresponding to the transverse and longitudinal modes. In contrast, isotropic aggregates of AuNPs show a large

broad absorption depending on the interparticle distance.[119,120]

Inorganic nanoparticles have been extensively explored for cancer imaging and therapy, due to their unique size and intrinsic optical and magnetic properties. Among them, AuNP-based platform uniquely combines multimodal and combination therapy in one system to achieve effective theranostics. Particularly, the assembly of AuNPs into defined nanostructures (e.g., clusters, chains, vesicles) can further improve the performance of NPs.[63,121,122] 1D chains of AuNPs showed several orders of magnitude enhancement in the electromagnetic field, which lead to stronger signal in SERS or biosensors.[62,123] However, 1D chains lack the ability to encapsulate therapeutic agents. In contrast, vesicular assemblies of AuNPs not only can serve as contrast agent for bioimaging, but also allow the efficient loading of both hydrophobic and hydrophilic drugs.[42,43,76,99,] In this case, the interparticle spacing of the plasmonic vesicles has to be carefully tuned to achieve absorption in the NIR range. The red-shift of the plasmon peak arising from plasmonic coupling is proportional to $exp^{-(d/D)}$, where d and D are interparticle distance and NP diameter, respectively.[76] When the size of NPs is small, it becomes challenging to tune the absorption of 3D vesicular assemblies of AuNPs to the NIR range.

This chapter describes the step-wise hierarchical self-assembly of BCP tethered AuNPs (NPAMs) into hollow vesicles composed of a single layer of NP chains in the membrane. The assembly involves two critical steps: the organization of individual NPAMs into chains and further assembly of the chains into NP chain vesicles (Figure 2.1). The formation of NP chain vesicles rather than vesicles with uniform

distribution of NPs in the membrane (referred to as non-chain vesicles) is achieved by tuning the grafting density (δ) of BCPs on the surfaces of AuNPs. The small interparticle distance between NPs along the chains in the membrane leads to tunable LSPR absorption in the NIR window, thus facilitating the application of the chain vesicles in biomedical applications. We demonstrated that chain vesicles showed eight fold enhancement in the photoacoustic signal when they are used as contrast agent for *in vivo* imaging, compared with non-chain vesicles.

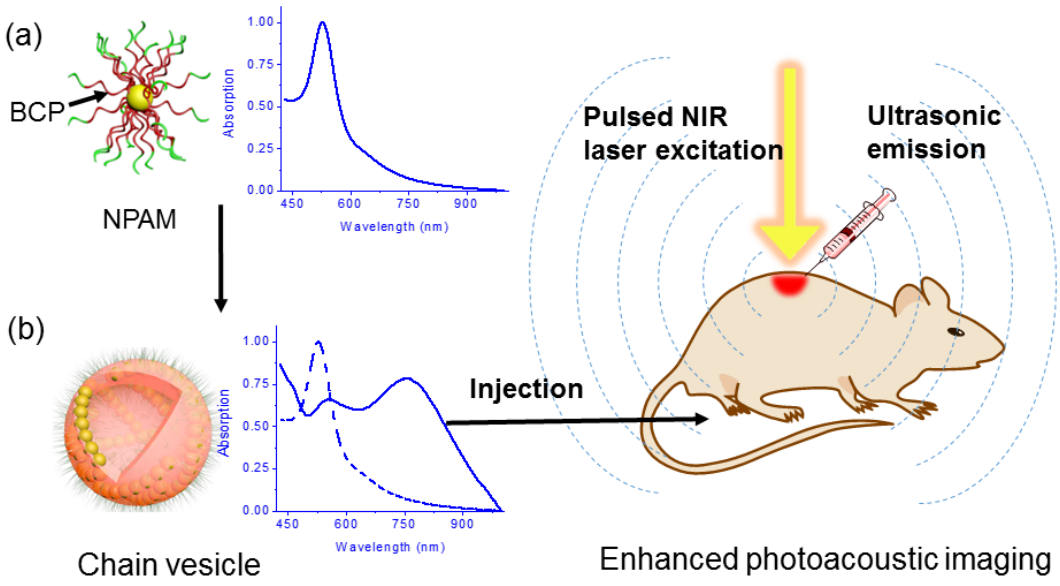

Figure 2.1. Schematics illustrating the self-assembly of BCP-AuNPs into chain vesicles for photoacoustic imaging.

2.2 Experiments

2.2.1 Materials

Styrene, azobis(isobutyronitrile) (AIBN), 4-cyano-4-(phenylcarbonothioylthio) pentanoic acid (CPPA), THF, DMF, sodium borohydride (NaBH4, ≥99%), gold(III) chloride trihydrate ($HAuCl_4$, ≥99.9% trace metals basis), sodium citrate tribasic dihydrate (≥99%), CTAB, Sodium oleate (NaOL), and silver nitrate ($AgNO_3$) were purchased from Sigma-Aldrich. Styrene was distilled under vacuum prior to use and stored in a freezer at -20 ^{o}C. AIBN was recrystallized from ethanol. Deionized water (Millipore Milli-Q grade) with resistivity of 18.0 MΩ was used in all the experiments.

2.2.2 Synthesis of thiol-terminated BCPs.

Thiol-terminated BCPs of HS-PS-*b*-PEO were synthesized using reversible addition-fragmentation chain transfer (RAFT) polymerization reported previously.[78] Chain transfer agent (PEO-CTA) was synthesized by attaching 4-cyano-4-(phenylcarbonothioylthiol) pentanoic acid to the PEO with molar mass of 2 kg/mol by esterification. RAFT polymerization was performed to grow PS block of BCPs from the PEO-CTA to make CTA-PS-*b*-PEO. Basically, styrene, PEO-CTA, and AIBN were dissolved in dioxane with a molar ratio of 500:1:0.2. The solution was purged with argon for 30 min before the reaction was put into an 80 ^{0}C oil bath. The reaction

was thermalstatted bath for 36 h before the reaction was quenched by cooling the reaction in liquid nitrogen. The product was precipitated in hexane and dissolved in THF to remove unreacted monomers and impurities. This purification step was thrice repeated. Molecular weights characterized by gel permeation chromatography (GPC) and ^{1}H NMR are 24.0 kg/mol and 33.6 kg/mol, respectively. The PDI of the BCP is 1.20. The CTA-PS-*b*-PEO was mixed with n-butylamine for 4 hours to convert CPPA into thiol groups. Excess n-butylamine was removed by sequential purification.

2.2.3 Synthesis of 3.5 nm seeds of AuNPs and CTAB covered AuNPs

The AuNPs stabilized by CTAB were prepared by a seed-mediated growth method as reported with minor modification.[124] Seeds of 3.5 nm AuNPs were synthesized as follows. A 4.9 mg mass of $HAuCl_4$ and 3.7 mg mass of sodium citrate were firstly dissolved in 50 mL of aqueous solution. A 1.5 mL volume of ice-cold, freshly prepared 0.1 M $NaBH_4$ solution was injected into the solution under strong stirring. The mixed solution turned brown immediately and the solution was further stirred for 3-4 hr.

CTAB-AuNPs of 13 nm were synthesized using the seed-mediated growth method.[18] The growth solution was prepared by adding 44.3 mg mass of $HAuCl_4$ and 1.5 g mass of CTAB in 450 mL of water, followed by the addition of 2.5 mL of 0.1 M ascorbic acid. Under vigorous stirring, a 15 mL of gold seed solution (seeds of 3.5 nm AuNPs) was quickly poured into the growth solution. The reaction mixture was stirred for 30 min at room temperature and then held at 29 ^{0}C for overnight.

CTAB-AuNPs of 20 nm diameter were synthesized following the above procedure with adjustment of the ratio between seeds and growth solution.

2.2.4 Preparation of NPAM

NPAMs were created by attaching BCP onto surfaces of AuNPs using an interfacial ligand-exchange method. Typically, predetermined mass of BCPs were first dissolved in 10 mL of chloroform, depending on the targeted grafting density of polymers on NPAMs. This solution was then added into an aqueous solution of 13 nm AuNPs, followed by sonication for 2 h to emulsify at room temperature. The resulting emulsion was kept undisturbed overnight. Spontaneous phase separation was observed with two layers, including the colorless aqueous phase (top layer), and chloroform phase containing AuNPs. The organic phase was then collected and dried under vacuum. The NPAMs were dispersed in THF and further purified by centrifugation in THF/hexane (1:2, vol. %) for six cycles. The final NPAMs were dissolved in THF with a concentration of 0.5 mg/mL. The relation between δ and BCP amount is summarized in Figure 2.2

2.2.5 Polymer grafting density calculation

The mass of AuNPs and BCPs was measured by TGA. The number of AuNPs in the sample can be calculated by the following equation

$$N_{(AuNPs)} = \frac{mass\ of\ AuNPs}{D_{(Au)} * V_{(AuNP)}} \qquad \text{(Eq. 2.1)}$$

where $D_{(Au)}$ is the density of gold and $V_{(AuNP)}$ is the volume of a single AuNP.

The number of polymer chains on the surfaces of AuNPs can be calculated by the following equation

$$N_{(BCPs)} = \frac{Mass\ of\ BCPs}{Mw\ of\ BCPs} * N_A \quad \text{(Eq. 2.2)}$$

where NA is the Avogadro's number.

The polymer grafting density can be caclualated from the following equation

$$\delta = \frac{N_{(BCPs)}}{N_{(AuNPs)} * A_{(AuNP)}} \quad \text{(Eq. 2.3)}$$

where $A_{(AuNP)}$ represents the surface area of a single AuNP.

Sample number	Mass of BCPs	Mass of AuNPs	Chains per AuNP	Grafting density
1	0.018 mg	0.517 mg	16	0.03 chain/nm^2
2	0.070 mg	0.970 mg	27	0.05 chain/nm^2
3	0.048 mg	0.456 mg	42	0.08 chain/nm^2

Table 2.1 the mass of BCPs and AuNPs measured from TGA and corresponding polymer grafting density calculated from above equations.

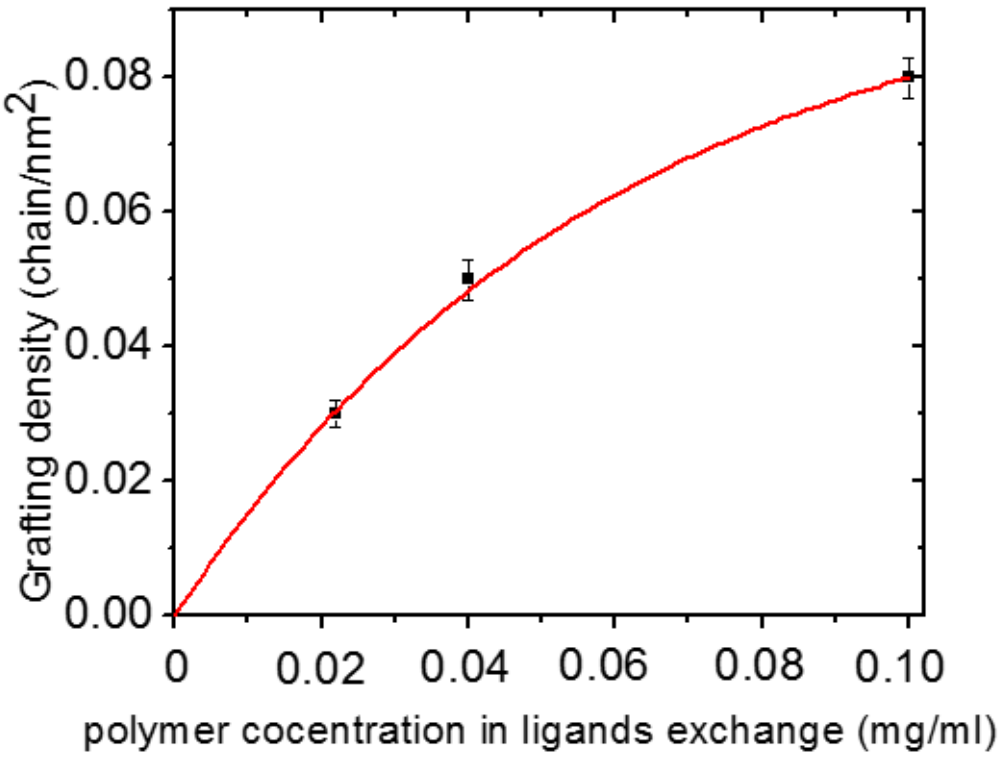

Figure 2.2. The relationship between the polymer ligands δ on the surfaces of AuNPs and amount of BCPs used in the ligands exchange. The δ of polymer ligands characterized by TGA. The BCP-AuNPs were prepared by modifying 1 mg of AuNPs with 0.1 mg, 0.4 mg, and 1 mg BCPs, respectively.

2.2.6 Self-assembly of NPAMs.

The self-assembly of NPAMs was triggered by dialyzing (dialysis bags with the Mw cutoff of 3000–5000 g/mol) the THF solution of NPAMs against water. The THF solution of NPAMs (~0.5 mg/mL) was dialyzed under gentle stirring for 24 h. The slow solvent exchange to the selective solvent (water) triggered the self-organization of NPAMs into various assemblies.

2.2.7 The investigation of self-assembly mechanism and kinetics

A 2 mL THF solution of NPAMs (0.5 mg/mL) was held in a glass container with stirring. A 20 μL of water was injected into the solution while stirring and the solution was allowed to stir for 3 min. This step was repeated until certain water content was reached. Solution samples with different water contents were taken for TEM or SEM characterizations and UV-VIS measurement.

2.2.8 Sample preparation for thermal gravimetric analysis (TGA)

Hexane was added into a THF solution of NPAMs to make a THF/hexane mixture with a volume ratio of 1:2. The solution was subjected to centrifugation until sediments of NPAMs were formed and the supernatant was clear. The sediments were dried in vacuum oven for 48 hours to remove the solvent residues before TGA measurement.[125-127]

2.2.9 Characterizations

The morphologies of assemblies were imaged using a Hitachi SU-70 Schottky field-emission gun (FEG) Scanning Electron Microscope (SEM) and a JEOL FEG Transmission Electron Microscope (TEM). SEM samples were prepared by casting a 5-10 μL of sample solution on silicon wafers and were dried at room temperature.[128] TEM samples were prepared by casting on 300 mesh copper grids covered with carbon film and were dried at room temperature. The plasmon coupling of AuNPs was monitored by PERKIN LAMBDA 35 UV–VIS spectrometer.

2.3 Results and discussion

2.3.1 Preparation of NPAMs and characterizations of hybrid vesicles

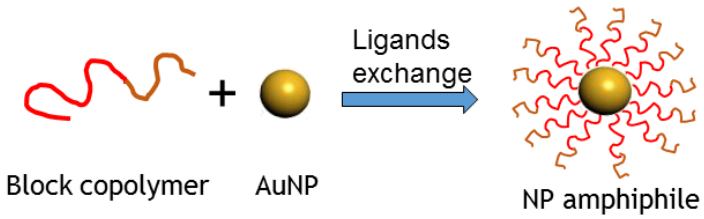

Figure 2.3. Schematic illustration of the synthesis of NPAMs by ligands exchange method.

CTAB-covered 13 ± 1.0 nm AuNPs were modified with thiol terminated polystyrene-*b*-polyethylene oxide (PS-*b*-PEO) through interfacial ligands exchange method we recently developed (Figure 2.3).[76] For the preparation of NPAMs, BCPs and AuNPs with different sizes were dissolved in water and $CHCl_3$, respectively. When the emulsions of the two immiscible solvents were formed under shaking, the AuNPs moved to the interface between water and oil, and were modified by the polymers through covalent interactions between thiol and Au. After the emulsions were broken, the resulting NPAMs were transferred into the oil phase. The free BCPs that were not attached on to the surface of AuNPs can be removed by multiple cycles of centrifugation. This method can be applied to AuNPs with different sizes easily without the need of concentrating the AuNPs. We adjusted the polymer grafting

density on the surfaces of AuNPs from 0.03 chain/nm^2 to 0.08 chain/nm^2 and higher by controlling the ratio between BCPs and AuNPs. The number of chains per AuNP corresponding to the polymer density of 0.03 chain/nm^2, 0.05 chain/nm^2, and 0.08 chain/nm^2 are 16, 27, and 42, respectively.

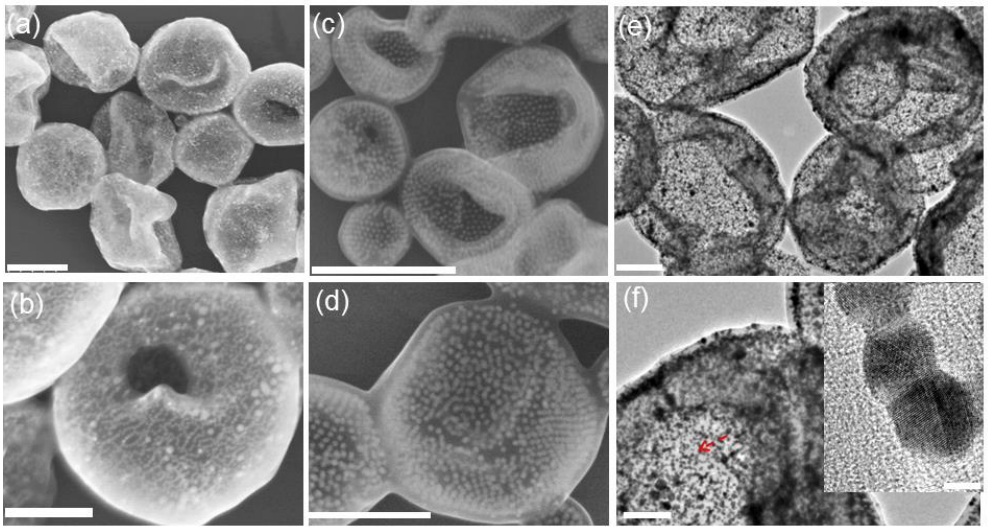

Figure 2.4. Representative SEM and TEM images of chain vesicles and non-chain vesicles. SEM images of (a,b) chain-vesicles and (c,d) non-chain vesicles made from BCP-AuNPs (13). The wrinkles in SEM images confirm the hollow nature of vesicles. Representative TEM images of (e,f) chain vesicles and (inset of f) fused chain structures within the vesicles. Scale bars: 500 nm in (a) and (c), 250 nm in (b) and (d), 200 nm in (e), 100 nm in (f), and 5 nm in inset of (f).

The PS-*b*-PEO with a PS block of 31.6 K and a PEO block of 2 K was used throughout the work.[78] The δ was controlled in the range of 0.03 chain/nm^2 to 0.08 chain/nm^2 by varying the ratio of BCPs to AuNPs during surface modification and being characterized by TGA (Figure 2.2 and Table 2.1). The NPAMs were denoted as

BCP-AuNPs (D), where D is the average diameter of AuNPs. The BCP-AuNPs were dispersed in THF for further self-assembly. The assembly of BCP-AuNPs was triggered by dialyzing a solution of building blocks in THF against deionized water, which is a selective solvent for the BCPs on the surface of NPs. The addition of water increases the unfavorable interfacial energy between water and hydrophobic PS, causing the collapse of hydrophobic polymer chains or association of BCP-AuNPs. The BCP-AuNPs with smaller Au cores or longer PS chains preferred to form vesicles instead of clusters or unimolecular micelles because of the larger deformability of NPAMs (including both AuNPs and BCP ligands). We presume that PEO chains reorganize to the surfaces of NPs during the association of BCP-AuNPs, leading to the formation of vesicles.[76]

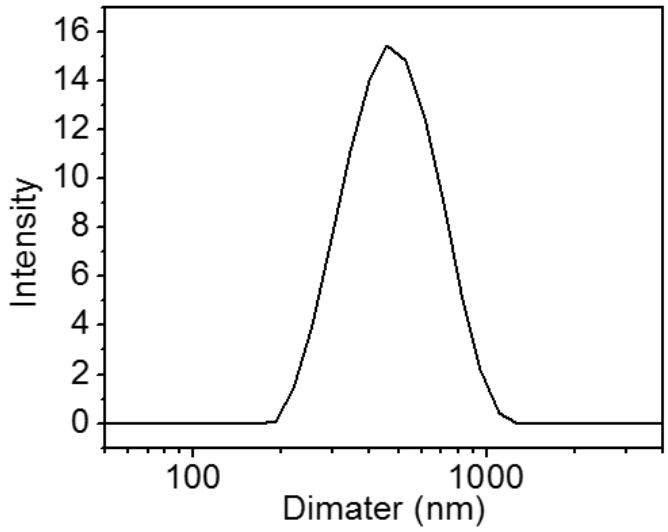

Figure 2.5. DLS spectrum of chain vesicles, indicating an average diameter of ~522 nm

The formation of chain vesicle or non-chain vesicle was largely dependent on

the densities (δ) of the polymer ligands on the surfaces of AuNPs. At low δ (0.03 chain/nm^2), the assembly process produced chain vesicles with a monolayer of AuNP chains in the vesicular membranes (Figure 2.43 a,b,e,and f). When NPs grafted with a higher δ (above 0.05 chain/nm^2) of BCPs were used, non-chain vesicles were formed with a monolayer of AuNPs of relatively uniform interparticle spacing in the vesicular membranes (Figure 2.4 c and d). The chain vesicle has an inner cavity that is separated from the environment by a monolayer membrane of AuNPs. The average diameter of the chain vesicles was 520 $\pm$ 170 nm, measured from DLS (Figure 2.5). This value is slightly smaller than the average diameter of 673 $\pm$ 233 nm obtained by TEM analysis. The larger value characterized by TEM was possibly due to the collapse and flattening of vesicles under vacuum conditions. The AuNP chains and chain network can be clearly observed in the vesicular membranes (Figure 2.4 a and b). The TEM images further confirmed that the vesicles were hollow and made from a monolayer of NP membranes (Figure 2.4 e and Figure 2.S1). By analyzing the TEM and SEM images of the vesicles, it was determined that the average separation distance between the chains within the vesicles was 12.3 $\pm$ 2.2 nm. The average number of AuNPs in chains within the vesicular membrane was 6.2 AuNPs per chain. In each chain, the NPs were in close contact with each other, and in some other cases, the AuNPs within one chain were even fused together (Figure 2.4 f and inset). We presume that the occurrence of fusion between adjacent AuNPs can be explained by a cold welding mechanism where gold atoms can diffuse by means of surface diffusion.[23] The hydrophobic interactions and the van der Waals interactions served as the attractive forces to facilitate the fusion between adjacent AuNPs. However, the

exact mechanism need to be furthered investigated. The average separation distance between AuNPs in each chain is 0.8 ± 0.1 nm, which is much smaller than that of 9.0 ± 1.5 nm between AuNPs in non-chain vesicles. The fusion and small interparticle distance between adjacent AuNPs within the chain vesicles led to a strong absorption in the NIR window, due to the strong coupling between AuNPs. Compared to non-chain vesicles made from the same sized AuNPs, chain vesicles have two distinct peaks locating at 545 nm and 780 nm, while the non-chain vesicles only have one absorption peak between 590 nm to 620 nm (Figure 2.6).

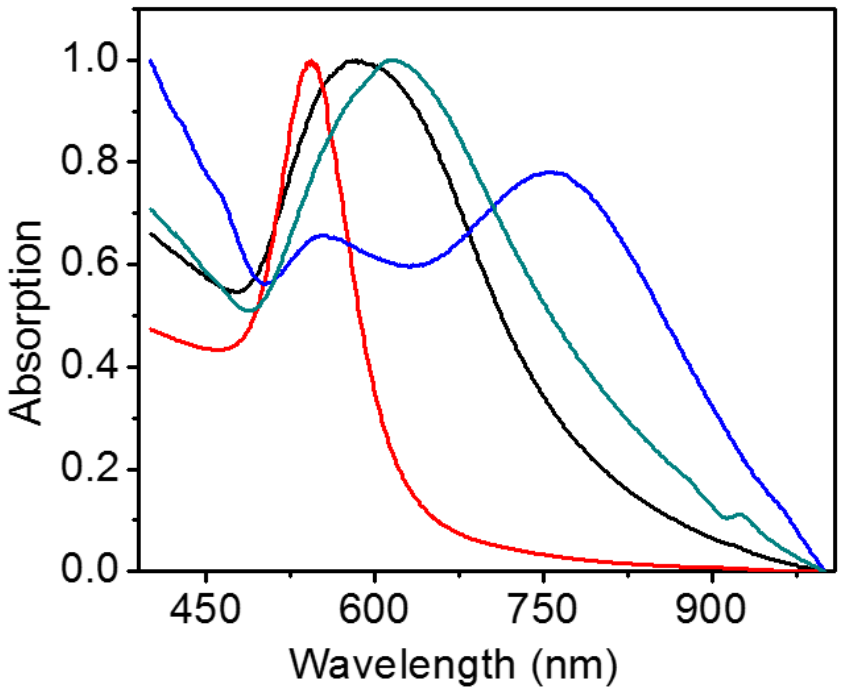

Figure 2.6. The UV-VIS spectra of individual AuNPs (red), chain vesicle (blue) and non-chain vesicles (black and green). The chain vesicles and non-chain vesicles were prepared by using BCP-AuNPs with δ of 0.03, 0.05, and 0.08 chain/nm^2, respectively.

2.3.2 Phase-like diagram

The assembly morphologies of the BCP-AuNPs (13) are strongly dependent on the δ and the quality of solvents (i.e. the water content in the water/THF mixture). The results of the systematic study are summarized in a phase-like diagram in Figure 2.7.

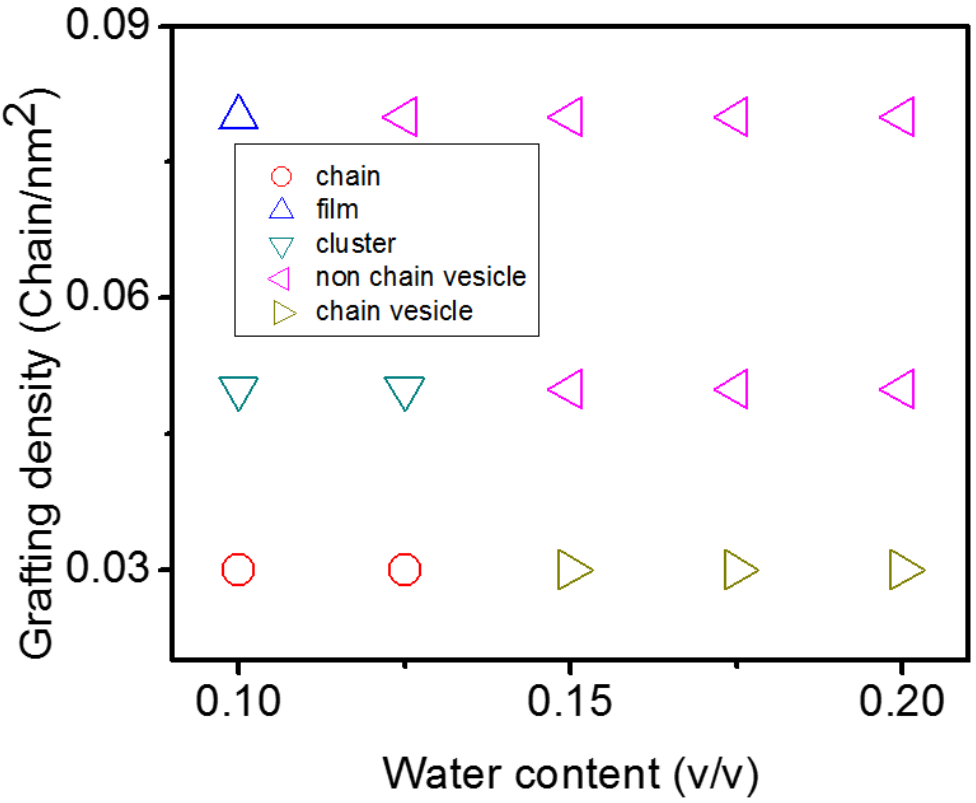

Figure 2.7. The phase-like diagram of self-assemblies of BCP-AuNPs (13) with varying grafting densities on the surfaces of AuNPs and water content. The different δ were 0.03, 0.05, and 0.08 chain/nm^2

First of all, the δ of BCPs on the surfaces of AuNPs plays a critical role in

controlling the assembly morphologies. The δ can be controlled by varying the ratio of polymers to AuNPs. Taking BCP-AuNPs in 100% water content as an example, when the δ was as low as 0.03 chain/nm^2, chain vesicles were formed. When the δ was above 0.08 chain/nm^2, BCP-AuNPs assembled into regular non-chain vesicles. Second, water content in the solvent also affects the assembly morphologies. To reveal the assembly process, aliquots of dispersions with different water content were examined by SEM. The BCP-AuNPs with low δ followed the above-mentioned two-step assembly process mechanism. When the water content was increased from 0% to 20%, the low δ BCP-AuNPs assembled into chains and transited into chain vesicles. For BCP-AuNPs with high δ, they first assembled into thin films with relatively uniform interparticle spacing and then formed into non-chain vesicles with increase in water content in the water/THF mixture (Figure 2.7 and Figure 2.8).[76] The BCP-AuNPs with intermediate δ (δ =0.05 chain/nm^2) assembled into small clusters and formed into non-chain vesicles. The BCP-AuNPs (13) with polymer grafting density lower than 0.03 chain/nm^2 either assembled into irregular structures or aggregated during the preparation. (Figure 2.9)

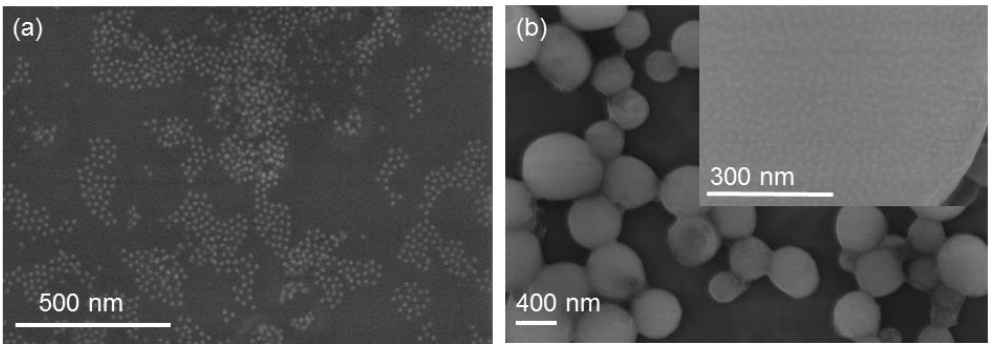

Figure 2.8. SEM images of the (a) films and (b) non-chain vesicles made from BCP-

AuNPs with a grafting density of 0.08 chain/nm^2 at different water content. The film sample was collected for SEM when water content was 10% in volume and the vesicle sample was collected for SEM when water content reached 20% in volume.

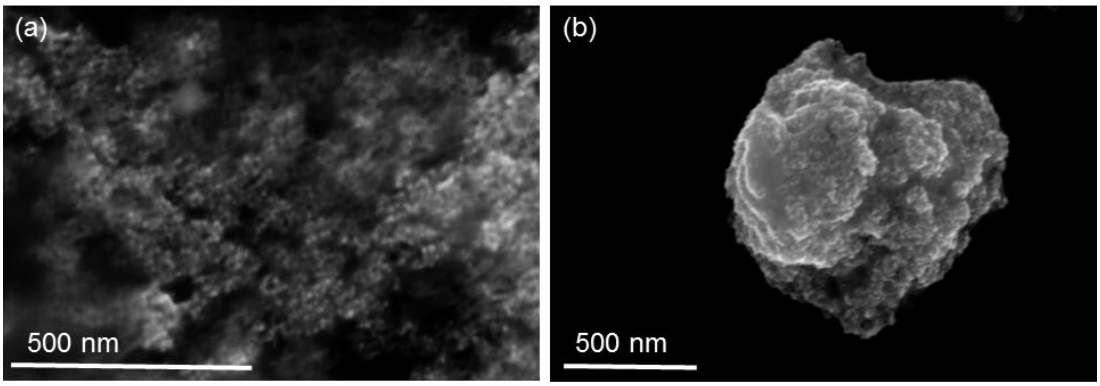

Figure 2.9. SEM images of irregular assemblies made from BCP-AuNP (13) with grafting densities below 0.03 chain/nm^2

2.3.3 Mechanism study of the self-assembly

We systematically investigated the formation mechanism of chain vesicles using UV-VIS spectroscopy and TEM. Water was stepwise (at an interval of 2 vol.%) added into the THF solution of BCP-AuNPs to trigger the self-assembly. UV-visible spectra were recorded 3 min after each addition of water (Figure 2.10 a). At 5 vol.% water, both TEM image and initial plasmon peak at 525 nm indicate that most BCP-AuNPs remained as individual NPs (Figure 2.10 b). With the increase of water content to ~10 vol.%, a new peak at 607 nm appeared along with the decrease in the plasmon peak at 525 nm. TEM characterization showed the formation of 1 D chains of AuNPs (Figure 2.10 c). The 1D AuNPs chains started to form when the water content reached 6~8

vol.%. TEM images of samples at 20 vol.% and 100 vol.% water content revealed that the assembly morphologies changed from 1D chains to vesicles. (Figure 2.10 d and Figure Figure 2.S2). This process was accompanied with the further red-shift of plasmon peak to 637 nm. These results suggested a two-step hierarchical self-assembly process: the formation of NP chains from individual NPs and subsequently assembly of NP chains into vesicles.

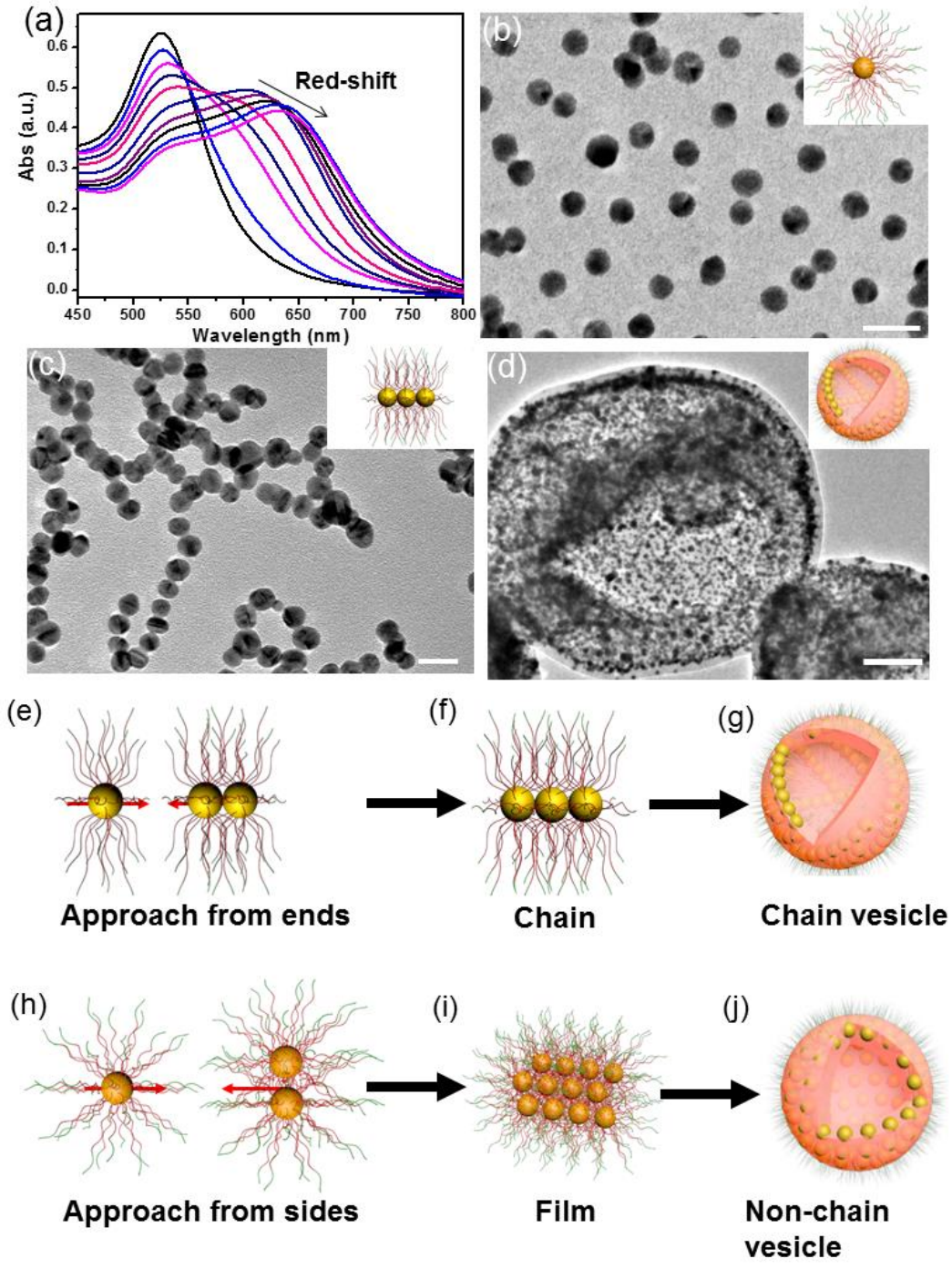

Figure 2.10. The self-assembly mechanism and kinetics study of BCP-AuNPs (13). (a) UV-vis spectra of BCP-AuNPs (13) at different water concentrations. The UV-vis spectra were recorded in the course of water addition (2 vol% interval). The addition

of water results in a significant reduction in the intensity of the 525 nm band, as well as a new absorption peak at 607 nm. The structural transition from 1 D chains to 3 D vesicles led to the red-shift of the new peak from 607 nm to 637 nm. (b-d) Representative TEM images of assemblies at 5, 10 and 100 vol% of water. The self-assembly presumably occurred in two steps, that is, the formation of 1D chains at lower water concentration and the transition of chains to vesicles at higher water concentration. Scale bars: 20 nm in (b) and (c), 100 nm in (d). Schematic illustration of the (e-g) chain vesicle forming mechanism and (h-j) non-chain vesicle forming mechanism

The competition in the formation of chain or non-chain vesicles can be explained as follows. At low polymer δ, the aggregates of two BCP-AuNPs had stronger steric repulsions from the sides than the ends due to the uneven distribution of polymers on the surfaces. As a consequence, individual NPs approached from ends of clusters of two NPs and aggregated in a linear mode to form chains (Figure 2.10 e). With the increase of water content, 1D chains were further assembled into vesicles. In contrast, when two NPs with high δ aggregated, the polymer steric repulsion prevented the third NP to get close to NP clusters. Individual NPs approached from the sides of clusters due to stronger hydrophobic interactions (Figure 2.10 h). Unlike most of previous reported 1D colloidal assemblies, the electrostatic repulsion is not the dominant repulsion force in chain forming process.[34,129,130] In those systems, enhancing the electrostatic repulsion prevents the NPs from aggregation while lowering the electrostatic repulsion induces global aggregation instead of linear

assembly. However, in our case, the assembly morphologies remained as chain vesicles when we dialyzed chain vesicle forming BCP-AuNPs against 500 mM NaCl solution to decrease the electrostatic repulsions. The smaller influence of electrostatic repulsions on 1D chain formation was due to the low dielectric constant of the mixed solvent of 10% of water in THF (12.59),[131] in which the chains were formed. In this solvent condition, the van der Waals interaction itself was strong enough to overcome the electrostatic repulsion. This can be proved by the fact that CTAB coated AuNPs without polymer ligands aggregated in this solvent condition with interparticle distance comparable to that in chains. Therefore, attractive interactions must be balanced by other repulsive interactions to ensure the linear assembly and we ascribe the repulsive interactions to the steric effect of the polymer chains. The root mean square end-to-end distance of the BCP was 11.7 nm.[78] The relatively long BCPs chain length compared to AuNP sizes and low polymer density provided the BCPs with the conformational flexibility needed for self-assembly.[75,76,99] The aggregation of first two chain-vesicle forming BCP-AuNPs led to ultrasmall interparticle distance. As a result, the BCP chains were squeezed out of gap between NP pairs, leading to higher polymer density around the center than the end of NP pairs (Figure 2.10 e). In poor solvent conditions, the collapsing coils of polymer chains are stabilized by three-body repulsion, which increase with the polymer density.[132] Therefore, the three-body repulsion at the center part of the NP pairs was stronger than that at the end. The stronger repulsion at the center prevented the additional BCP-AuNPs from getting close to the side and induced the formation of 1D chains (Figure 2.10 f). This was consistent with larger separation distance between chains (~12 nm) than that between

NP pairs (~0.8 nm) in the chain vesicles. With further addition of water, the chains of NPs become unstable, as a result of the relatively low density of hydrophilic PEO blocks. In order to minimize the interfacial tension arising from the interaction between PS and water, the chains of NPs interacted with each other to produce enclosed vesicles. There was a preference for chains to parallel with their neighboring chains in the vesicular membrane. We measured the angle between the chains from SEM images to calculate the average angle and separate them into four groups depending on the distances between the chains (Figure 2.11). Basically, we chose a point on the chain as the center and drew concentric circles with different diameters to group chains with different separation distance from the original chain. The angle between chains were measured by Image J.[133]

$$\text{The angle} = \begin{cases} x, & x < \pi/2 \\ 180 - x, & x \geq \pi/2 \end{cases} \quad \text{(Eq. 2.4)}$$

The average angle (~27^0) between two chains with smaller separation distance (< 30 nm) is smaller than that (~52^0) between two chains far away from each other (55~80 nm) (Figure 2.11). The folding of chains were also observed during the vesicle formation, which affected the parallel degree of neighboring chains.

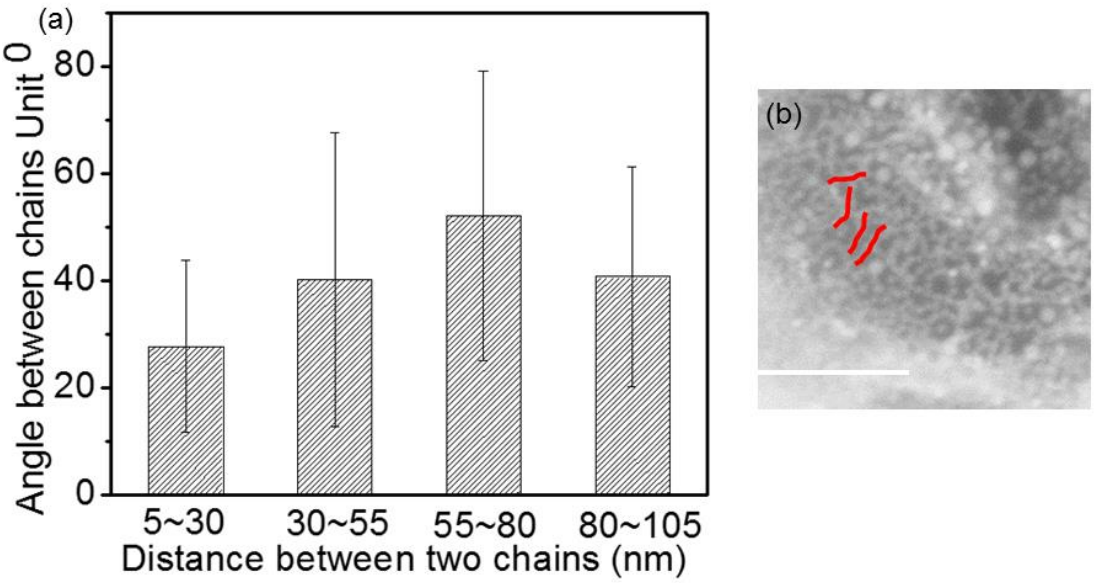

Figure 2.11. (a) The average angle between chains at different separation distances. (b) examples of NP chains in vesicular membrane with different orientations. Scale bars: 200 nm

We also conducted control experiments by using NPAMs with 22 nm core sizes (BCP-AuNPs (22)) or with 14 nm AuNP cores stabilized by sodium citrate instead of CTAB. We kept the same mass ratio of BCPs to AuNPs as we used in surface modification of 13 nm AuNP for chain vesicles. In both cases, non-chain vesicles were obtained (Figure 2.12). The ratio of BCP to the surface area of AuNPs is higher in the ligand exchange of BCP-AuNP (22) than that of chain vesicle forming BCP-AuNP (13). The resulting δ entered into the range of non-chain vesicles. In terms of sodium citrate stabilized AuNPs, higher δ was also achieved because the relatively weaker binding ability of sodium citrate to Au surfaces than CTAB led to higher percentage of ligands replacement by polymers. Then, we decreased the polymer

density on the surfaces of AuNPs that were initially stabilized by sodium citrate. The transition from non-chain vesicle to chain vesicle with the decreasing of polymer density was also observed (Figure 2.13). When AuNPs had lower δ than 0.03 chain/nm^2 on their surfaces, the BCP chains were not able to provide enough steric hindrance to overcome the strong wan der Waals forces, resulting in irregular assemblies. In summary, by adjusting the δ on the surfaces of NPs, we can control the competition between attractive forces and repulsive forces to determine the arrangement of AuNPs within the assemblies.

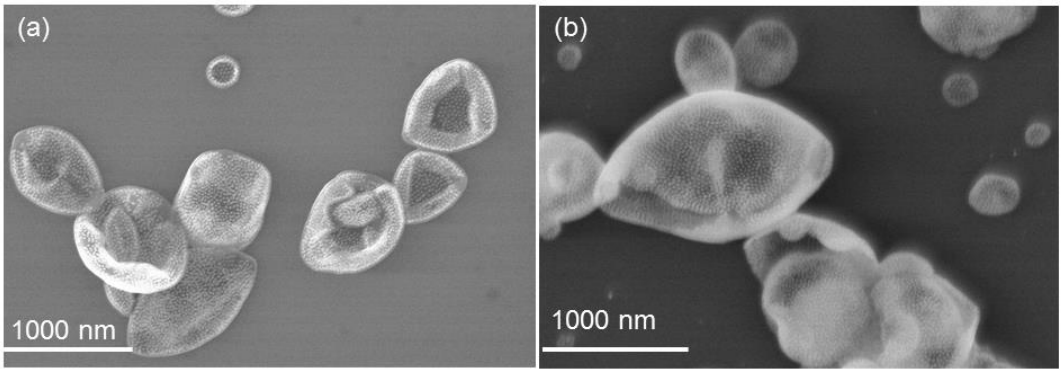

Figure 2.12. SEM images of non-chain vesicles made from (a) BCP-AuNPs (22) and 14 nm AuNPs with tethered BCPs that originally had sodium citrate as stabilize agent.

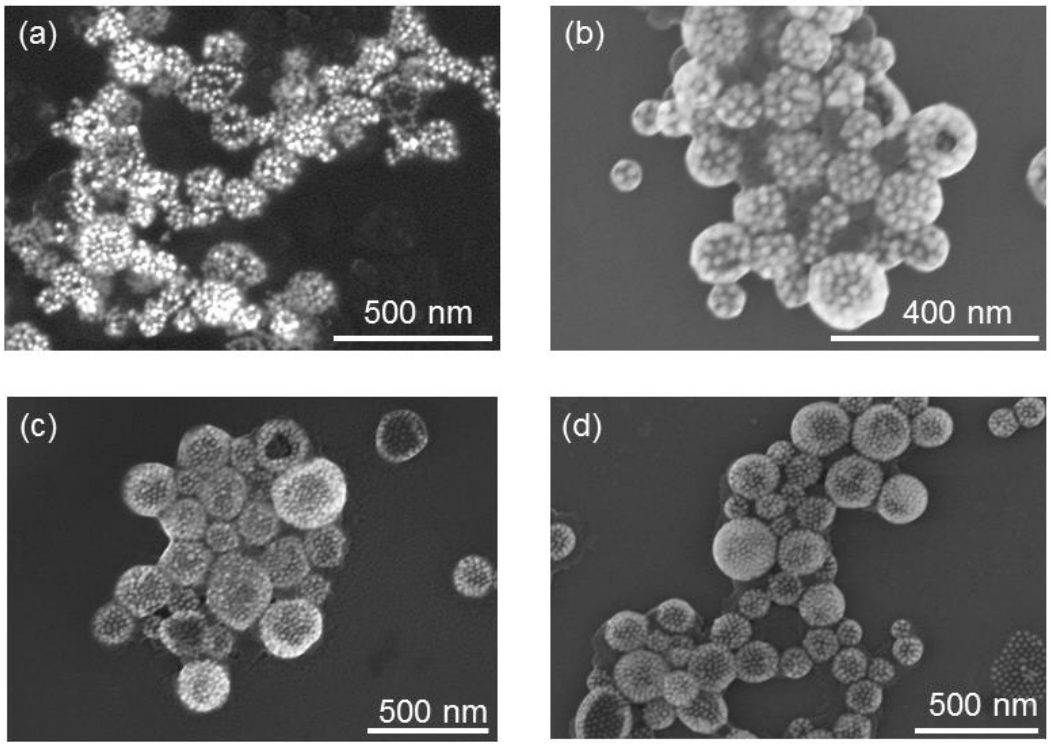

Figure 2.13. SEM images of vesicles made from BCP-AuNPs with BCP grafting density increasing from (a) to (d). The average size of AuNPs is ~20 nm and they were originally stabilized by sodium citrate. At low grafting density, the hybrid vesicles contained NP chains.

2.4 Photoacoustic imaging

For biological applications, it is crucial to fine-tune the absorption of nanostructures in the NIR wavelength which can penetrate tissues more deeply. The organization of AuNPs in a linear form in the membrane of vesicle resulted in the red-shift of plasmon peak from visible to NIR range, due to the stronger coupling between NPs compared to non-chain vesicles. This feature enables the superior performance of chain vesicles in imaging, drug delivery, and treatment. Au NPs can

absorb light and emit an acoustic wave. The acoustic wave can be detected by untrasonic detector to provide us the image of the localized area, which is the so-called photoacoustic (PA) imaging.[44] PA imaging of chain vesicles and non-chain vesicles were employed to compare their PA efficiency under 780 nm pulsed laser. The vesicles containing same amount of gold materials (50 μg) were injected into the mouse tissue by means of subcutaneous injection, where the laser was irradiated for the equal time. The chain vesicles showed eight fold enhancement in the PA signal after they were injected, while the non-chain vesicle only showed 1.1 times enhancement (Figure 2.14). This demonstrated that the stronger coupling between AuNPs in the chain vesicles was preferred in biomedical applications. This can be achieved through carefully adjusting the repulsive and attractive forces between AuNPs. We are currently working on decreasing the size of chain vesicles for biomedical applications.

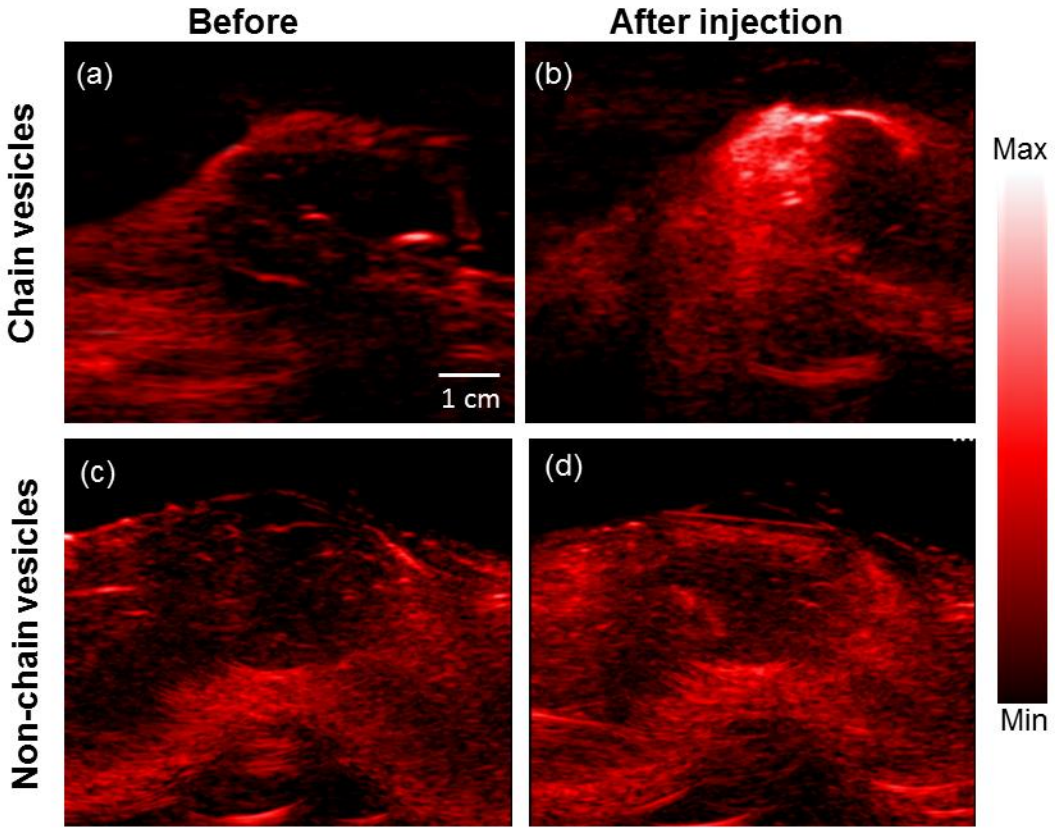

Figure 2.14. In vivo 2D PA imaging of mouse tissue before and after injection of chain vesicles (a, b) and non-chain vesicle (c,d).

2.5 Conclusions

We investigated the step-wise hierarchical self-assembly of BCP-AuNPs into vesicles of chains of NPs. We found that the δ of polymer ligands plays an important role in determining the assembly structures. The integration of strong plasmon coupling of 1D chain into vesicles led to the NIR absorption of the vesicles. Compared to non-chain vesicles, the chain vesicles showed higher efficiency in PA

imaging. The fundamental understanding of this assembly behavior can help us design new functional materials with desired structures and properties.

Chapter 3: Entropy-driven Pattern Formation of Hybrid Vesicular Assemblies Made from Molecular and Nanoparticle Amphiphiles

Overview. Although an analogy has been drawn between them, organic MAMs and inorganic NPAMs are significantly different in dimension, geometry, and composition as well as their assembly behavior. Their concurrent assembly can synergistically combine the inherent properties of both building blocks, thus leading to new hybrid materials with increasing complexity and functionality. Here we present a new strategy to fabricate hybrid vesicles with well-defined shape, morphology and surface pattern by co-assembling MAMs of BCPs and NPAMs comprising inorganic NPs tethered with amphiphilic BCPs. The assembly of binary mixtures generated unique hybrid Janus-like vesicles with different shapes, patchy vesicles, and homogeneous vesicles. Our experimental and computational studies indicate that the different nanostructures arise from the delicate interplay between the dimension mismatch of the two types of amphiphiles, the entanglement of polymer chains, and the mobility of NPAMs. In addition, the entropic attraction between NPAMs plays a dominant role in controlling the lateral phase separation of the two types of amphiphiles in the membranes. The ability to utilize multiple distinct amphiphiles to construct discrete assemblies represents a promising step in the self-assembly of structurally complex functional materials.

This chapter is adapted from the manuscript published in the following article: Liu,Y., Li, Y., He, J., Duelge, K., Lu, Z., ,and Nie, Z., Entropy-driven pattern formation of hybrid vesicular

assemblies of binary molecular and nanoparticle amphiphiles, *J. Am. Chem. Soc.*, **2014**, 136, 2602-2610

3.1. Introduction

Natural or synthetic amphiphiles such as lipids[134] and BCPs[135] represent one of the most prospective building blocks for constructing functional materials. MAMs can self-assemble into a rich variety of complex hierarchical nanoarchitectures with applications ranging from biomedicine, tissue engineering to electronics.[10,13,136,137] In contrast, inorganic NPAMs can exhibit intrinsic optical, electronic, and magnetic properties that are unattainable by their organic counterparts.[39,75,76] NPAMs are usually constructed by synthesizing NPs with distinct hydrophilic and hydrophobic regions or attaching amphiphilic molecules (i.e., BCPs) on the surfaces of inorganic NPs.[75,76,87] This new class of building blocks can self-assemble as better-studied molecules into defined nanostructures with various morphologies such as chains, micelles, vesicles, and tubules.[36,39,75,76,78,80-82,87] The organization of NPAMs enables one to fine-tune the synergetic coupling between subunits (i.e., semiconducting, metallic and magnetic NPs) within assemblies,[22] thus fully realizing the enormous potential of NPs in such as biomedicine,[45,138] energy,[139] and optoelectronics.[140]

Recently, the rapidly rising demand for new materials drives the design of nanostructures with increasing complexity and new functionality.[141-146] One promising strategy is to simultaneously assemble multiple types of amphiphiles into discrete architectures. Most examples involve the concurrent assembly of two or more MAMs of lipids, surfactants, and/or polymers.[100,134,142,147] The physical and chemical properties of these assembled structures are inherently limited by the nature of

organic species. The combination of organic MAMs and inorganic NPAMs can potentially surpass such limitations of assembled materials by imparting the system with summation or collective properties of all building blocks. However, the concurrent self-assembly of MAMs and NPAMs has rarely been explored, and their co-assembly behaviors are still unclear.[147] The Eisenberg group reported the concurrent self-assembly of free BCPs of PS_{320}-*b*-PAA_{47} and 4 nm AuNPs modified with PS_{270}-*b*-PAA_{15}. In the resulting hybrid vesicles, the AuNPs were located in the center of the entire hydrophobic membrane of polymer vesicles.[100] In a following study from the same group, the NPAMs were incorporated into the center of the cylindrical and spherical micelles. In these cases, as small AuNPs (less than 5 nm) were used, the thickness of vesicle membranes is similar to the sum of NPs diameter and the length of polymer ligands. We hypothesize that NPAMs with larger sizes will lead to different assembly morphologies and the cooperativity and complexity of concurrent self-assembly of MAMs and NPAMs will maximize our capability of creating novel hybrid assemblies with desired architectures and properties.

Here we report an experimental and computational study on the co-assembly of BCP amphiphiles and NPAMs comprising inorganic NPs tethered with amphiphilic linear BCPs in selective solvents (Figure 3.1). The binary mixtures of amphiphiles assembled into a variety of hybrid vesicles with well-defined shape, morphology and surface pattern by controlling the entropy-driven lateral phase separation of binary amphiphiles within membranes. Typical assembled nanostructures include patchy vesicles (PVs) with multiple small NPAM domains surrounded by MAM phase

(Figure 3.1 b), Janus-like vesicles (JVs) with distinguished MAM and NPAM halves (Figure 3.1 c-e), and homogeneous vesicles (HVs) with uniform distribution of NPAMs (Figure 3.1 f). The formation of different nanostructures arises from the delicate interplay between the dimension mismatch of the two types of amphiphiles, the entanglement of polymer chains, and the mobility of NPAMs. Additionally, the entropic attraction between NPAMs, as a result of the maximization of the conformational entropy of free BCP chains, plays a dominant role in controlling the phase-separation of the two types amphiphiles in the membranes. It is remarkable that this strategy allows the preparation of hybrid JVs with intriguing non-spherical shapes, including hemispherical (Figure 3.1 d) and disk-like shape (Figure 3.1 e). The ability to directly integrate multiple amphiphiles with significantly different dimensions, geometries, and compositions into discrete nanostructures opens new avenues to fabricate structurally complex hybrid materials with advanced properties.

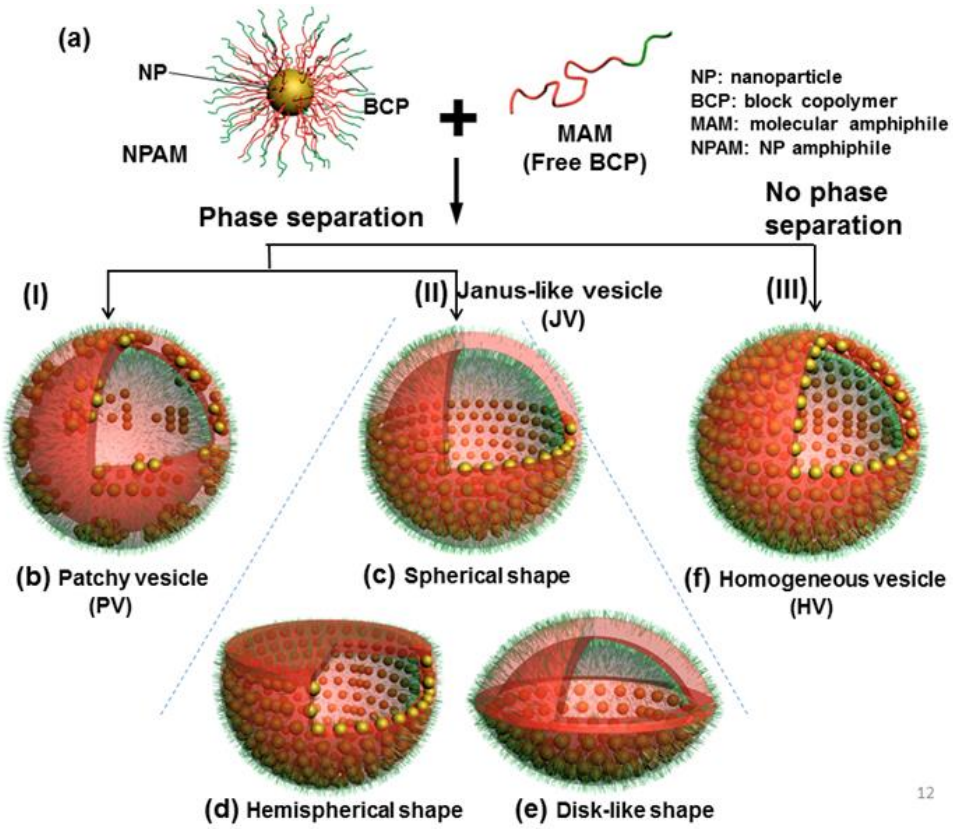

Figure 3.1. Schematic illustration of the co-assembly of binary mixtures of MAMs and NAPAMs into hybrid vesicles with defined shape, morphology and surface pattern. The NPAM consists of an inorganic NP tethered with amphiphilic linear BCPs, while free amphiphilic BCP is used as MAM (a). When phase-separation occurs (I and II), the concurrent assembly produces spherical hybrid PVs with multiple NPAM domains (b) and hybrid JVs with distinguished MAM and NPAM halves (c-e). The JVs acquire a spherical (c), hemispherical (d), and disk-like (e) shape depending on the assembly parameters. When no phase-separation occurs (III), the assembly generates HVs with uniform distribution of NPAMs in the membrane (f).

3.2 Experiments

3.2.1 Materials.

Styrene, AIBN, CPPA, THF, FDMF, sodium borohydride (NaBH4, ≥99%), gold(III) chloride trihydrate ($HAuCl_4$, ≥99.9% trace metals basis), sodium citrate tribasic dihydrate (≥99%), CTAB, Sodium oleate (NaOL), and silver nitrate ($AgNO_3$) were purchased from Sigma-Aldrich. PS-*b*-PEO (i.e., PS_{307}-*b*-PEG_5, PS_{307}-*b*-PEG_{45}, and PS_{307}-*b*-PEG_{383}) without thiol functional groups were purchased from Polymer Source, Inc.

3.2.2 Synthesis of thiol-terminated BCPs.

The synthesis of thiol-terminated PS-*b*-PEO is referred to the experimental section in Chapter 2.

3.2.3 Synthesis of sodium citrate covered AuNPs and CTAB covered AuNRs.

Sodium citrate AuNPs were synthesized using sodium citrate reduction method reported previously.[148] To make 19 nm AuNP, 1 mL of 10 mg/mL HAuCl4 aqueous solution and 3 mL of 10 mg/mL sodium citrate was injected into 500 mL of boiling water under stirring. After being refluxed for 30 min, the solution temperature was decreased to 85 ℃. Another 3 mL of sodium citrate solution and 1 mL of $HAuCl_4$ solution were injected. The reaction was maintained in 85 ℃ water bath for 15 min before it was cooled down to room temperature.

AuNRs were prepared using seed-mediated growth method as reported.[36] A seed

solution was first prepared by mixing 5 mL of 1.0 mM $HAuCl_4$, 2.5mL of H_2O, and 5.0 mL of 0.2 M CTAB, followed by injecting 0.6 mL of ice-cold 10 mM $NaBH_4$ under stirring. The grow solution were prepared by mixing 1.0 mL of 10 mM $HAuCl_4$,19.0 mL of 0.1 M CTAB, 0.2 mL of 10 mM $AgNO_3$, and 0.12 mL of 0.1 M ascorbic acid. A 0.32 mL seed solution was added into the growth solution with gently shaking. The solution was then set aside overnight at 28℃.

3.2.4 Surface modification of AuNPs.

Briefly, a 2 mg of thiol-terminated BCPs was dissolved in 10 mL of DMF. A 40 mL of aqueous solution of AuNPs was concentrated into 100 μL by centrifuge. The concentrated AuNP solution was slowly added into the above BCPs solution in DMF while shaking. Subsequently, the mixture was sonicated for 1 hr to avoid aggregation and then was kept undisturbed for 6 hours to complete the ligand exchange. To remove free BCPs, the solution centrifuged for eight times and redispersed in THF. The estimated free BCPs left in the system should be lower than 2×10^{-12} mg/mL.

3.2.5 Self-assembly of NPAMs.

The PS-*b*-PEO without thiol functional groups and NPAMs were dissolved in THF with predetermined concentration. Ultrapure water was added drop-wise into the mixture while vigorously stirring, until the final water content reached 25% by volume. The solution was shaken for 5 hr and then dialyzed against water using dialysis bags (M_w cutoff of 3000-5000 g/mol) for 24 hr to remove THF.

3.2.6 Dissipative particle dynamics (DPD).

The dissipative particle dynamics (DPD) simulation technique was proven to be a suitable and efficient method in the studies of self-assembly of NPs and BCPs. In DPD method, the time evolution of the interacting coarse-grained (CG) beads is governed by Newton's equations of motion[149]

$$\frac{d\vec{r}_i}{dt} = \vec{v}_i \,, \quad \frac{d\vec{v}_i}{dt} = \sum_{j \neq i} (\vec{F}^C{}_{ij} + \vec{F}^D{}_{ij} + \vec{F}^R{}_{ij}) = \vec{f}_i \quad . \qquad \text{(Eq. 3.1)}$$

Inter-bead interactions are characterized by pairwise conservative, dissipative, and random forces. They are

$$\vec{F}^C{}_{ij} = \alpha_{ij}(1 - r_{ij}/r_c)\vec{e}_{ij} \,, \quad \vec{F}^D{}_{ij} = -\gamma w^D(r_{ij})(\vec{e}_{ij} \cdot \vec{v}_{ij})\vec{e}_{ij} \,, \quad \vec{F}^R{}_{ij} = \sigma w^R(r_{ij})\theta_{ij}\vec{e}_{ij} \quad .$$

(Eq. 3.2)

Here, $\vec{r}_{ij} = \vec{r}_i - \vec{r}_j$, $r_{ij} = |\vec{r}_{ij}|$, $\vec{e}_{ij} = \vec{r}_{ij}/r_{ij}$, r_c is the interaction cutoff radius, and $\vec{v}_{ij} = \vec{v}_i - \vec{v}_j$. θ_{ij} is a random number with Gaussian distribution and unit variance. α_{ij} is the interaction parameter between beads *i* and *j*. The weight functions $w^D(r_{ij})$ and $w^R(r_{ij})$ of dissipative and random forces couple together to form a thermostat. Español and Warren showed the correct relation between the two functions,[150]

$$w^D(r_{ij}) = [w^R(r_{ij})]^2 \,, \sigma^2 = 2\gamma k_B T \,.$$

DPD-VV algorithm is used for numerical integration,[135] i.e.

$$\vec{v}_i \leftarrow \vec{v}_i + \frac{1}{2}\frac{1}{m}(\vec{F}_i^C \delta t + \vec{F}_i^D \delta t + \vec{F}_i^R \sqrt{\delta t})$$
$$\vec{r}_i \leftarrow \vec{r}_i + \vec{v}_i \delta t$$
$$\textit{Calculate} \quad \vec{F}_i^C(\vec{r}), \vec{F}_i^D(\vec{r}_i, \vec{v}_i^0), \vec{F}_i^R(\vec{r}) \quad . \qquad \text{(Eq. 3.3)}$$
$$\vec{v}_i \leftarrow \vec{v}_i + \frac{1}{2}\frac{1}{m}(\vec{F}_i^C \delta t + \vec{F}_i^D \delta t + \vec{F}_i^R \sqrt{\delta t})$$
$$\textit{Calculate} \quad \vec{F}_i^D(\vec{r}_i, \vec{v}_i)$$

In our simulations, we use reduced units and assume all CG beads are equal on volume. The bead mass and the temperature are set to be unity, i.e. $m = k_B T = 1$, and the cutoff radius $r_c = 1$. Polymers are constructed by connecting adjacent beads in the chain together via harmonic spring $\vec{F}_{ij}^S = -k\vec{r}_{ij}$, where $k = 4$. A time step of $\delta t = 0.02$ is used, and the total simulation steps are 10^6. We set the cubic box side length as 80, which represents 800 nm in experiment, and control the number density of coarse-grained beads at 3, so the total number of beads in our simulations is 1536000, which contains 125 $C_{90}(A_xB_y)_8$ polymer tethered gold nanoparticles (AuNPs) (that is, NPAMs), 2000 $A_{18}B_1$ free block copolymers (BCPs) (that is, MAMs), and the remaining part as water. All simulations are performed in NVT ensemble using GALAMOST on Nvidia Tesla C2050 GPU.[151]

3.2.7 Coarse-grained models.

In this work, we adopted 8 linear chains connected to a center NP core to form the composite system $C_{90}(A_xB_y)_8$, where the hydrophobic PS is denoted as type A and hydrophilic PEO is denoted as type B, and C_{90} represents the AuNPs, in which 90 CG beads form a spherical rigid body.[151] Each composite system contains N_b=8(x+y)+90

beads, in which *x* is the length of an A block, and *y* is the length of a B block.

Table 3.1. Molecular parameters in the system. The monomer volumes are calculated using the molecular weights and the experimental bulk densities at room temperature.

	Molecular weight M (g/mol)	**Density ρ (g/cm^3)**	**Monomer volume V (Å^3)**	**Monomer number per DPD bead**	**Coarse-grained bead volume V (Å^3)**
PS monomer	104	1.06	163	18×64	187776
PEO monomer	44	1.12	65	45×64	187200
Water	18	1.0	30	98×64	188160

To map onto the experimental systems, we choose an appropriate coarse-graining level for water, PEO, PS and AuNPs. The diameter of the rigid body C90 is 2.0 in our simulations, which represents 20-nm AuNP core in experiment. From experimental grafting density σ=0.1 *chains/nm^2*, we identify that the grafted chains per AuNP is about 512. In our simulations, we adopt 8 linear chains to model the grafted BCPs, so one linear chain in our simulations represents 64 adjacent polymer chains in experiment. According to the molecular weights and the bulk densities of the pure species in experiments, the volumes of the monomers can be obtained, as shown in Table S1. We group 98×64 water molecules, 45×64 PEO monomers and 18×64 PS monomers, respectively, into one CG bead. Therefore, the reference volume of one CG bead adds up to 188160 Å^3, 187200 Å^3 and 188160 Å^3 for water, PEO and PS, respectively. We vary the length of A and B blocks as A_3B_1, A_6B_1, $A_{12}B_1$, $A_{14}B_1$, $A_{17}B_1$, $A_{25}B_1$ in our simulations to characterize different lengths of PS block (Table S2), such as $PS_{54}PEO_{45}$, $PS_{108}PEO_{45}$, $PS_{216}PEO_{45}$, $PS_{252}PEO_{45}$, $PS_{306}PEO_{45}$, $PS_{450}PEO_{45}$ in experiments, respectively. The free BCPs are mapped onto $A_{18}B_1$ in our simulations to characterize $PS_{320}PEO_{45}$ in experiments.

Since PEO is miscible with water at almost any concentrations, and AuNP and PS is insoluble in water, α_{BS}=27, α_{CS}=80, and α_{AS}=120 are used in our simulations. We fix interaction parameter between the same type of beads at α_{ii}=25 to correctly describe the compressibility of water,[149] and set α_{CB}=α_{AB}=40 to describe the incompatibility between Au/PS and PEO components. Koutsos *et al.* found that the PS chains are weakly adsorbed on the gold substrate, so we set α_{CA}=30.[152]

Table 3.2. The simulation models and the corresponding experimental systems. AuNPs tethered linear amphiphilic BCPs of PS-b-PEO and free BCPs could self-assemble into Janus type vesicles, full-coverage vesicles, and micro-phase-separated vesicles in aqueous solution.

20 nm	Micro-phase-separated	Janus type	Janus type	Full-coverage	Full-coverage
Simulation	A_6B_1	$A_{12}B_1$	$A_{14}B_1$	$A_{17}B_1$	$A_{25}B_1$
Simulation	$PS_{108}PEO_{45}$	$PS_{216}PEO_{45}$	$PS_{252}PEO_{45}$	$PS_{306}PEO_{45}$	$PS_{450}PEO_{45}$
Experiment	13.9K	23.9K	25.7K	33.6K	49.3K
Experiment	$PS_{114}PEO_{45}$	$PS_{211}PEO_{45}$	$PS_{245}PEO_{45}$	$PS_{304}PEO_{45}$	$PS_{455}PEO_{45}$

3.2.8 Surface coverage calculation

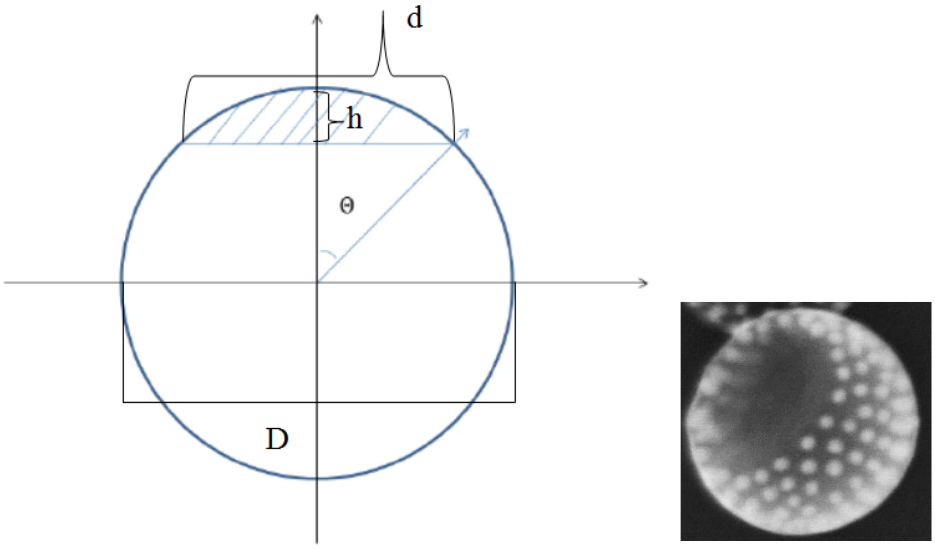

Figure 3.2. Schematic illustration of geometric parameters of a hybrid JV and SEM image of a hybrid JV.

The blank area is the 2-D projection of a hybrid Janus-like vesicle (JV) (Figure 3.2). Assuming that the polymeric domain remains spherical, the 2-D projection will be the shaded area plus the original blank area. From SEM or TEM images, the chord length of the shaded area (d) and the diameter of vesicles (D) can be measured.

$$sin\,\theta = \frac{d}{D} \quad \text{(Eq. 3.4)}$$

The surface area of shade part in the 3-D model is

$$S = \int dS_{shade} = \int_0^{\theta} d\theta' \int_0^{2\pi} d\emptyset\, R^2\, sin\,\theta' = 2\pi R^2(1 - cos\,\theta) \quad \text{(Eq. 3.5)}$$

where R is the radius of the vesicles (D/2) and $\emptyset$ is the azimuthal angle in spherical coordinates. The surface area of NPAMs in the JV is

$$4\pi R^2 - 2\pi R^2(1 - cos\,\theta) = 2\pi R^2(1 + cos\,\theta) \quad \text{(Eq. 3.6)}$$

Therefore, the ratio between surface areas of ACMs over entire surface areas of the assemblies is

$$P=\frac{2\pi R^2(1+\cos\theta)}{\frac{\pi d^2}{4}+2\pi R^2(1+\cos\theta)}. \qquad \text{(Eq. 3.7)}$$

3.2.9 Calculation of polymer grafting density on each NP

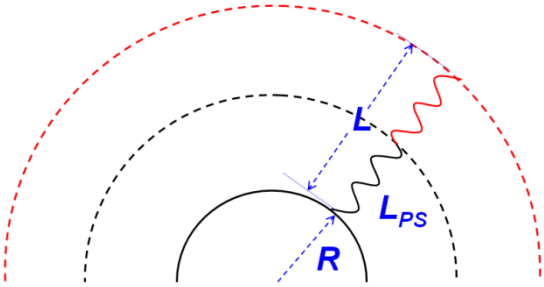

Figure 3.3. The schematic illustration of a NPAM. R is the radius of AuNPs, L is the thickness of BCPs, and L_{PS} is the thickness of PS layer.

We have estimated the number of grafted polymer chains (~0.10 chains/nm^2) using method we reported previously.[11] Taking Au-19-PS_{245}-*b*-PEO_{45} as an example, we can measure the average radius R of AuNPs and the overall radius, R+L of NPAM (Figure 3.3). The volume of grafted polymers is calculated using Eq. 3.8:

$$V_{polymer}=\frac{4\pi}{3}\left[\left(R+L\right)^3-R^3\right] \qquad \text{(Eq. 3.8)}$$

Using the M_n of PS_{245}-*b*-PEO_{45} 25.7 kg/mol, the average number of polymer chains on each AuNP is calculated from Eq. 3.9.

$$N_{polymer}=\frac{\rho V_{polymer}N_{Av}}{M_n} \qquad \text{(Eq. 3.9)}$$

where ρ and N_{Av} are the density of polymer and the Avogadro number, respectively. We assume the polymer density is close to the bulk density of polystyrene 1.05 g cm^{-3}. This value gives the average grafting density (σ) of 0.10 chains/nm^2.

3.3 Results and discussion

3.3.1 Self-assembly of binary MAMs and NPAMs.

The NPAMs used for assembly were prepared by tethering thiol-terminated amphiphilic linear BCPs of PS-*b*-PEO on the surfaces of AuNPs through ligand exchange.[8,11] Free amphiphilic BCPs of PS-*b*-PEO without thiol groups were used as MAMs to co-assemble with NPAMs. To optimize the assembly structures, a systematic study was conducted by using different sizes of AuNPs and lengths of individual blocks of tethered and free BCPs. The co-assembly system of NPAMs and MAMs were denoted as Au-D-PS_{x1}-*b*-PEO_{y1}/PS_{x2}-*b*-PEO_{y2}, where D is the diameter of AuNPs, and x_1, y_1, x_2 and y_2 are the repeating units of individual blocks of tethered and free BCPs, respectively. The characterization details of BCPs are summarized in Table 3.3.

Table 3.3. Characterization of amphiphilic BCPs used for self-assembly.

PSx_1-b-$PEOy_1$	x1	y1	M_n (kg/mol)^{GPC}	M_n (kg/mol)^{NMR}	PDI
1	114	45	9.7	13.9	1.11
2	211	45	16.0	23.9	1.15
3	245	45	18.1	25.7	1.12
4	304	45	24.0	33.6	1.2
5	455	45	30.2	49.3	1.18
PS_{x2}-*b*-PEO_{y2}	x2	y2	M_n (kg/mol)^{GPC}		PDI
1	307	5	32.2		1.06
2	307	45	34		1.04
3	307	383	49		1.06
4	678	80	73.5		1.10

M_n (kg/mol) ^{GPC}: the number-average molecular weight determined by GPC using plystyrene standards for calibration. M_n (kg/mol) ^{NMR}: the molecular weight calculated from ^{1}H NMR measurements. PDI stands for polydispersity index.

The co-assembly of two types of amphiphiles was triggered by adding water, which is a selective solvent for NPAMs and MAMs, into the binary mixtures of amphiphiles in THF, followed by dialysis against deionized water to remove THF. The assemblies of these binary amphiphiles were hybrid vesicles with various morphologies, namely, JVs (Figure 3.3 a-d), PVs (Figure 3.3 e), and HVs (Figure 3.3 f), depending on the size of NPAMs and the length of constituent blocks of both free and tethered BCPs. Since the BCP tethers and free BCPs were both PS-*b*-PEO, the entropy contribution towards the over free energy gain became critical in the course of assembly. In this case, the non-absorbing free BCPs (that is, MAMs) served not only as building blocks participating in the assembly, but also as depletant to induce short-range attraction between NPAMs due to depletion effect.[27] The depletion interactions excluded the MAMs from pairs of NPAMs, and hence increased the conformational entropy of the MAMs, which reduced the overall free energy of the system. This resulted in the lateral phase separation of MAMs with NPAMs within

the 2D vesicular membranes. When the MAMs and NPAMs strongly segregated, the assembly produced JVs comprised distinguished halves of the two types of amphiphiles with a sharp boundary (Figure 3.4 a-d). Otherwise, the assembly of binary amphiphiles generated PVs with many small NPAM domains surrounded by a continuous MAM domain (Figure 3.4 e), or HVs with uniform distribution of NPAMs in the membranes (Figure 3.4 f). Nevertheless, the dominant role of entropy in assembly conceptually differs our system from any existing concurrent assembly of pure organic MAMs.

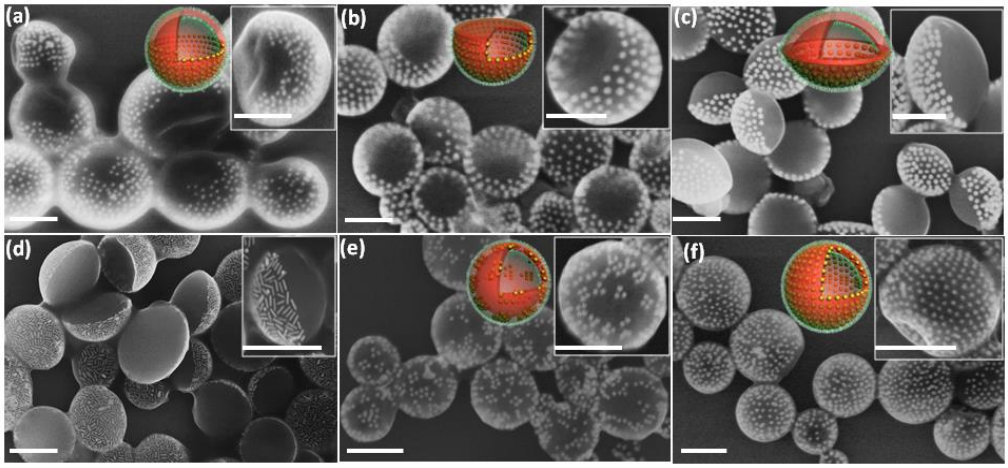

Figure 3.4. The co-assembly of binary mixtures of MAMs and NPAMs into hybrid vesicles. (a-d) Representative SEM images of JVs with spherical shape (a), hemispherical shape (b), and disk-like shape (c,d). SEM images of PVs (e) and HVs (f). The hybrid vesicles were assembled from a mixture of MAMs and NPAMs: (a) Au-19-PS_{245}-b-PEO_{45}/PS_{307}-b-PEO_{45}, (b) Au-19-PS_{211}-b-PEO_{45}/PS_{307}-b-PEO_5, (c) Au-40-PS_{455}-b-PEO_{45}/PS_{307}-b-PEO_5, (d) Au-40 (rods) –PS_{455}-b-PEO_{45}/PS_{307}-b-PEO_5, (e) Au-19-PS_{114}-b-PEO_{45}/PS_{678}-b-PEO_{80}, and (f) Au-19-PS_{455}-b-PEO_{45}/PS_{307}-b-PEO_5. All the self-assemblies were conducted in a water/THF mixture (1:3 in volume ratio).

The scale bars: 400 nm in (a), 150 nm in (b), 200 nm in (c,e,f), and 600 nm in (d).

Non-spherical vesicles represent the complexity of lipid-based biological membranes.[1] However, the formation of non-spherical vesicles is rare in a polymer or NP system.[34] Remarkably, the co-assembly of binary amphiphiles allows us to tune the shapes of vesicles, thanks to the unique characteristics (i.e., dimension, bending modulus, rigidity) of NPAMs. We ascribe the non-spherical shapes of hybrid JVs to the interplay of bending modules and line tension of multiple domains of NPAMs and MAMs. For example, the assembly of Au-19-PS_{245}-*b*-PEO_{45}/PS_{307}-*b*-PEO_{45} generated JVs with a spherical shape (Figure 3.4 a). When the lengths of free and tethered BCPs were changed, a binary mixture of Au-19-PS_{211}-*b*-PEO_{45}/PS_{307}-*b*-PEO_5 assembled into JVs with hemispherical shape (Figure 3.4 b). The bowl-like body of such vesicles was constructed from the rigid NPAMs, while a nearly flat polymer membrane covered the bowl to form enclosed vesicular compartments (see atomic force microscopy characterization in Figure 3.4). When the size of NPAMs (or the NP core of NPAMs) increased, the bending module of NPAM membranes increased. As a result, the curvature of the NPAM membranes decreased to release the bending energy, resulting in the formation of disk-like hybrid JVs with two symmetric halves for the Au-40-PS_{455}-*b*-PEO_{45}/PS_{307}-*b*-PEO_5 system (Figure 3.4 c,d).[154] The exact mechanism is still unclear and need further exploration in future research.

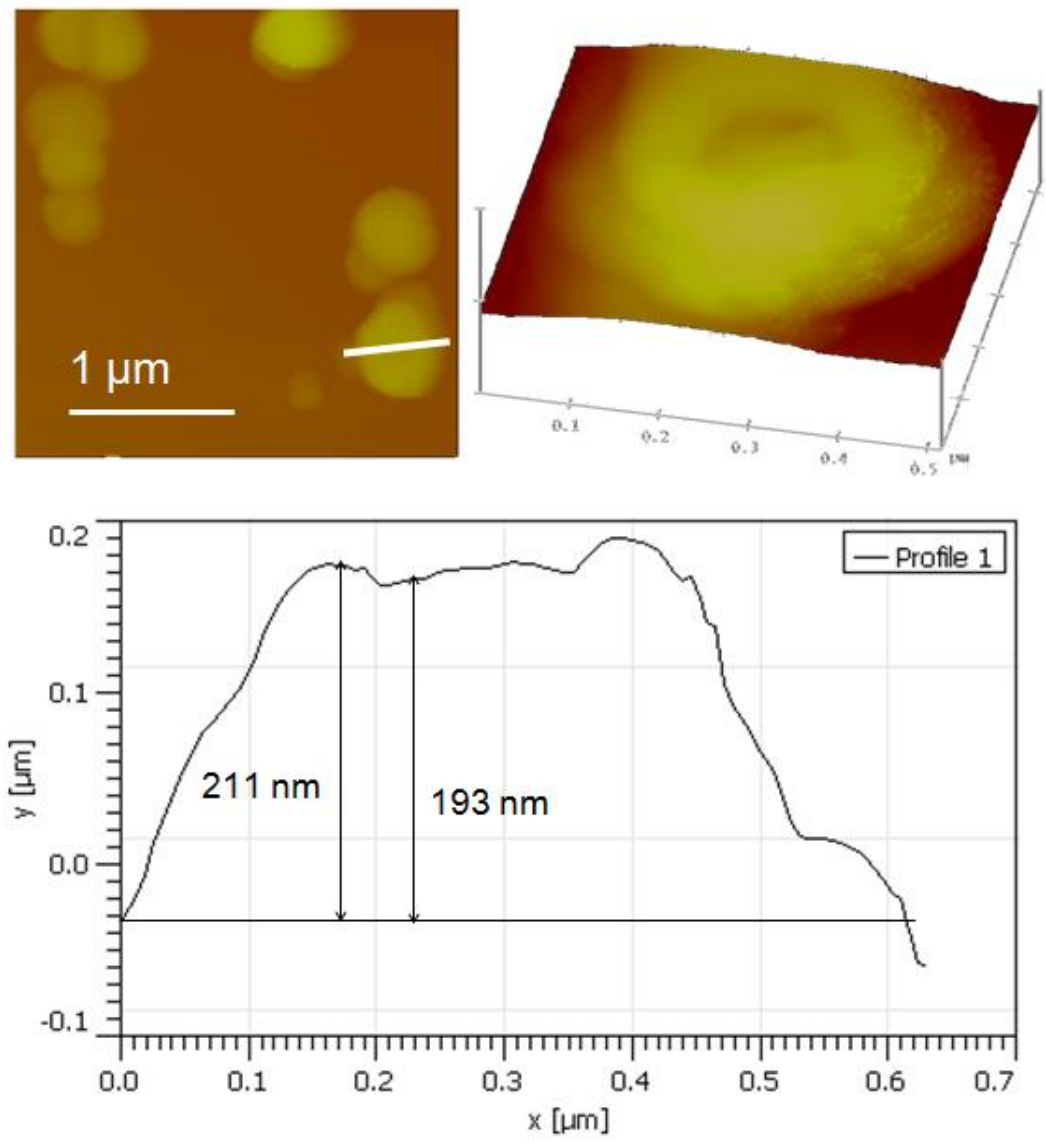

Figure 3.5. AFM images of hemispherical hybrid JVs assembled from Au-19-PS_{211}-*b*-PEO_5/PS_{307}-*b*-PEO_5. Given a 193-nm height of the overall vesicle, an 18-nm vertical topological difference between the edge and the center indicates the presence of a relatively flatten polymeric domains to seal the bowl-like NPAM domain.

3.3.2 Structural characterizations of hybrid JVs.

The hybrid JVs constituted a hollow interior constructed from binary mixtures of amphiphiles with significantly different dimensions, geometries, and compositions. The NPAM half of hybrid JVs was made from a monolayer of densely packed AuNPs with relatively uniform spacing (Figure 3.6 a-c).Taking hemispherical hybrid JVs assembled from Au-19-PS_{245}-*b*-PEO_{45}/PS_{307}-*b*-PEO_5 system as an example (Figure 3.6 b), we characterized the hollow interior and Janus-like morphology of the vesicles using various transmission electron microscopy (TEM) techniques (Figure 3.6 d-h).

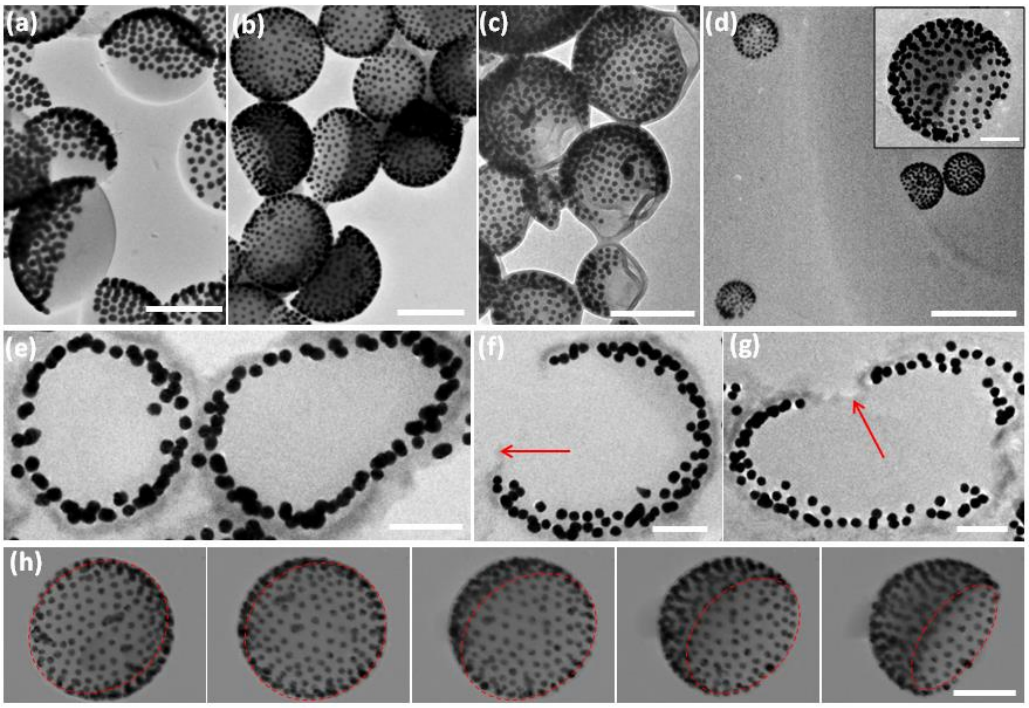

Figure 3.6. TEM characterization of hybrid JVs. (a-c) Representative TEM images of JVs with disk-like (a), hemispherical (b), and spherical (c) shapes. (d) Cryo-TEM image of hemispherical JVs. (e-g) TEM images of microtome sections of hybrid JVs

along different slicing directions: crossing the NPAM half only (e) and crossing both the NPAM and MAM halves (f,g). The red arrow indicates the location of polymer domains in the membranes of vesicles. (h) Tomographic TEM images of JVs at different tilting angles (left to right: -42 °, -22 °, -2 °, 38 °,and 50 °). The hybrid JVs are assembled from a binary system of (a) Au-40-PS_{455}-*b*-PEO_{45}/PS_{307}-*b*-$PEO_{5,}$ (b,d,e-h) Au-19-PS_{245}-*b*-PEO_{45}/PS_{307}-*b*-PEO_5, and (c) Au-19-PS_{245}-*b*-PEO_{45}/PS_{307}-*b*-PEO_{45}. All the self-assemblies were conducted in a water/THF mixture (1:3 in volume ratio). The scale bars are 500 nm in (a,d), 300 nm in (b,c), 100 nm in (e-h) and in the inset of (d).

First, Cryogenic TEM (cryo-TEM) image clearly showed the presence of hemispherical vesicles with a single layer of AuNPs in solution (Figure 3.6 d). Second, the hollow feature was demonstrated by the ring-like array of AuNPs in microtome sections of JVs (Figure 3.6 e-g). Depending on the slicing direction of JVs, the cross-section of JVs appeared as either a completely closed ring (Figure 3.6 e) or a non-closed ring with an opening (that is, a portion with the absence of AuNPs) which was corresponding to the MAM domain of hybrid JVs (Figure 3.6 f,g). The membrane thicknesses of the MAM and NPAM domains were roughly estimated to be ca. 20.8 nm and ca. 39.1 nm, respectively. The single array of AuNPs in the rings further confirmed that the NPAM domains of the vesicles consisted of a single layer of densely packed AuNPs. Third, electron microscopy tomography was used to record TEM images of HJVs at multiple tilt angles (−42° to 50°) (Figure 3.5 h). A series of tomographic TEM images illustrated the orientations of JVs with the MAM domain facing different directions. In addition, a close inspection of JVs with intact

and broken membranes of the polymer half further confirmed the hollow cavity of the vesicles, as well as the presence of the polymer domain in the vesicular membranes (Figure 3.7 and 3.8).

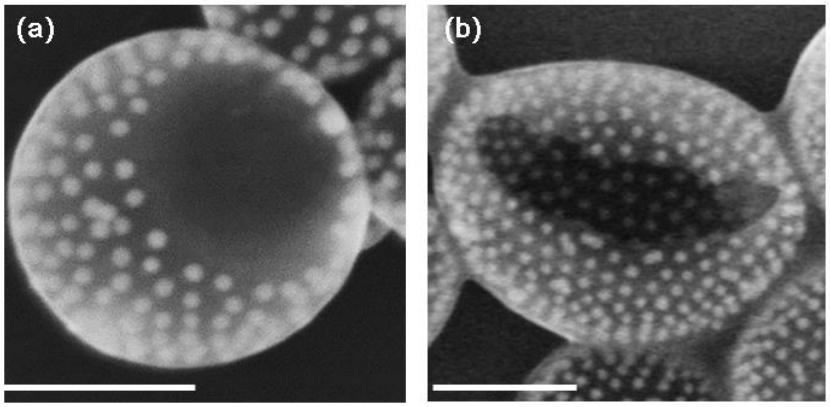

Figure 3.7. SEM images of hemispherical hybrid JVs with intact (a) and broken membranes (b) of the polymer half. Hemispherical hybrid JVs are assembled from Au-19-PS_{211}-*b*-PEO_{45}/PS_{307}-*b*-$PEO_{5.}$ Scale bar: 200 nm

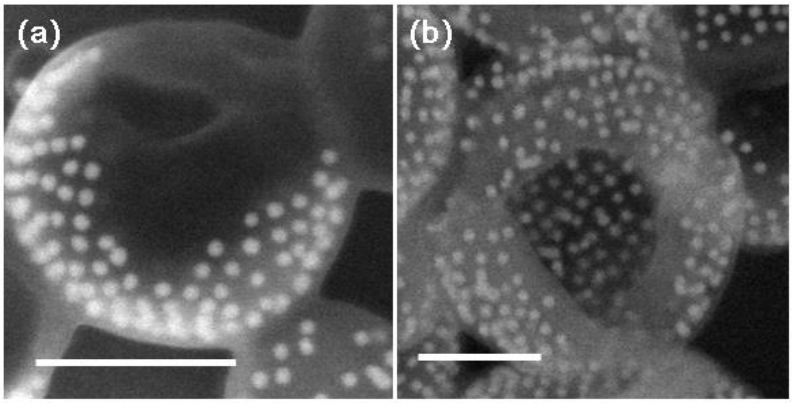

Figure 3.8. SEM images of spherical hybrid JVs with intact (a) and broken membranes (b) of the polymer half. Spherical hybrid JVs are assembled from Au-19-PS_{245}-*b*-PEO_{45}/PS_{307}-*b*-$PEO_{45.}$ Scale bar: 200 nm

The surface area ratio of the two halves of hybrid JVs can be readily controlled by NPAMs in the mixture, while keeping the amount of MAMs as a constant. With the increase of NPAM concentration from 0.21, to 0.45, and to 0.90 mg/mL, the surface fraction of NPAM half in hybrid JVs increased from 27.4%, to 38.1%, and to 85.9% (Figure 3.9). The JVs maintained a hemispherical shape, while varying the surface fraction of two halves.

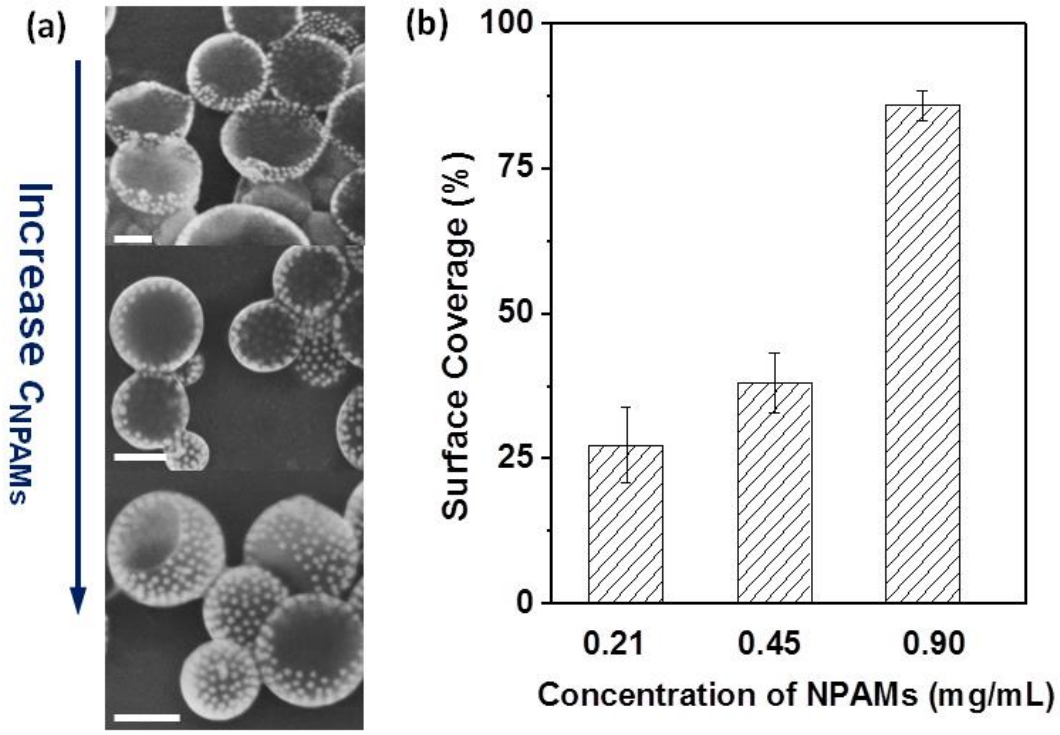

Figure 3.9. Control over the surface area ratio of two different halves of hybrid JVs assembled from Au-19-PS_{211}-*b*-PEO_{45}/PS_{307}-*b*-PEO_5. (a) SEM images of assemblies of binary mixtures of amphiphiles with different concentrations of NPAMs: 0.21 mg/mL, 0.45 mg/mL, and 0.9 mg/mL (from the top to the bottom). (b) Column diagram demonstrating the surface coverage of NPAMs in assemblies at different concentrations of NPAMs. Scale bar: 150 nm

3.3.3 Experimental and computational studies on assembly kinetics.

We studied the kinetics of the formation process of hybrid JVs using a system of Au-19-PS_{211}-*b*-PEO_{45}/PS_{307}-*b*-PEO_5 as an example. Time-dependent dynamic light scattering (DLS) measurement shows the evolution of hydrodynamic radius (R_h) of the assemblies in the mixed solvents (Figure 3.10). About 30 min after the addition of water, two populations of assemblies with R_h of ca. 91.5 and ca. 299.5 nm were presented in the system. They corresponded to small clusters of NPAMs and relatively big vesicles with randomly distributed MAMs and NPAMs in the membranes, as confirmed by SEM characterization (Figure 3.11 a). With time, the population of clusters gradually disappeared, accompanied with an increase in the diameter of vesicles (Figure 3.10 a, and Figure 3.11 c). This can be explained by the fusion of clusters with vesicles, in order to reduce the unfavorable exposure of hydrophobic constituents of small clusters of NPAMs, and hence minimize the overall interfacial free energy of the system. About 130 min after the assembly, only one population of assemblies with R_h of ca. 313 nm was presented in the system. The NPAMs within the vesicular membranes laterally migrated and packed more closely to each other, resulting in the formation of hybrid JVs with distinguished two halves. In a word, the concurrent assembly involves three critical steps, namely, initiation of assembly, fusion of nanostructures, and phase separation of two types of amphiphiles within membranes (Figure 3.11).

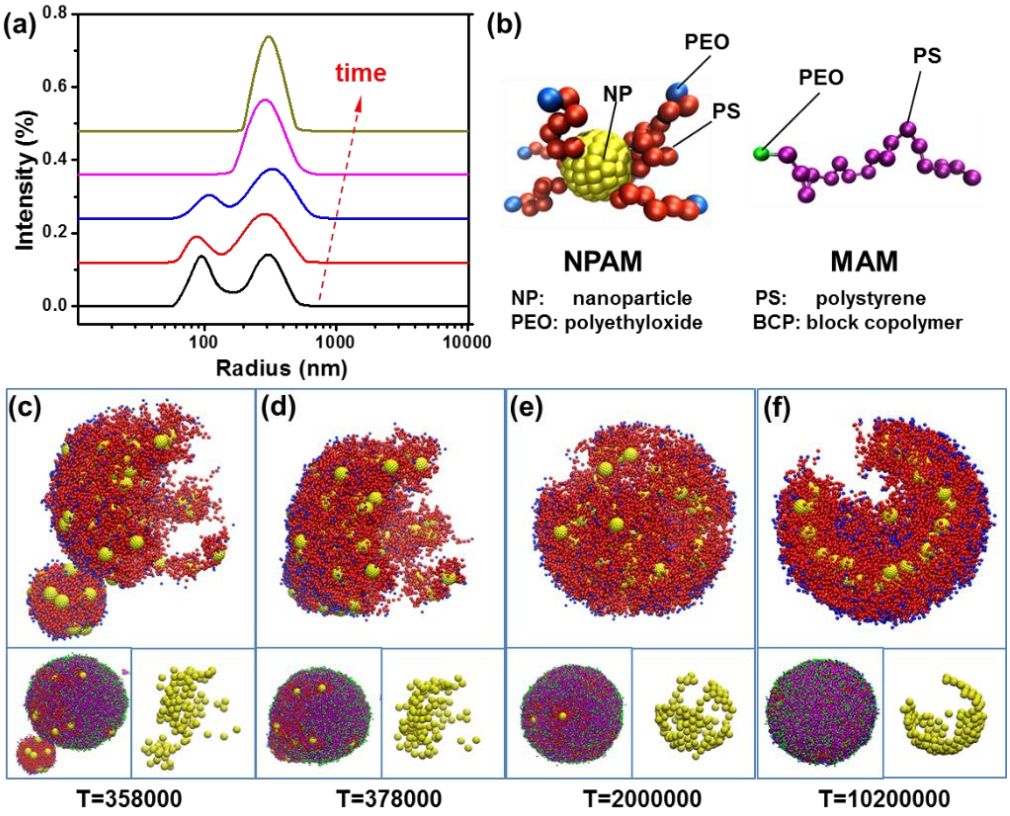

Figure 3.10. The kinetics of the co-assembly of MAMs and NPAMs into hybrid JVs in selective solvents. (a) Time-dependent DLS measurements of the assembly of the two types of amphiphiles after different times of assembly: (from bottom to top) 30, 40, 70, 130 and 190 min after the addition of water to the system. The hybrid vesicles were assembled from Au-19-PS_{211}-*b*-PEO_{45}/PS_{307}-*b*-PEO_5 in a water/THF mixture (1:3 in volume ratio). (b) Schematic illustration of binary amphiphiles used in DPD simulation. (c-f) Snap-shots of DPD-simulated assembly of the binary amphiphiles at different simulation times: T=358,000 (c), T=378,000 (d), T=2,000,000 (e), and T=10,200,000 (f). The snap-shots show the fusion of NPAM clusters and vesicular assembly, and the lateral phase-separation of NPAMs and MAMs in the vesicular membrane to form hybrid JVs.

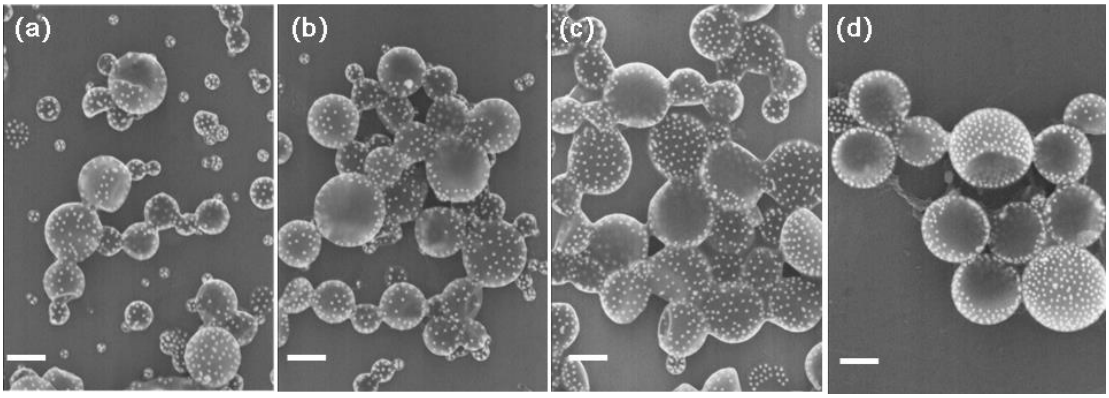

Figure 3.11. SEM images of the time-dependent assembly of the binary mixtures of Au-19-PS_{211}-*b*-PEO_{45}/PS_{307}-*b*-PEO_5. SEM images were taken at (a) 30 min, (b) 70 min, (c) 190 min after addition of water into the solution, and (d) after the dialysis against water. At 30 min small the assemblies were a mixture of clusters of NPAMs and relatively big vesicular assemblies with randomly distributed NPAMs in the membranes. With time, small clusters gradually disappeared, accompanied with the increase in the diameter of vesicles. At 190 min, the majority of assemblies were hybrid JVs. Scale bars: 200 nm.

We simulated the co-assembly of binary amphiphiles by dissipative particle dynamics (DPD),[148,150] using a coarse-grained (CG) model.[155,156] Note that our simulation model did not take into account the shapes of vesicles at present stage. Figure. 3.10 b illustrates the model of NPAMs containing AuNP cores tethered with amphiphilic linear BCPs, and MAMs of free BCPs (see Tables 3.1 and 3.2 for details). Our simulation confirmed the three critical steps of the formation of HJVs. Snap-shots of the simulation in Figure 3.10 c-f clearly show the fusion of NPAM clusters with vesicular assemblies, and the subsequent phase separation of binary amphiphiles within individual vesicles. We noticed that the fusion of the clusters and vesicles took

place rapidly in the simulation. In contrast, the lateral phase separation of binary mixtures of amphiphiles was rather slow to rearrange their organization in the membranes, due to the slow diffusion rate of relatively large NPAMs.

3.3.4 Phase separation behaviors of binary mixtures of amphiphiles confined in the vesicular membranes.

The phase separation behaviors of assembly of two types of amphiphiles as well as resulting assembly morphologies were strongly dependent on the relative length of individual blocks of free and tethered BCPs.[99] The results of our systematic study were summarized in a phase-like diagram in Figure 3.12 a. First of all, the PS length of tethered BCPs of NPAMs played a critical role in the phase separation of binary amphiphiles during assembly. Taking binary system with MAMs of PS_{307}-*b*-PEO_5 (M_w of PS is 32 kDa and M_w of PEO is 200 Da) as an example, when the PS length of tethered BCPs was relatively short (i.e., a M_w of 11.9, 21.9, and 23.7 kDa), a strong phase separation between binary amphiphiles occurred to generate hybrid JVs with two distinguished halves (Figure 3.12 a and Figure 3.13 a and b). When the PS length of tethered BCPs was long (i.e., a M_w of 31.6 k and 47.3 k), NPAMs were uniformly distributed in the MAM membrane to form hybrid HVs (Figure 3.13 c and d). In this case, the interparticle spacing between AuNPs within assemblies of binary amphiphiles was 16 nm, which was much larger than 9 nm for that of pure NPAM assembly system. This indicated that the MAMs were filled in-between NPAMs within vesicular membranes. Second, the PEO length of MAMs also influenced the morphologies of assemblies of the two types of amphiphiles. For a system with Au-

19-PS_{211}-*b*-PEO_{45} as NPAMs, when MAMs with short PEO blocks (i.e., a M_w of 0.2 and 2 kDa) were used, the binary mixture of amphiphiles strongly segregated in the membranes to generate

JVs. For MAMs with longer PEO blocks (i.e., M_w of 17 kDa) were used, their co-assembly with NPAMs carrying any length of tethered BCPs produced PVs with many small NPAM domains surrounded by a continuous phase of MAMs in the membranes. Our DPD simulation results were in good agreement with the experimental observations. The assemblies transited from PVs, to JVs, and to HVs eventually, when the PS length of tethered BCPs increased from 11.9 to 47.3 kDa (Figure 3.12 b-d). All the assembled structures observed in our experiments and simulations are reproducible, which manifests the stability of JV, PV, and HV characteristics. This also implies that the observed structures are equilibrium structures.

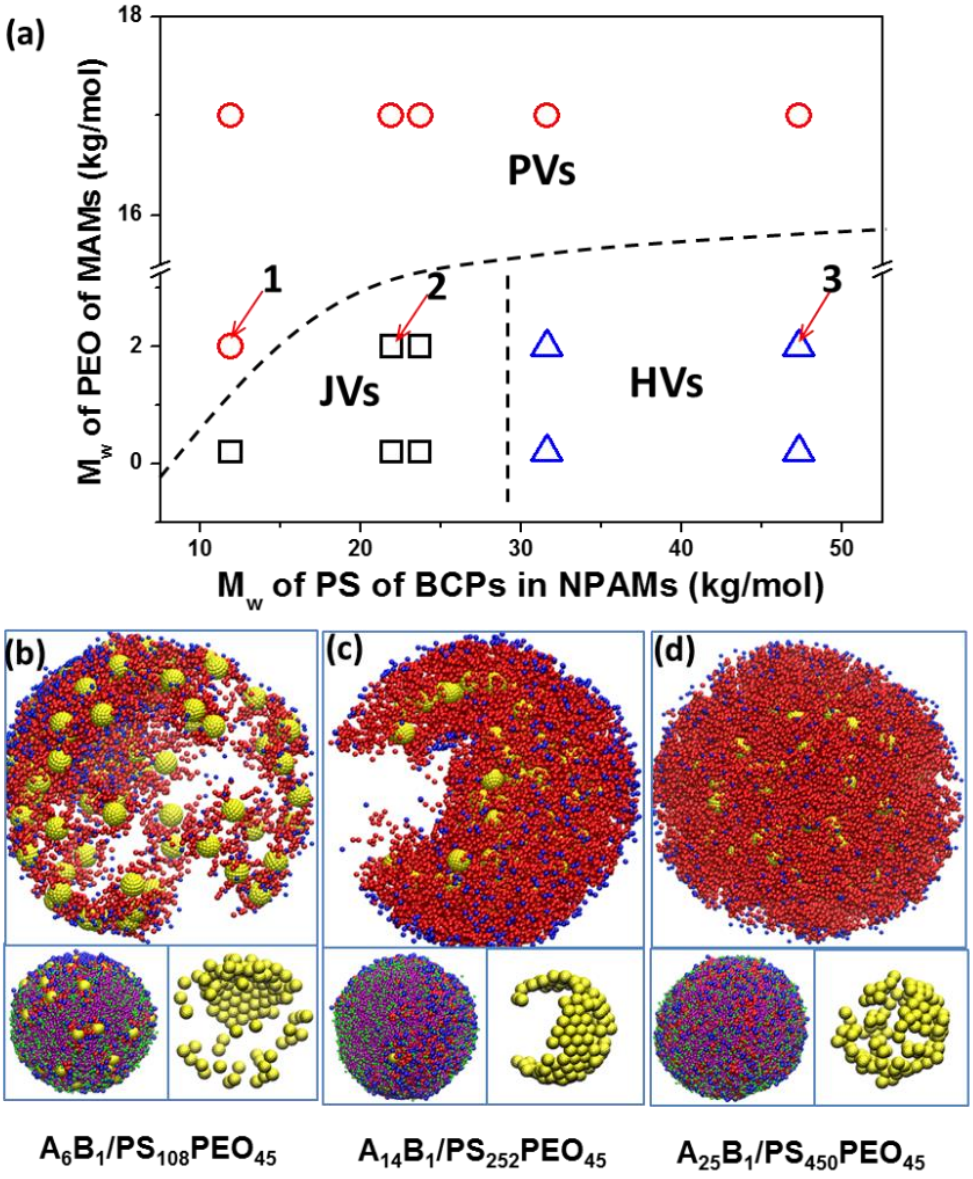

Figure 3.12. Phase separation behavior between the amphiphiles of MAMs and NPAMs. (a) Phase-like diagram of experimental study of the assembly of the two types of amphiphiles in a water/THF mixture (1:3 in volume ratio). In all conditions, the diameters of AuNPs in NPAMs were ca. 19 nm. The PEO blocks of BCPs in NPAMs were 2 kDa, while the PS blocks of MAMs were 32 kDa. The binary mixtures for the point 1, 2 and 3 in the phase-like diagram are Au-19-PS_{114}-*b*-

PEO_{45}/PS_{307}-*b*-PEO_{45}, Au-19-PS_{211}-*b*-PEO_{45}/PS_{307}-*b*-PEO_{45}, and Au-19-PS_{455}-*b*-PEO_{45}/PS_{307}-*b*-PEO_{45}.(b-d) Snap-shots of DPD simulation of co-assembly systems corresponding to point 1-3 in (a). For visualization purpose, MAMs are not shown in the top images in (b-d), and only AuNPs are shown in the right bottom images in (b-d).

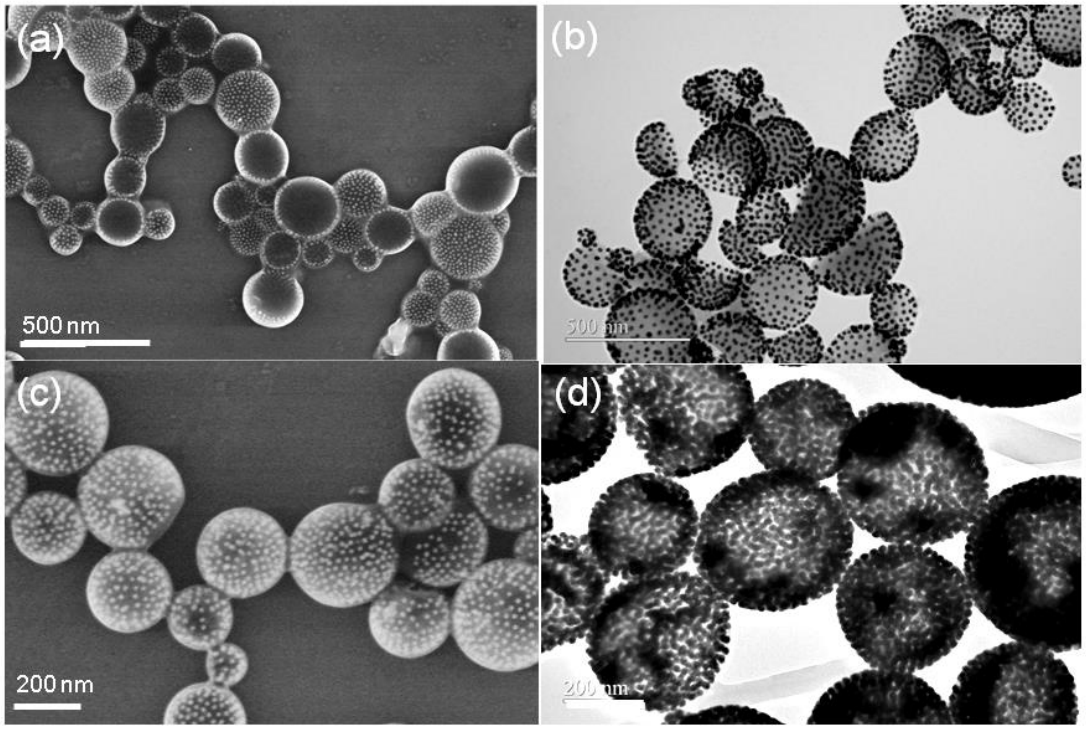

Figure 3.13. (a) TEM and (b) SEM images of the hemispherical shapes hybrid JVs assembled from Au-19-PS_{245}-*b*-PEO_{45}/PS_{307}-*b*-PEO_{5}. (c) TEM and (d) SEM images of HVs assembled from Au-19-PS_{455}-*b*-PEO_{5}/PS_{307}-*b*-PEO_{5}. When the PS length of tethered BCPs of NPAMs was relatively short, a strong phase-separation between two types of amphiphiles occurred to generate hybrid JVs with two distinguished halves. When the PS of tethered BCPs was long, NPAMs were uniformly distributed in the polymeric membrane to form hybrid HVs with a uniform distribution of AuNPs in the

membranes.

Our simulation results showed more details on the vesicle structures and the driving force of phase separation. We radially sliced the space with constant distance starting from the center of mass of the vesicle, and defined radial density distributions (RDDs) of one component as the number of the specific component divided by the volume of the spherical shell. Figure 3.14 a-c show the RDDs of each component of assemblies with different morphologies. The appearance of two distinguished peaks for hydrophilic PEO (or hydrophobic PS) in all the systems indicated that AuNPs were sandwiched between two hydrophilic PEO (or hydrophobic PS) layers which form the internal and external surfaces of the vesicle. We calculated the effective membrane thickness (D_{emt}) of each type of amphiphiles in the vesicle by using the distance between the two peaks of PEO blocks (Table 3.4). For both phase separated systems (hybrid PVs and JVs), D_{emt} of NPAMs was significantly different from that of MAMs, that is, 22.4 and 35.6 nm for patchy system, and 26.2 and 20.9 nm for Janus system, while D_{emt} of NPAMs and MAMs in HVs was approximately equal (Figure 3.14 a-c and Table 3.4). This indicates that the mismatch in D_{emt} of two types of amphiphiles exists in the vesicular membranes with surface patterns, which can be explained by the unique role of entropy during assembly. If the vesicle membrane comprises randomly distributed NPAMs and MAMs, MAMs will be stretched in the direction normal to the membrane, due to the compression from neighboring NPAMs (Figure 3.14 d). The stretching constraint on chain conformations of MAMs will be reduced by grouping MAMs together to form a large domain of their own, in which the MAM chains possess larger conformational entropy (Figure 3.14 e). Although

membrane thickness mismatch is energetically unfavorable to form hybrid JVs, the accompanied chain conformational entropy increases largely in MAM domain, which decreases overall free energy and favors the formation of hybrid JVs.

Table 3.4. Effective membrane thickness (D_{emt}) of MAM domains and NPAM domains.

Model in simulations	A_6B_1	$A_{14}B_1$	$A_{25}B_1$
Chain length	$PS_{108}PEO_{45}$	$PS_{252}PEO_{45}$	$PS_{450}PEO_{45}$
D_{emt} of NPAMs (nm)	22.4±0.6	36.2±0.6	40.4±1.1
D_{emt} of free BCPs (nm)	35.6±0.3	30.9±0.6	40.4±1.1

Simulation of the dynamics of assembly process indicated that both the mobility of NPAMs and the entanglement of polymer chains influence the final morphology of assembled structures. When NPAMs carrying short BCPs (PS_{108}-*b*-PEO_{45}) was assembled with MAMs of PS_{307}-b-PEO_{45}, the NPAMs migrated rapidly within the membrane, resulting in the fluctuation of the domain boundaries in the membranes. Small NPAM domains continuously merged into larger domains, while these large domains could not maintain a stable packing state and slowly dissociated into small individuals. In this case, hybrid PVs were formed as shown in both our experiments and simulations. This observation is also reflected by the presence of two distinguished RDD peaks of AuNPs (Figure 3.14 a): AuNPs were frequently pulled towards the outer or inner leaflet of the vesicle, rather than being stabilized in the center of the vesicular membrane as in hybrid JVs.

Alternatively, hybrid PVs can be produced when the chain length of hydrophilic PEO block (of MAMs) is significantly increased, as shown in Figure 3.11 a. When

we increased the PEO length of MAMs one order of magnitude, the MAMs in membranes were largely stretched due to the tendency of solvation of PEO blocks in water. This resulted in larger D_{emt} of MAMs. In contrast, the D_{emt} due to the variation of PS block length in NPAMs did not change that much, since PS blocks can be considered as in melt phase. Thus the AuNPs (of NPAMs) were mainly distributed in the outer or inner leaflet of the vesicular membrane (rather than in the center of the membrane). As a result, the mobility of NPAMs significantly increases, thus favoring the formation of PVs. This explains the formation of PVs for large PEO block length in the MAMs, regardless of the length of the PS block in the NPAMs. This also explains the transition from HVs to PVs in Figure. 3.11 a.

When NPAMs carrying very long BCPs (PS_{450}-*b*-PEO_{45}) was used, the entanglement of long polymer chains significantly reduced the mobility of NPAMs. The highly localized motion of NPAMs led to the uniform distribution of NPAMs within a continuous phase of MAMs in the membranes of HVs. The homogeneous distribution of NPAMs in vesicle in turn induced the stretching of MAM chains, as indicated by the equal value (40.4 nm) of D_{emt} and the overlap of the RDD along radical direction for both amphiphiles (Figure 3.14 c). In this case, although the conformational entropy of MAMs was reduced, the increase in the translational entropy of AuNPs favored the homogeneous distribution of AuNPs in the vesicle. In addition, the stretching of MAMs enhanced the lateral packing (or interactions) of the grafted BCP chains and free BCP chains, and reduced the roughness of the inner and outer surface of vesicular membranes, thus giving rise to a lower overall interfacial free energy of the system. In a word, the mismatch of PS chain length, the

entanglement of polymer chains, and the mobility of NPAMs synergistically determine the three types of morphologies of vesicular assemblies. The hybrid JVs only formed when the lengths of free BCPs of MAMs and tethered BCPs in NPAMs were in a specific window, as shown in Figure 3.11 a. The need for maximizing conformational entropy of polymers induces effective attraction between NPAMs, thus leading to a well-equilibrated Janus structure under thermodynamic control. For the formation of PVs and HVs, other than dominant role of thermodynamics, the assembly is also affected by kinetic factors (i.e., entanglement of polymer chains).

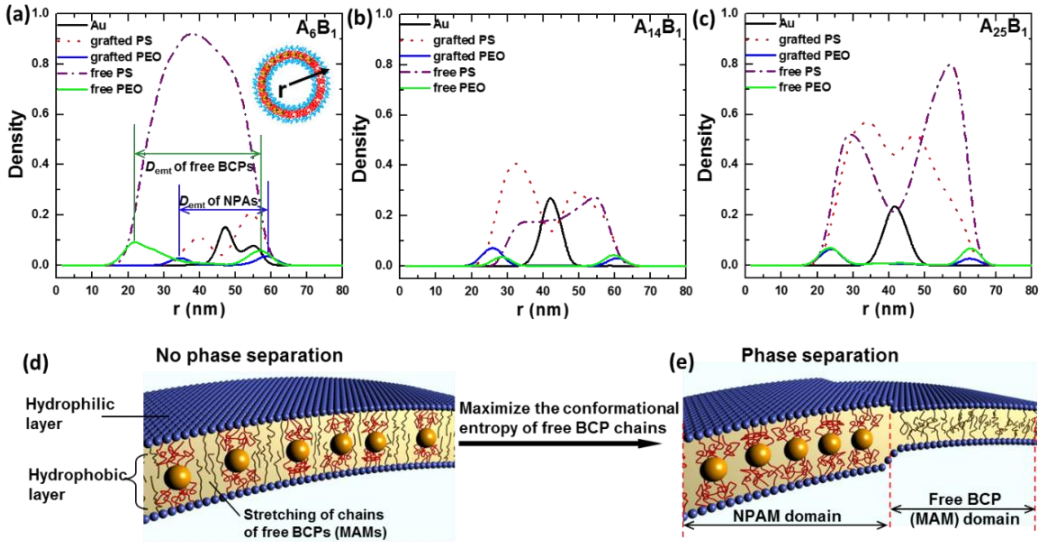

Figure 3.14. Membrane structures of the vesicles assembled from binary mixtures of amphiphiles of MAMs and NPAMs. (a-c) Radial density distributions (RDD) of each component of assembly of two types of amphiphiles corresponding to point 1-3 in the phase-like diagram in Figure 3.11: PVs (a), JVs (b), and HVs (c). The length of PS blocks of MAMs and PEO blocks of tethered BCPs are 32 kDa and 2 kDa, respectively. AuNPs with a diameter of 19 nm were used in all experiments. (d, e) Schematic illustration of the formation mechanism of hybrid JVs due to phase

separation. (d) In membrane without phase separation, the MAMs are stretched in the direction normal to the membrane due to the compression from neighboring NPAMs. (e) The effective attraction between NPAMs is induced by the need for maximizing conformational entropy of MAMs.

3.4 Conclusions

In summary, we demonstrated a simple yet powerful strategy for designing hybrid vesicles with well-defined shape, morphology and surface pattern through co-assembly of multiple types of amphiphiles. The dominant role of entropy in the co-assembly process conceptually differs our system from any existing concurrent assembly of solely organic amphiphiles. These hybrid vesicles have potential applications in sensing,[157] bioimaging,[158] drug delivery,[45] nano- and micro-reactors,[159] and optoelectronics.[160] The ability to construct discrete nanostructures from multiple types of amphiphiles with distinct size, shape and composition paves the way for the fabrication of structurally complex functional materials with broad applications. Moreover, this strategy will significantly enlarge the library of tunable parameters (i.e., dimension, shape, rigidity, bending modulus, etc.) available for controlling assembly, which is unattainable solely by organic amphiphiles.

Chapter 4: Concurrent Self-assembly of Polymeric/Inorganic Nanoparticle Hybrid Vesicles with Magneto-Plasmonic Properties

Overview. We reported the cooperative self-assembly of multiple types of building blocks including NPAMs containing AuNP cores, hydrophobic MNPs, and free MAMs of BCPs into multifunctional hybrid vesicles. The assembly process produced hybrid Janus vesicles with spherical shapes and hemispherical shapes, and spherical patchy vesicles. The morphologies of the assemblies and distribution of NPs within the hydrophobic membrane can be readily controlled by adjusting the sizes and amount of NP building blocks. The hybrid vesicles can be used as drug delivery vehicles and the controlled release of payloads can be achieved with the assistance of external laser light. The photothermal effect can be enhanced by magnetically triggered concentration of vesicles. This strategy offers us a new way to control the shapes and properties of the assemblies. We further demonstrated the resulting magneto-plasmonic hybrid vesicles showed more than two times of enhancement in transverse relaxation rate than that of MNPs-loaded micelles. Thus, the hybrid vesicles have potential applications in drug delivery and treatment.

This chapter is adapted from a manuscript that is to be submitted to *ACS Nano*.

4.1 Introduction

Magnetic, plamonic, and fluorescent properties of inorganic NPs have been widely used in biomedical applications.[35,40,59] Inorganic NP/polymeric hybrid vesicles with imaging and therapeutic functionalities, such as PA imaging, MRI, and

photothermal therapy, have been reported.[27,76,161,162] The desired functionalities of the assemblies are largely determined by the types of inorganic NPs presented in the discrete structures. The integration of multiple types of inorganic NPs into the structures is expected to bestow the system with multiple functionalities, hence broadening their potential applications. For example, the hybrid nanomaterials with both MNPs and AuNPs show magneto-plasmonic properties, leading to their applications as imaging probes (PA imaging and MRI) and therapeutic agents (photothermal therapy) simultaneously.[163,164] In Chapter 3, we demonstrated that the concurrent self-assembly of NPAMs and MAMs have led to hybrid vesicles with controllable patterns of NPAMs and BCPs within the vesicular membranes.[99,153,165,166] The free BCPs domains in hybrid vesicles can encapsulate hydrophobic inorganic NPs, making it possible to build multi-component hybrid vesicles. Despite the attempts to insert various types of inorganic NPs into polymeric membranes, our ability to assemble multiple types of inorganic NPs into one system is still limited. Up to now, there is no report on the preparation of magneto-plasmonic vesicles. We are interested in inserting inorganic NPs into vesicular membranes and understanding the fundamentals of self-assembly, in order to achieve delicate control over assembly structures.

This chapter describes a systematic study on the concurrent self-assembly of multiple types of building blocks including hydrophobic NPs, NPAMs, and free amphiphilic linear BCPs into multicomponent hybrid vesicles. As a proof-of-concept experiment, we will generate the magneto-plasmonic hybrid vesicles by co-

assembling a mixture of AuNPs tethered with PS-*b*-PEO (NPAMs), free BCPs of PS-*b*-PAA (MAMs), and hydrophobic magnetic NPs (MNPs) (Figure 4.1). By tuning the sizes of NPAM cores and amount of MNPs, we produced vesicles with various shapes, including Janus spherical vesicles (JSVs), Janus hemispherical vesicles (JHVs), and spherical patchy vesicles (PVs). The hybrid vesicles show tunable LSPR in the range of 550 nm to 650 nm as a result of the controlled plasmonic coupling and are responsive to external magetic field. The addition of MNPs led to two morphological transitions of the hybrid vesicles, which are: i) from spherical shapes to hemispherical shapes, and ii) from homogeneous shapes to Janus shapes. The photothermal effect of the hybrid vesicles could be enhanced through the magnetic field induced concentration of vesicles to a specific location. Finally, we demonstrated that the transverse relaxation rate (R_2) of the vesicles were strongly dependent on morphologies of assemblies.

4.2 Experiment

4.2.1 Materials

THF, gold(III) chloride trihydrate ($HAuCl_4$, ≥99.9% trace metals basis), sodium citrate tribasic dihydrate (≥99%), sodium oleate (NaOL), silver nitrate ($AgNO_3$), iron(III) chloride hexahydrate ($FeCl_3$▪$6H_2O$), hexane, oleic acid, and octadecene were purchased from Sigma-Aldrich. Free BCPs of PS_{107}-*b*-PAA_4 were purchased from polymer source. The polymer ligands of PS_{490}-*b*-PEO_{45} were prepared by the reversible addition–fragmentation chain transfer polymerization.

4.2.2 Synthesis of inorganic NPs

The Fe_3O_4 NPs (MNPs) were prepared according to the previous reference.[107] Iron-oleate, the precursor for the MNP synthesis, was synthesized through the following method. A 5.4 g mass of $FeCl_3 \cdot 6H_2O$ and 18.25 g mass of NaOL were dissolved in a solvent mixture containing 40 mL ethanol, 70 mL hexane, and 30 mL distilled water. The solution was stirred at 70 ℃ for 4 hours before the organic layer was extracted. The organic solution was washed with water for 3 times. Then the organic solvent was removed through rotary evaporator and vacuum oven. For the synthesis of MNPs, a 9g mass of iron-oleate, 1.4 g mass of oleic acid, and 40 mL of octadecene were mixed in a 3-neck flask followed by pumping with Ar for 30 min. The reaction temperature was elevated to 310 ℃ and was maintained for 30 min. After the purification, MNPs were dissolved in THF for self-assembly.

The AuNPs were synthesized by sodium citrate reduction method.[81] The AuNPs seeds were prepared by injecting 1 mL of 10 mg/mL $HAuCl_4$ aqueous solution and 3 mL of 10 mg/mL sodium citrate into 500 mL of boiling water under stirring. After being refluxed for 30 min, the solution temperature was decreased to 85 ℃. Another 3 mL of sodium citrate solution and 1 mL of HAuCl4 solution were injected. Repeat this step for certain times until the desired AuNP size was achieved.

4.2.3 Preparation of NPAM

The preparation NPAMs is referred to the experimental section in Chapter 3.

4.2.4 Self-assembly procedure

For the self-assembly of JSVs, a 250 μL THF solution of NPAMs (2 mg/mL), a 75 μL THF solution of BCPs (0.8 mg/mL), and a 15 μL THF solution of MNPs (10 mg/mL) were mixed together. The volume of the solution was adjusted to 400 μL by adding THF. A THF/water solvent mixture (v/v=3:2) was injected into the above solution by a syringe pump at rate of 2 mL/h until the final water content reached 25%. The solution was held for 3 hours before being dialyzed against pure water to remove the organic solvent.

To prepare the MNPs loaded polymer micelles, a 75 μL THF solution of BCPs and a 15 μL of MNPs solution were mixed together and the final volume was adjusted to 400 μL by adding THF. A THF/water solvent mixture (v/v=3:2) were injected into the above solution by a syringe pump at rate of 2 mL/h until the final water content reached 25%. The solution was held for 3 hours before being dialyzed against pure water to remove the organic solvent.

4.3 Results and discussion

The hydrophobic Fe_3O_4 MNPs used in this work were covered with oleic acid as ligands on the surfaces. The NPAMs were made by attaching thiol terminated PS_{490}-*b*-PEO_{45} onto the surfaces of AuNPs with different sizes (20 nm, 30 nm, and 50 nm). BCPs of PS_{107}-*b*-PAA_4 without thiol groups were used as MAMs. The self-assembly of ternary mixture was triggered by the solvent exchange method.[10] Briefly, the three types of building blocks were first mixed in THF, which is a good solvent

for all. A water/THF mixture with a water fraction of 40% (% by volume) was slowly added into the above solution at a constant rate of 2 mL/h until the water content reached 25% in the solution. The resulting solution was held for 3 h before being dialyzing against ultrapure water to completely remove THF in the solution.

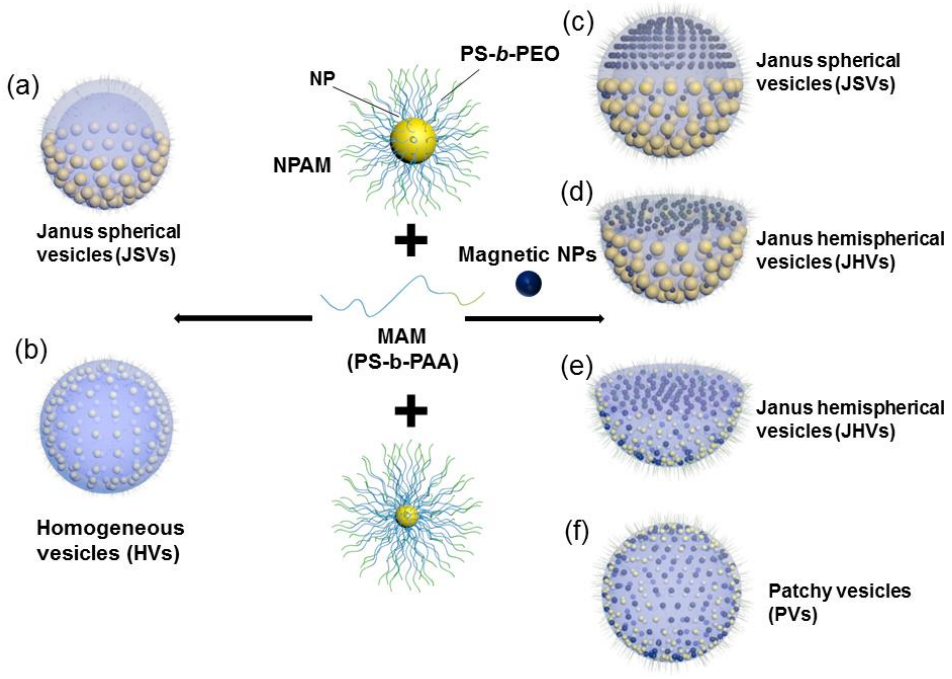

Figure 4.1. Schematic illustration of ternary assembly of NPAMs, free BCPs, and MNPs into hybrid vesicles. The yellow and blue spheres represent AuNPs and MNPs, respectively. The concurrent assembly of MAMs and NPAMs with large AuNP cores (50 nm and 30 nm) resulted in (a) JSVs. The hybrid vesicles made from the concurrent assembly of NPAMs with large cores, MAMs, and hydrophobic MNPs were (c) JSVs and (d) JHVs depending on the amount of MNPs. The concurrent assembly of MAMs and NPAMs with small AuNP cores (20 nm) resulted in (b) HVs.

In the presence of MNPs, the concurrent self-assembly led to a formation of (e) JHVs with a concentration ranging from 5.8% to 11.0 wt. % of MNPs and (f) PVs at 15.6 wt. % of MNPs.

4.3.1 Magneto-plasmonic hybrid vesicles

Depending on the size of NPAMs and mass concentration of MNPs in the mixture of the three building blocks, the assembly process produced Janus vesicles with spherical shapes (JSVs) and hemispherical shapes (JHVs), in which NPAMs segrated to the one half vesicluar membranes, and patchy vesciels (PVs), in which many domains of MNPs were sorrounded by NPAMs.

First, when NPAMs with relatively large cores (30 nm or 50 nm) were used, the concurrent assembly of NPAMs and MAMs in absence of MNPs formed JSVs, with distinguished polymer-rich domains and NPAM-rich domains (Figure 4.2 e). With the presence of MNPs, the ternary assembly morphologies remained as JSVs with a concentration of MNPs below wt. 5.8%. The increase of concentration of MNPs to wt. 11.0% led to a formation of JHVs. The JSVs composed of NPAMs with relatively large cores were achieved by using MNPs ranging from 15 nm to 30 nm (Figure 4.2 a-d). The hybrid vesicle constitutes a hollow cavity and a membrane composed of NPAMs, MNPs, and free BCPs. The higher contrast at the edges and the wrinkle surfaces of the assemblies in TEM images are typical characters of vesicular assemblies (Figure 4.2 b and d).[167] The average diameter of the JSVs containing 15 nm MNPs is 570.8 ± 93.2 nm characterized from DLS (Figure 4.S1). The value is

close to the average diameter of 538.5 ± 106.1 nm obtained from SEM analysis. Within the vesicular membranes of JSVs, the NPAMs were segregated from free BCPs, and relatively densely packed in one half of the vesicles, while the hydrophobic MNPs could be clearly observed in the polymeric domains in the other half of the vesicles. A close inspection revealed that there were some MNPs between NPAMs.

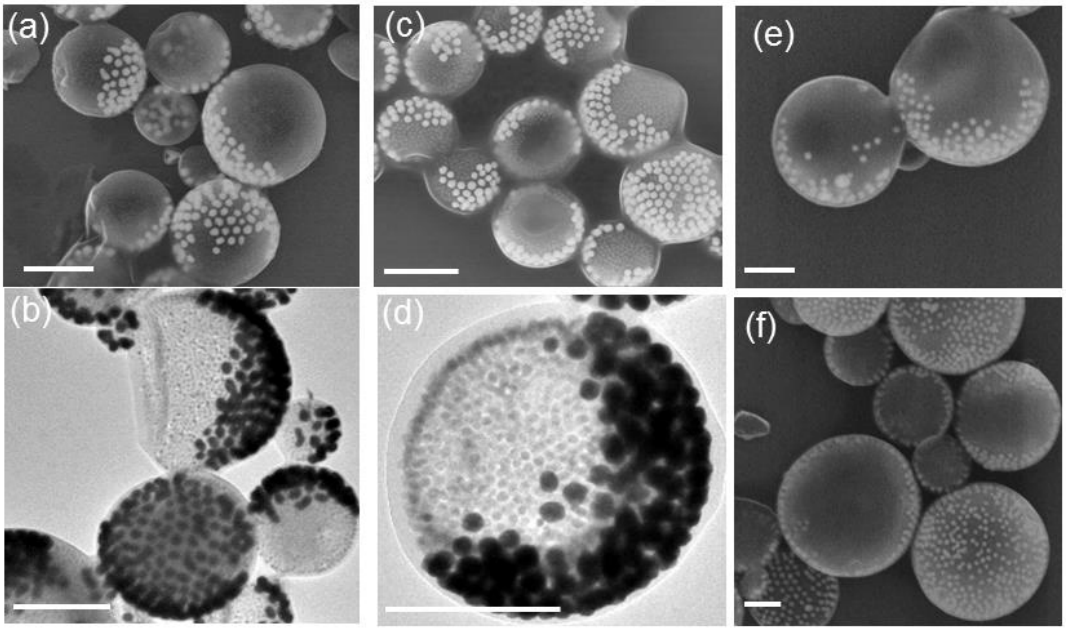

Figure 4.2. SEM and TEM characterizations of magneto-plasmonic hybrid vesicles composed of relatively large NPAMs. (a) SEM and (b) TEM images of the JSVs, where AuNPs and MNPs are 50 nm and 15 nm, respectively. (c) SEM and (d) TEM images of the JSVs, where AuNPs and MNPs are 50 nm and 30 nm, respectively. The BCP building blocks are PS_{107}-*b*-PAA_4. SEM images of the (e) JSVs made from concurrent assembly from NPAMs with 30 nm cores and PS_{107}-*b*-PAA_4 and (f) JHVs made from NPAMs with 30 nm cores, 15 nm MNPs, and PS_{107}-*b*-PAA_4. Scale bars:

500 nm in (a), (b), (c), 400 nm in (d), and 200 nm in (e) and (f).

Second, when NPAMs with relative small cores (20 nm) were used, the ternary concurrent self-assembly produced JHVs at a concentration of MNPs between wt. 5.8% and wt. 11.0% and PVs at a wt. 15.6 % of MNPs. Each JHV has a bowl-like vesicular body containing a mixture of NPAMs and MNPs, covered by a flat polymeric membrane containing MNPs only (Figure 4.3 b and e). The JHVs composed of NPAMs with 20 nm cores have an average diameter of 395.0 ± 124.8 nm measured from SEM. In PVs, many small BCPs/MNPs rich domains were surrounded by NPAM-rich domains (Figure 4.3 c and Figure 4.3 e). The average diameter of PVs is 504.8 ± 120.9 nm obtained from SEM. In the absence of MNPs, the concurrent self-assembly of NPAMs and MAMs led to a formation of homogeneous spherical vesicles (HSVs) (Figure 4.3 a).

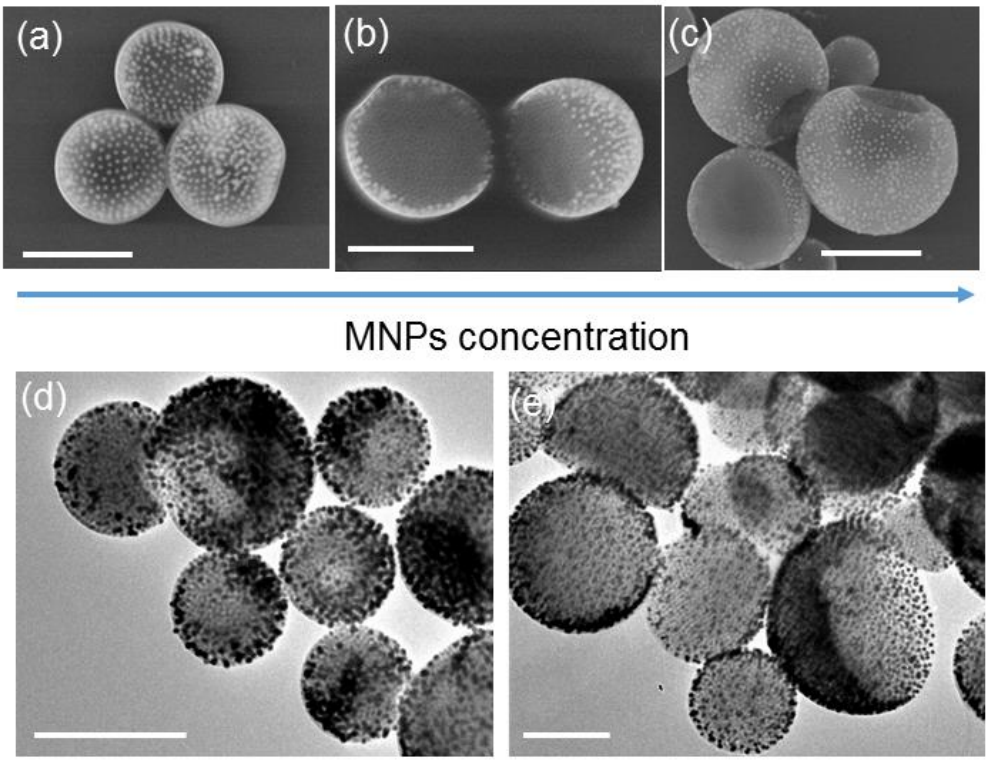

Figure 4.3. SEM and TEM characterizations of magneto-plasmonic hybrid vesicles composed of relatively small NPAMs. (a) SEM image of HSVs made from NPAMs composed of 20 nm cores and free BCPs of PS_{107}-*b*-PAA_4 in absence of MNPs. (b) SEM image of the JHVs made from the ternary assembly with wt. 5.8% of MNPs. (c) SEM image of the PVs made from the ternary assembly with wt. 15.6% of MNPs added. The corresponding TEM images are (d) PVs and (e) JHVs. Scale bars: 500 nm

The energy dispersive X-ray spectrometry (EDX) was used to characterize the distribution of two types of NPs within the JSVs (Figure 4.4 a). The higher intensities of Fe and Au signal at the edge of the vesicles in the EDS line scan confirmed the formation of vesicles with hollow cavity. The signal of Au only located at one end of the line, indicating the phase separated vesicular structures. The Fe intensities were

slightly higher at the polymer end than the AuNP end. This can be explained by the non-uniform distribution of MNPs in the membrane, when the concentration of MNPs is lower at NPAM halves.

The absorptions of JSVs, JHVs, and PVs were measured by UV-VIS spectroscopy. For JSVs containing 50 nm AuNPs, a strong red-shift of the LSPR peak from 543 nm of individual NPs to 650 nm of the hybrid vesicles was observed (Figure 4.4 b). For JHVs and PVs composed of 20 nm AuNPs, the LSPR peaks red-shifted from 530 nm of individual AuNPs to 560 nm and 570 nm, respectively. (Figure 4.4 c). The red-shift of the plasmon peak is proportional to the $e^{(-d/D)}$, where d and D are interparticle distance and NP diameter, respectively.[76] The segregation of NPAMs in one half of the vesicles in JSVs reduced the interparticle distance between AuNPs, The average interparticle distances between pairs of AuNPs in JSVs, JHVs, and PVs were measured to be 10.6 nm, 11.0 nm, and 11.9 nm, respectively. Therefore, the larger red shift of LSPR peak of JSVs was due to the larger AuNP diameter and smaller interparticle distance in the JSVs than other systems

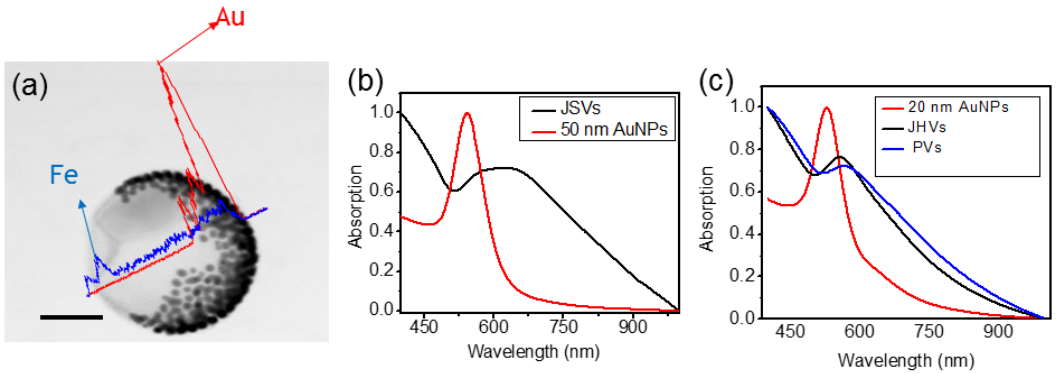

Figure 4.4. The EDX and Uv-vis characterizations of hybrid vesicles. (a) EDX line

scan of the Fe and Au intensities of the JSVs. The red and blue lines represent the signals of Au and Fe, respectively. (b) The UV-vis absorption spectra of NPAMs with 50 nm cores (red) and JSVs composed of NPAMs with 50 nm cores (black). (c) The UV-vis absorption spectra of NPAMs with 20 nm cores (red), PVs (blue), and JHVs (black) composed of NPAMs with 20 nm cores. Scale bars: 500 nm.

4.3.2 Cooperative assembly behaviors of MNPs

The assembly morphologies were largely dependent on the size and mass concentration of NP building blocks. To understand the self-assembly mechanism, we compared the morphologies of binary assemblies of NPAMs and BCPs to ternary assembly morphologies comprising NPAMs, BCPs and MNPs. The results were summarized in a phase-like diagram in Figure 4.5. In the study of the phase-like diagram, the size of MNP was kept as 15 nm and the three types of NPAMs with different core size (20 nm, 30 nm and 50 nm) were used. The addition of MNPs led to two structural changes of hybrid vesicles: i) a transition from spherical shapes to hemispherical shapes, and ii) a transition from homogeneous vesicles to Janus vesicles.

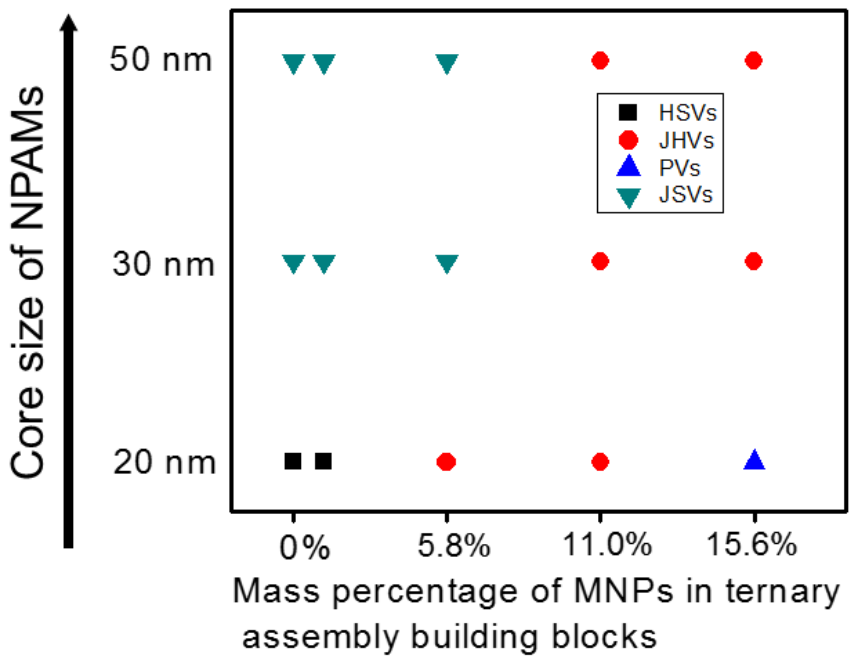

Figure 4.5. Phase-like diagram of concurrent self-assembly of magneto-plasmonic hybrid veiscles. The phase like diagram showed the assembly structures were affected by the core sizes of NPAMs and m% of MNPs introduced. HSVs, JHVs, PVs, and JSVs represent homogeneous spherical vesicles, Janus hemispherical vesicles, spherical patchy vesicles, and Janus spherical vesicles, respectively

First, when the wt. % of MNPs was increased to certain amount (*i.e.* 11.0 wt. % for relatively large NPAMs and 5.8 wt. % for small NPAMs), a structural transition from spherical shapes to hemispherical shapes occurred. Our control experiment showed that MNPs were excluded from NPAMs without addition of free BCPs (Figure 4.6 a). Also, MNPs were not observed in the hybrid vesicles if free BCP of PS-*b*-PEO was used to replace PS-*b*-PAA (Figure 4.6 b). Therefore, MNPs can only locate at the area where PS-*b*-PAA is present, possibly due to the coordination

interactions between MNPs and PAA.[168] We presume that the structural transition is a result of the phase separation between NPAMs and MAMs and the increase in the packing parameters of BCPs due to the presence of MNPs. The mismatch between the membrane thicknesses of NPAMs and MAMs is the driving force for phase separation.[99] The insertion of MNPs into the hydrophobic membrane effectively increase the hydrophobic volume of BCPs, resulting in the increase of the packing parameter.[18]

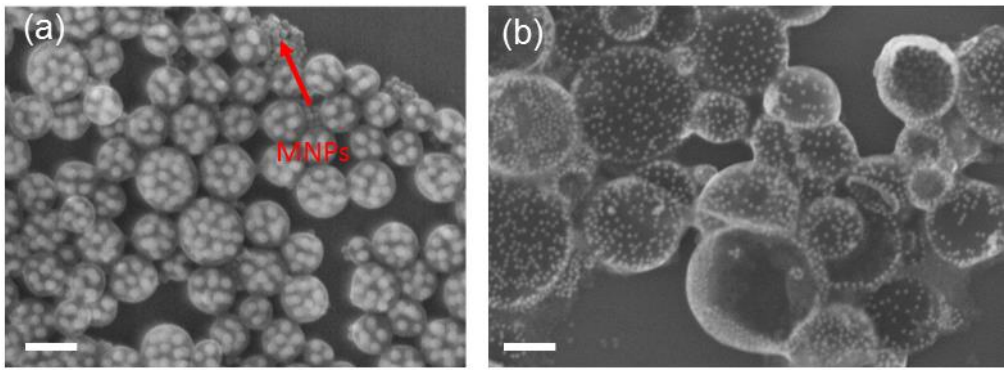

Figure 4.6. Control experiments of the concurrent self-assembly of hybrid vesicles. (a) SEM image of the concurrent self-assembly of NPAMs with 20 nm cores and 15 nm MNPs. The red arrow indicated the clusters of MNPs outside the NPAM assemblies. (b) The concurrent self-assembly of NPAMs with 20 nm cores, free BCPs of PS-*b*-PEO, and 15 nm MNPs. Scale bars: 100 nm in (a) and 200 nm in (b).

Second, when NPAMs with 20 nm cores were used as NP building blocks, the increase of wt. % of MNPs led to a structural transition from homogeneous vesicles to Janus vesicles. In the absence of MNPs, the mixture self-assembled into HSVs. We presume that the formation of HSVs in the absence of MNPs was due to kinetic

factors (*e.g*. entanglement of polymer chains). The driving force for phase separation is weaker as the smaller mismatch between the membranes thicknesses of two types of amphiphiles led to smaller conformational entropy gain through phase separation. With the presence of MNPs, the assembly morphologies changed from homogeneous vesicles to Janus vesicles. Our hypothesis is that the hydrophobic interactions between PS-*b*-PAA and MNPs leads to the PS-b-PAA wrapped MNPs during the self-assembly process. This increases the membrane thickness of the combination of PS-*b*-PAA and MNPs. It is also possible that when free BCPs wrap onto the surfaces of hydrophobic MNPs, it increases the effective molecular weight of free BCPs and costs higher entropy penalty for BCPs wrapped MNP to be inserted into polymer ligands on the surfaces of NPAMs.

In addition, PVs were formed when a high wt. % of MNPs were co-assembled with NPAMs with 20 nm cores and MAMs. We presume that the PV is an intermediate assembly morphology between HSV and JHV and was formed possibly due to the kinetic factors (mobility of NPs, entanglement of polymer chains).

4.3.3 Photothermal effect and drug release

The localized heat generated by AuNPs upon laser irradiation has been used in photothermal ablation of tumor cells or externally-triggered release of payloads.[55] The JSVs made from 50 nm AuNPs and 15 nm MNPs have a plasmon peak of 670 nm. Upon the irradiation of 655 nm CW laser (0.35 W/cm^2), the temperature of the samples rose from 24 ℃ to 38 ℃ in 4.5 min as a result of localized heat. In contrast,

neither pure water nor MNPs micelles led to obvious rise in the temperature, the photothermal effect of pure MNP system was negligible (Figure 4.7).

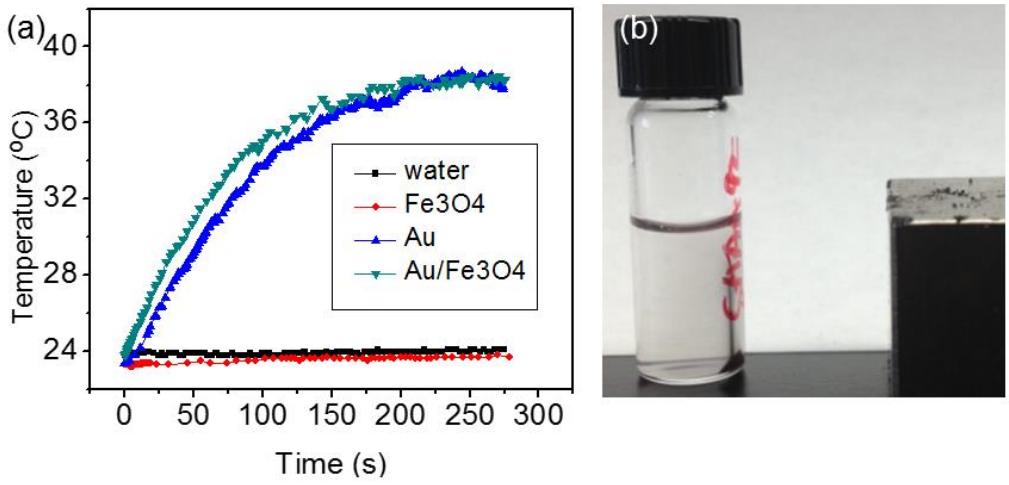

Figure 4.7. Photothermal property and magnetic responsiveness of the hybrid vesicles (a) The photothermal induced temperature increase of the MNPs/Au hybrid vesicles (green), Au vesicles (blue), MNPs assemblies (red), and water (black). (b) The responsiveness of hybrid vesicles to external magnetic fields.

It has been reported that the external magnetic fields can be used to manipulate the biodistribution of MNPs, thus promoting the accumulation of MNPs in the tumor area.[169,170] The presence of MNPs in the hybrid vesicles makes them responsive to external magnetic field. With a magnet nearby, hybrid vehicles were immediately concentrated on the inner surfaces of the container to the direction of the magnetic field. The solution turned clear in 5 min, indicating most of the hybrid vesicles in the solution were concentrated. The concentration process was reversible, as the concentrated vesicles were dispersed again in the solution with gently shaking after

the magnet was taken away. No insoluble aggregate was observed after the hybrid vesicles were concentrated and dispersed in the solution for 10 times. The manipulation of magnetic field can directionally move the materials to a targeted place and the photothermal effect of the hybrid materials at a specific location can be enhanced by concentrating the hybrid vesicles under external magnetic field. To demonstrate that the concentration of vesicles can enhance the photothermal effect, we compared the localized temperature change when a NIR laser was irradiated at a solution in which hybrid vesicles that were uniformly dispersed versus those the vesicles were concentrated. We loaded our vesicle solution into a capillary tube and the irradiation of 655 nm CW laser toward the hybrid vesicles solution increased the localized temperature from 24 ℃ to 40 ℃. Then a magnet was put below the capillary tube for 5 min to concentrate the hybrid vesicles to the bottom. The same laser was used to irradiate the concentrates of hybrid vesicles for same amount of time, and the temperature of the localized area increased from 24 ℃ to 70 ℃. The temperature increase was due to the more rapid heating at higher localized concentration of Au materials and the relatively slow heat dissipation to surrounding water. The results indicated the hybrid vesicles can potentially enhance their efficiency in photothermal therapy by external magnetic field triggered concentration of vesicles.

To demonstrate the potential use of hybrid vesicles in remote-controlled release of payloads, we encapsulated a model drug, fluorescein isothiocyanate (FITC) in the hybrid vesicles during the assembly process. The resulting FITC loaded vesicles were put into a dialysis tube and irradiated with 655 nm CW laser at a time interval of 3

min. The dialysis tube was placed in a 3 mL water reservoir and 1 mL of water from reservoir was taken and measured of its fluorescence intensity every three min. After each measurement, the 1 mL water was put back into the water reservoir. Figure 4.8 b and c show that the fluorescence intensity at 520 nm increased as a function of time. The localized heat melted the AuNPs and broke the integrity of the vesicles, leading to the release of cargos (Figure 4.9). The FITC release rate from hybrid vesicles can be tuned by external magnetic field. The faster release of FITC were achieved by first concentrating hybrid vesicles through an external magnetic field and then irradiating the vesicles concentrates with the laser. The fluorescence intensity plateau was reached more quickly when external magnetic field was used to concentrate the hybrid vesicles (18 min) than that of hybrid vesicles which were uniformly dispersed in the solution (45 min) (Figure 4.8 c).

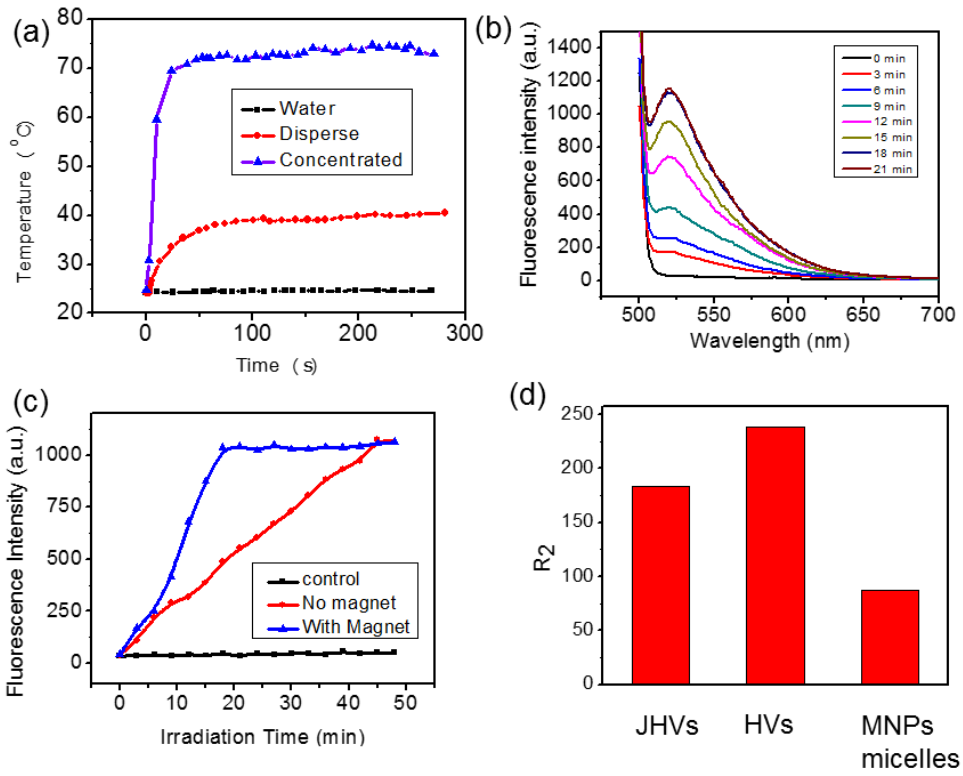

Figure 4.8. Photothermal properties, drug release profiles, and transverse relaxation rate of hybrid vesicles. (a) The photothermal effect induced temperature increase of the water (black), hybrid vesicles that were uniformly dispersed (red), and concentrated hybrid vesicles (blue). All the samples were irradiated with a 655 nm CW laser (0.35 W/cm^2) for 4.5 min. (b) The time-dependent florescence spectra of the dye released from the hybrid vesicles with the laser irradiation. Fluorescence intensity at 520 nm gradually increased with laser irradiation time. (c) The FITC release profile from the hybrid vesicles that were uniformly dispersed (blue), concentrated hybrid vesicles (red) under laser irradiation, and from hybrid vesicles without laser irradiation (black). (d) The R_2 of JHVs, HVs, and MNPs-loaded

micelles were calculated to be 183.8, 238.6, and 87.5 s^{-1} mM^{-1}.

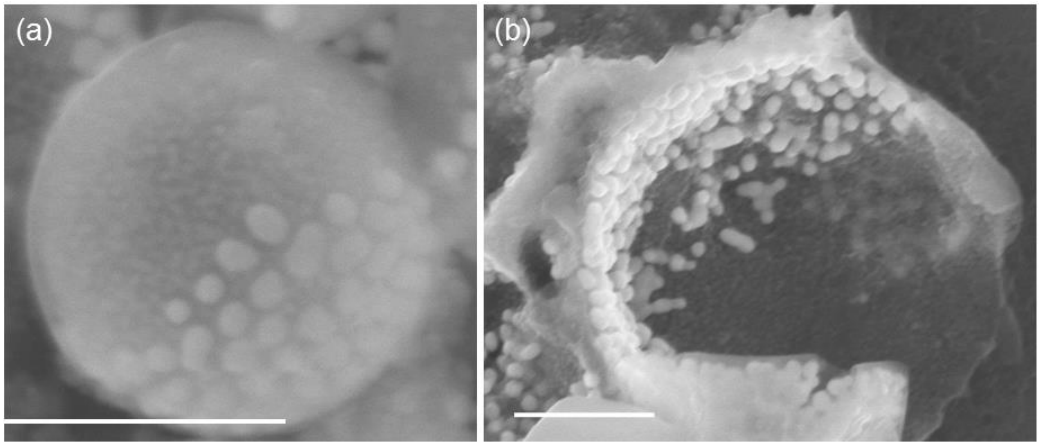

Figure 4.9. SEM images of JSVs (a) before and (b) after being irradiated by for 4 min 655 nm CW laser (0.35 W/cm2) for 4 min. Scale bars: 500 nm

4.3.4 MRI phantom and R_2

Magnetic NPs have been widely used in biomedical applications, such as MRI and magnetic hypothermia therapy.[57-60] To evaluate the potential application of hybrid vesicles in MRI, we measured the transverse relaxation rates (R_2) of JSVs, JHVs, and MNP-loaded polymer micelles to study how assembly structures would affect MRI sensitivity. The MNP-loaded polymer micelles were prepared by concurrent self-assembly of MNPs and free BCPs without using NPAMs. (Figure 4.10). In the presence of NPAMs, the hybrid vesicles formed.

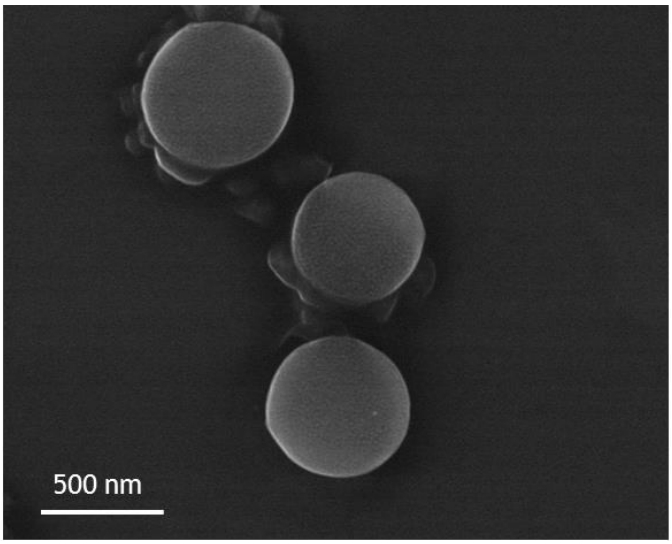

Figure 4.10. SEM image of the MNPs-loaded polymeric micelles made from 15 nm MNPs and free BCPs of PS_{107}-b-PAA_4.

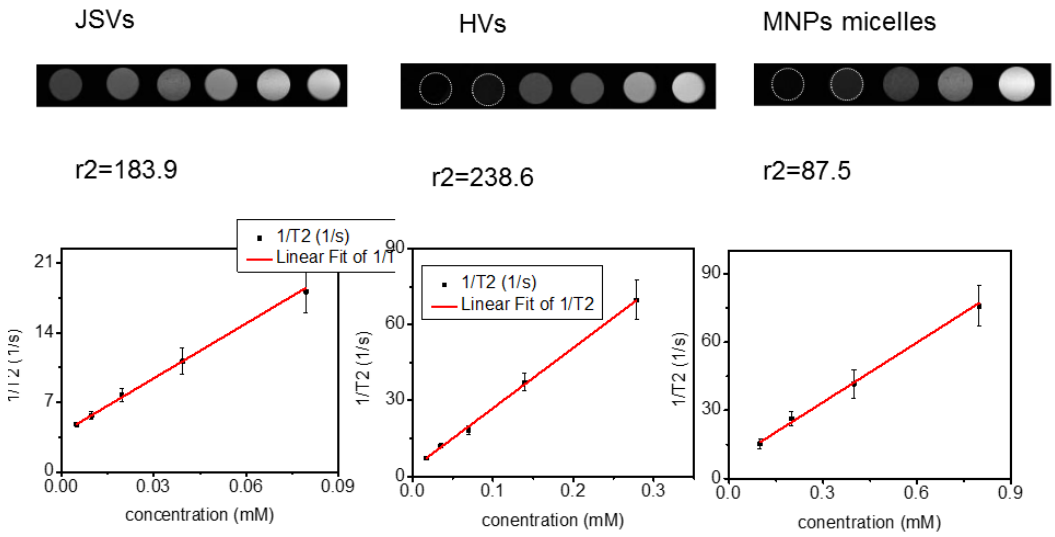

Figure 4.11. MRI phantom images of JSVs, HVs, and MNPs micelles with an iron concentration gradient and the corresponding R_2 values.

R_2 is the transverse relaxation rate of water protons based on the molar concentration of iron. The higher R_2 rate indicates a more sensitive MRI contrast agent. To obtain the R_2 of different materials, the inverse transverse relaxation time (T_2) was plotted as a function of concentration of iron in the hybrid materials. The R_2 of JSVs, JHVs, and hybrid micelles were calculated to be 183.8, 238.6, and 87.5 s^{-1} mM^{-1}, respectively (Figure 4.8 d and Figure 4.11). It was found that the R_2 of hybrid vesicles was more than two times higher than the R_2 of MNP-loaded polymer micelles, because of the higher water accessibility to the MNPs in hybrid vesicles. This observation is in agreement with previous reported results.[60]

4.4 Conclusions

We developed the self-assembly of hybrid vesicles with membranes integrated with multiple types of inorganic NPs as potential therapeutic materials. The distribution of NPs within the membrane and assembly morphologies can be controlled by changing the size and concentration of NP building blocks. We further evaluated the performance of hybrid vesicles in MRI and the photothermal experiment. The photothermal effect of the materials can be enhanced by magnetically manipulating and concentration of hybrid vesicles to specific locations. We also demonstrated that the hybrid vesicles can be potentially used in drug delivery and the release of cargoes can be controlled remotely by light. The hybrid vesicles showed higher R_2 than MNPs hybrid micelles, as a result of larger water molecule accessibility to MNPs.

Chapter 5: Continuous Microfluidic Self-assembly of Hybrid Janus-like Vesicular Motors: Autonomous Propulsion and Controlled Release

Overview: Vesicular micro-/nanomotors are attractive micro/nanomachines for their ability to encapsulate active compounds (e.g., drugs) and deliver the payload in a controlled manner. We reported the single-step, template-free self-assembly of polymer/inorganic NP hybrid, Janus-like vesicular (JVs) motors using microfluidic flow-focusing device (μFFD). The vesicles can be used to encapsulate active compounds, and the release of this payload can be effected using NIR light.

This chapter is adapter from manuscript published in the following article: Wang, L. Liu, Y. [&], ([&] co-first author) He, J., Hourwitz, M. J., Yang, Y., Fourkas, J. T., Han, X. and Nie, Z., Continuous Microfluidic Self-Assembly of Hybrid Janus-Like Vesicular Motors: Autonomous Propulsion and Controlled Release. *Small.* **2015**, doi: 10.1002/smll.201500527.

Note: Yijing Liu performed the synthesis of BCPs and NPs and preparation of NPAMs. Dr. Lei Wang and Yijing Liu performed the self-assembly experiments in microfluidic devices. Dr. Lei Wang and Yijing Liu did characterizations of the assembled structures and tested the performances of materials as motor and drug delivery tools.

5.1 Introduction

Artificial micro-/nanomachines have enormous applications in such as targeted drug delivery[171,172], separation of biomolecules or cells,[173-175] surface patterning,[176] and environmental remediation.[177] Whitesides *et al.* reported self-propelled plates capable of autonomous propulsion in the presence of chemical fuel in 2002.[178] Since then, tremendous progress has been achieved in the design and fabrication of micro-/nanomotors. Micro-/nanomotor systems that have been investigated include

multimetallic and dielectric particles,[179] bimetallic nanorods,[180-182] tubular catalytic microengines[183] and capsule motors.[184] A number of different driving mechanisms have been pursued for autonomous propulsion, including bubble recoil,[182] interfacial tension,[179,185] force fluctuations,[186] electrostatic forces,[187-189] Brownian ratcheting,[190] self-diffusiophoresis[191] and gravity.[181] Vesicular micro-/nanomotors are particularly attractive, because they can encapsulate active compounds (e.g., drugs) with minimal leakage and deliver the payload in a controlled manner. However, challenges still remain in the design and fabrication of vesicular motors. Wu *et al.* recently reported the use of microcontact printing to fabricate micro-sized capsules asymmetrically decorated with Pt nanoparticles (NPs) as motors.[184] However, this "top-down" approach provides limited control over the structures, and is not capable of mass production.

In the past decade, microfluidic technology has emerged as a powerful platform for a wide range of applications such as bioanalysis,[192] tissue engineering,[193] cellular biology,[194] and chemical synthesis/assembly.[94,195] Microfluidics offers several advantages over conventional batch reaction or assembly, such as continuous and automatic processing, precise control over synthetic conditions, and high reproducibility.[195] Microfluidic approaches have been used for the assembly of amphiphilic building blocks such as lipids, BCPs, and inorganic NPs into vesicular structures with superior controllability.[79,195,196] Our group has recently reported the self-assembly of NPAMs with AuNR or AuNP cores into functional hybrid materials in the microfluidic devices. The microfluidic method allows the manipulation of the

hydrodynamics of fluids in time and space, thus enabling us to control the self-assembly kinetics to generate a range of hybrid nanostructures, such as micelles, giant vesicles, and disks.[79,94] However, to date, there has been no report of continuous microfluidic synthesis of nano- or micro-motors.

This chapter describes the use of a microfluidic flow-focusing device (μFFD) for the single-step, template-free self-assembly of polymer/inorganic NP hybrid, Janus-like vesicles (JVs) that can act as vesicular motors.[196] The JVs are asymmetrically functionalized with inorganic NPs in the two distinct halves of their membranes. We use laminar flow in a microfluidic device to create Janus-like motors through the assembly of a mixture of amphiphilic BCPs and NPAMs (Figure 5.1 a). This approach affords us control over both the overall diameter of JVs (in the range of 400 nm to 2600 nm) and the surface coverage of inorganic NPs in the vesicular membranes. When platinum NPs (PtNPs) are integrated asymmetrically in the vesicular membranes, the JVs can undergo autonomous propulsion through the decomposition of hydrogen peroxide (Figure 5.1 b). In addition, the vesicles can be used to encapsulate active compounds, and the release of this payload can be achieved using NIR light. These JVs, therefore, combine autonomous propulsion and the encapsulation and release of active compounds into a single system.

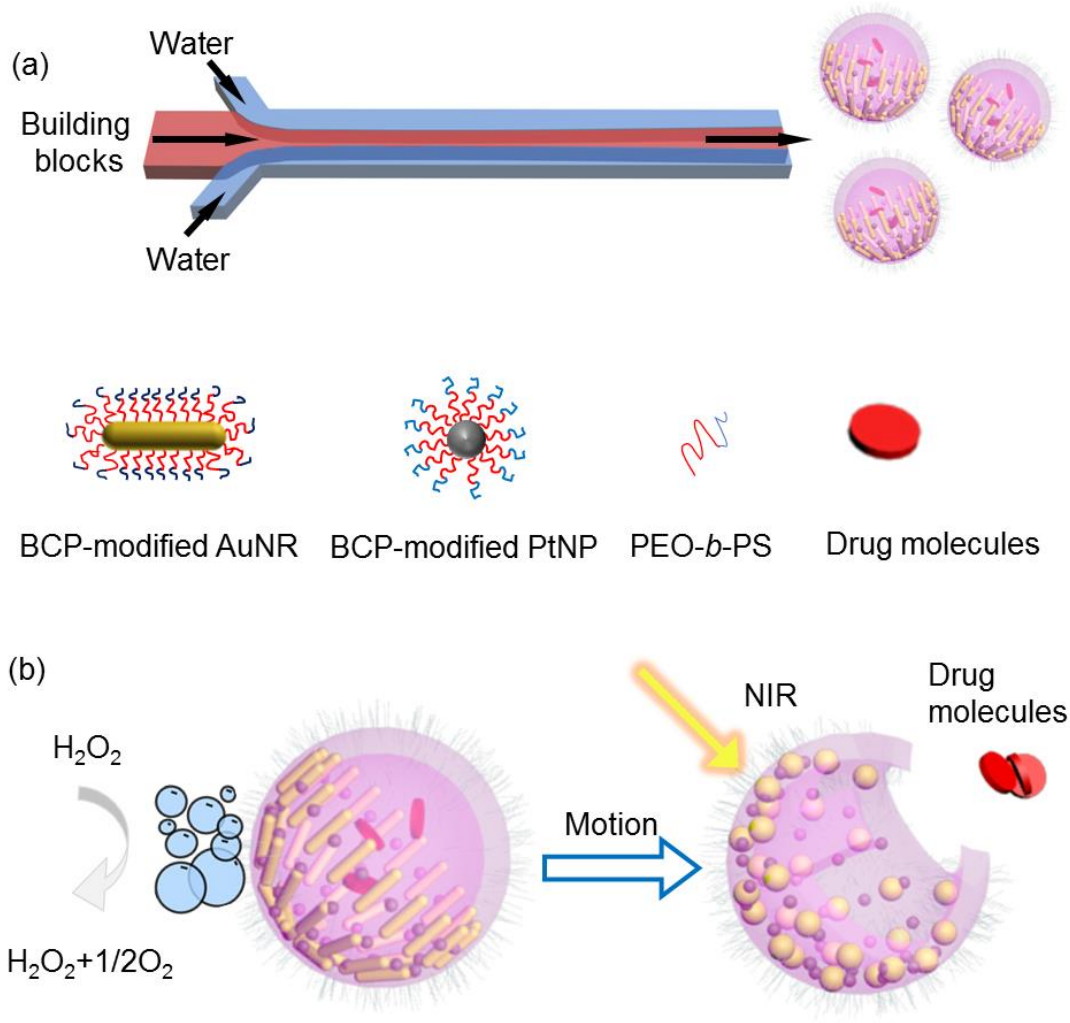

Figure 5.1. a) Schematic illustration of the self-assembly of a mixture of building blocks (i.e., BCP modified AuNRs/PtNPs and free BCPs) into JVs in MFFDs. The assembly building blocks were dispersed in THF. The THF flow was sheathed by two water streams. b) Scheme of the self- propelling of JVs in the presence of hydrogen peroxide (H_2O_2) as fuel and the payload release from JVs upon the irradiation of NIR light.

5.2 Experiments

5.2.1 Materials

Acetone, $NaBH_4$, CTAB, $HAuCl_4$, NaOL, $AgNO_3$, HCl, ascorbic acid, sodium citrate, H_2PtCl_6, ethylene glycol, $NaNO_3$, poly(vinyl pyrrolidone) (PVP, MW = 55, 000, 30 mM as calculated in terms of the repeating unit, THF, DMF were all purchased from Sigma Aldrich. Pure water was used in all the aqueous solution.

5.2.2 Design of microfluidic devices.

μFFDs were fabricated in poly(dimethyl) siloxane (PDMS) using a standard soft lithography method.[79,197] Briefly, a 10:1 (weight ratio) mixture of silicone elastomer oligomer and cross-linker (Sylgard 184 Silicone Elastomer Kit, Dow Corning, USA) was poured over a master with relief patterns on silicon wafer, followed by curing for 6 h at 65 ℃. After curing, the PDMS replica was peeled off from the wafer and cut into individual devices. Blunt needles were used to punch inlets and outlets of the devices. Immediately after oxygen plasma treatment, the PDMS device was bonded onto another piece of plasma-treated glass or PDMS substrate. The detailed dimensions of the MFFD are illustrated in Figure 5.4.

5.2.3 Synthesis of CTAB/NaOL covered AuNRs, AuNPs and PtNPs.

AuNRs of different aspect ratio were synthesized according to a previously reported method with minor modifications.[198] Briefly, a seed solution was prepared by rapidly injecting 600 uL of freshly prepared 0.01M $NaBH_4$ into a 10 mL solution

of 0.1 M CTAB and 2.5×10^{-4} M $HAuCl_4$ under rapid stirring. The solution was kept in a 29 ℃ water bath for about 1h before use. CTAB, NaOL, $AgNO_3$, HCl, and seed solution at specific molar ratios depending on the targeted aspect ratio of AuNRs were consecutively added into the reaction flask. Take the AuNRs with aspect ratio of 80:20 as an example, A 5.40 g mass of CTAB and 0.7404 g mass of NaOL were mixed in a 500 mL Erlenmeyer flask and dissolved in 150 mL water under heating. After cooling to room temperature, the solution was put into a 30 ℃ water bath after adding 10.8 mL of 7.2 mM $AgNO_3$. After 15 minutes, a 150 mL solution containing 0.0591 g $HAuCl_4$ was quickly added to the solution with stirring at 700 rpm. The solution was slowly reduced by the sodium oleate and would eventually become clear. A 1.26 mL volume of HCl (37%) was injected into the solution with stirring at 400 rpm about 90 minutes later. After another 15 minutes, a 750 uL solution of 0.064 M ascorbic acid was injected into the solution immediately followed by adding 480 uL seed solution. Stirring was stopped and the solution was placed in a 30 ℃ water bath overnight. The product was purified and concentrated by centrifuging twice for future use.

The synthesis of 50 nm AuNPs is referred to experimental section in Chapter 4

The synthesis of PtNPs was conducted using a method reported previously.[199] In brief, a 1 mL of 80 mM H_2PtCl_6 solution in ethylene glycol was rapidly injected to 7 mL ethylene glycol (kept in oil bath with 160 ℃) containing both $NaNO_3$ (110 mM) and poly(vinyl pyrrolidone) (PVP, MW = 55 000, Sigma, 30 mM as calculated in terms of the repeating unit). After the injection of H_2PtCl_6 solution, the solution was kept at 160 ℃ for about 30 min. The sample was washed after it was cooled

down in air to room temperature. A 5 mL of acetone was added into 10 mL of the PtNP solution, followed by centrifuge at 1500 rpm for 15 min. After removing the surfactant, the PtNPs were then redispersed in water.

5.2.4 Synthesis of thiol-terminated BCPs and surface modification of NPs.

The synthesis of thiol-terminated BCPs is referred to experimental sections in Chapter 2. The surface modification of AuNPs is referred to experimental section in Chapter 3.

5.2.5 Self-assembly of JVs.

The self-assembly of a mixture of building blocks (that is, free BCP of PEO_{45}-*b*-PS_{455} without thiol group and AuNRs modified with PEO_{45}-*b*-PS_{455}-SH) was performed in PDMS-based MFFDs. The final concentration of AuNRs modified with PS-*b*-PEO is about 1 mg/mL, while the final concentration of PtNPs modified with PS-*b*-PEO is about 0.5 mg/mL. Water was injected into the device from two side channels, while a solution of assembly building blocks in THF was injected from a center channel using syringe pumps. The assembled JVs were collected from the outlet of the MFFDs, after the laminar flow of fluids was stabilized for a few minutes. When a mixture of free BCP of PEO_{45}-*b*-PS_{455}, BCP-modified AuNRs, and BCP-modified PtNPs was used, the assembly process generated vesicles comprising both AuNRs and PtNPs in the NP half of the vesicular membranes.

5.2.6 Characterization of assembled JVs.

A Hitachi SU-70 Schottky field emission gun Scanning Electron Microscope (FEG-SEM) and a JEOL FEG Transmission Electron Microscope (FEG-TEM) were applied for the images of the samples. All the samples for SEM were prepared by casting a 5-10 μL of aqueous solution on silicon wafers, and dried at room temperature. TEM samples were prepared from the casting on 300 mesh copper grids covered with carbon film, and dried at room temperature.

5.2.7 Motion of vesicular motors.

A diluted solution of Janus micromotors was mixed with equal volumes of hydrogen peroxide (Sigma, US) fuel solution with different concentration (v/v, 10-30%). The motion of micromotor was captured using a Nikon Eclipse Ti-S fluorescence microscope equipped with a high-speed camera (frame acquisition time 1 μs). The videos of motor movement were taken 2 min after the stabilization of the system. All the optical microscope images of motor movement were tracked using the Metamorph tracking module, and the results were analyzed using Image J software.

5.2.8 Encapsulation and NIR-triggered release of a model compound.

To examine the controlled release, RB was used as a model drug. A 50 μL of RB in THF solution (1 mg/mL) was first mixed with a 1 mL THF solution containing AuNPs, PtNPs and free PEO_{45}-*b*-PS_{455}. The self-assembly was conducted at Q_{THF} =40 μL/min and Q_{H2O} =60 μL/min. The solution of JVs was centrifuged to remove the

unloaded dye molecules by gentle centrifugation. The JVs were redispersed in water by gently shaking. A 500 μL of the RB-loaded solution was then transferred to a dialysis cap with a molecular weight cutoff of 6,000-8,000 Daltons. The cap was placed on the top of UV cells filled with pure water.

5.3 Results and discussion

5.3.1 The synthesized Inorganic NPs

The synthesized AuNPs have an average diameter of 48.0±6.0 nm and an absorption peak of 535 nm (Figure 5.2 c and d). The AuNRs have an aspect ratio close to 4, with its average longitude length of 80.5 ± 8 nm (Figure 5.2 a). The star-like PtNPs with an average diameter of 20 nm were obtained.

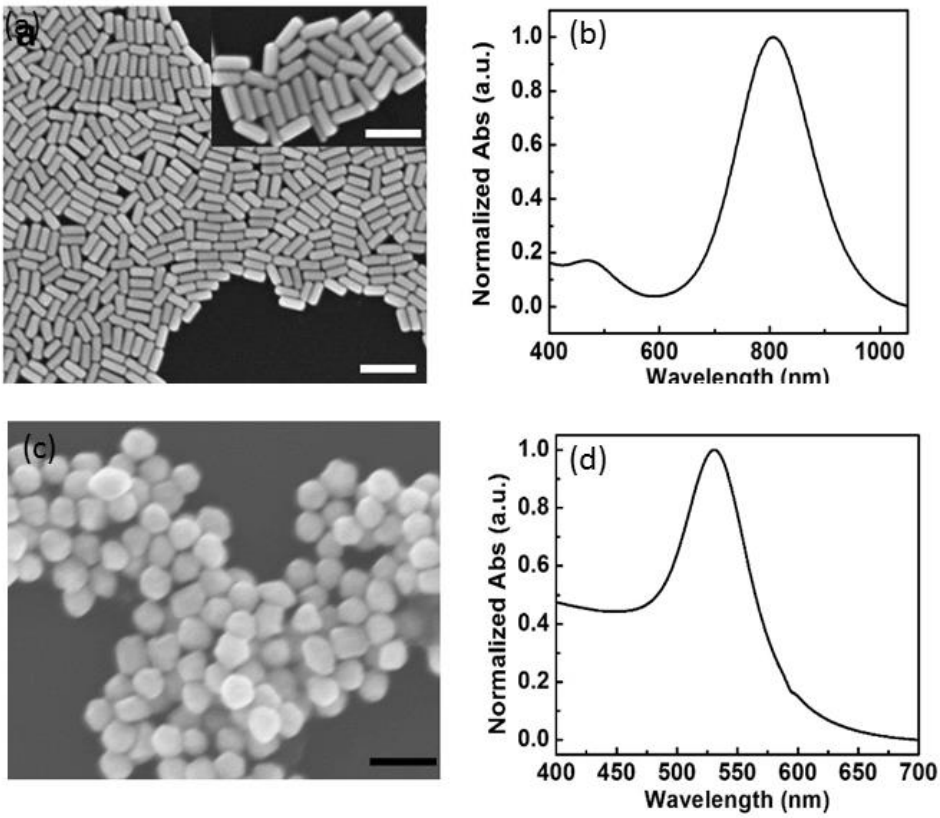

Figure 5.2. SEM and Uv-vis characterizations of AuNRs and AuNPs (a) SEM of AuNRs with an aspect ratio of ~80: 20 and (b) corresponding absorption spectrum. (c) SEM of 50 nm AuNP and (d) corresponding absorption spectrum. Scale bars: 200 nm in (a) and 100 nm in (c).

5.3.2 Janus vesicles based on AuNRs or AuNPs

The JVs were fabricated by continuously co-assembly of a mixture of free PEO-*b*-PS and NPAMs comprising inorganic NPs tethered with thiol-terminated PEO-*b*-PS in a μFFD (Figure 5.3).

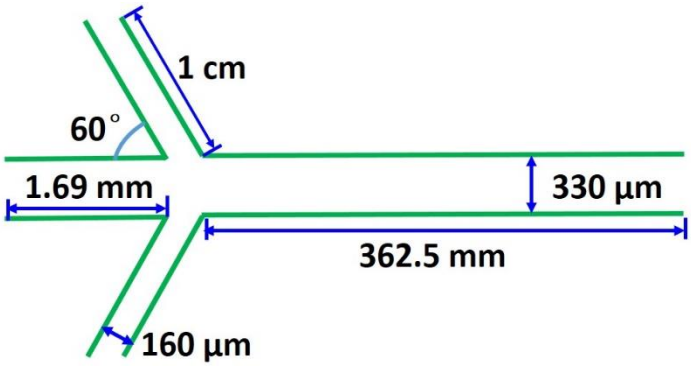

Figure 5.3. Schematic illustration of the dimension of a MFFD. The distances from the inlets to the junctions are 1.7 mm (main channel) and 10 mm (side channel), respectively. The total length of the main channel was 346.5 mm. The height and width of the main channel is 100 and 330 µm, respectively. The width of the side channel is 120 µm.

Amphiphilic BCP and NPAMs are known to self-assemble into a range of nanostructures particularly vesicles in selective solvents.[76,78,99] To generate JVs, a THF solution containing the mixture of building blocks was introduced into the central channel, while two streams of water, which is nonsolvent for PS blocks of BCPs, were introduced from two side channels (Figure 5.1 a). The flows of fluids were forced to enter a common downstream channel and formed a laminar flow of three streams, due to the low Reynolds' numbers (ranging from 0.1 to 5) of fluids in the microchannels. The diffusive mixing between two miscible liquids along the transverse direction changed the quality of solvents for both molecular building blocks and NPAMs at the biphasic boundary, thus triggering the formation of JVs.[79] The assembly of Janus vesicles with two distinct halves rather than vesicles with a

random distribution of NPs can be explained by the lateral phase separation between free BCPs and polymer-tethered NPs in the membranes as we discussed in chapter 3.[78] The JVs were obtained within a wide range of flow rates in the μFFDs. This microfluidic strategy is applicable to the self-assembly of various NPs (*i.e.*, AuNRs, AuNPs, and PtNPs). The integration of inorganic NPs in the membrane of JVs impart the system with unique functionality arising from the intrinsic optical, electronic, and catalytic properties.

Figures 5.4 shows the representative JVs assembled from a mixture of PEO_{45}-*b*-PS_{455} and AuNRs modified with PEO_{45}-*b*-PS_{455}-SH at Q_{H_2O}=60 μL/min and Q_{THF}=40 μL/min (Q represents the volumetric flow rate of the liquids).

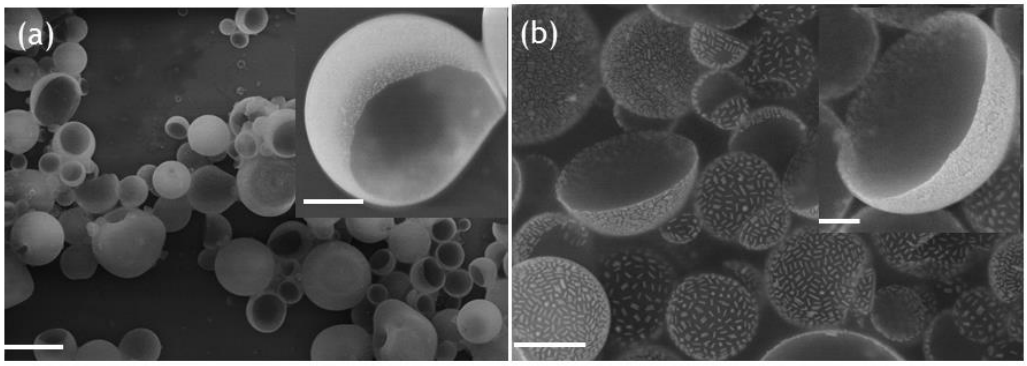

Figure 5.4. SEM (a, b) of JVs assembled from a mixture building blocks of free PEO_{45}-*b*-PS_{455} and AuNRs tethered with BCPs of PEO_{45}-*b*-PS_{455}-SH. The assembly conditions are: Q_{H2O}= 60 μL/min, Q_{THF}= 40 μL/min for vesicles in (a) and Q_{H2O}= 80 μL/min, Q_{THF}= 40 μL/min for vesicles (b). The insets in (a, b) are high magnification images of vesicles. Inset image in (a) shows that the JV is hollow. Scale bars are: 2 μm (a), 500 nm (b), and 500 nm for inset in (a) and 200 nm for inset in (b).

The JVs with a hemispherical shape consist of two distinct halves: one includes a single layer of densely packed AuNRs in the membrane and another is composed of pure polymer (See large area SEM image and size distribution analysis of JVs in Figure 5.5).

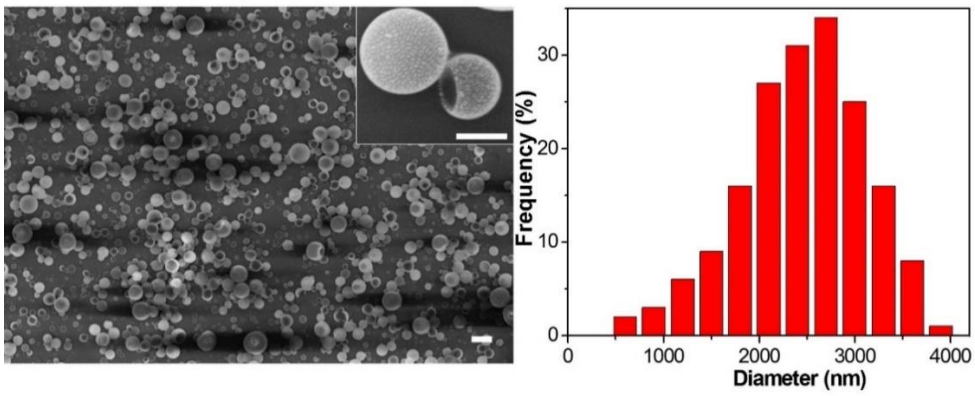

Figure 5.5. JVs assembled from a mixture of free BCP of PEO_{45}-*b*-PS_{455} and AuNRs (an aspect ratio of ~80:20) tethered with BCP of PEO_{45}-*b*-PS_{455}-SH at Q_{water} of 60 µL/min and Q_{THF} of 40 µL/min. Scale bars are 3 µm.

When only single type of building blocks was used, the assembly process produced common vesicles made from either pure PS-*b*-PEO or NPs tethered with PS-*b*-PEO (see Figure 5.6), rather than Janus-like vesicles with two halves.

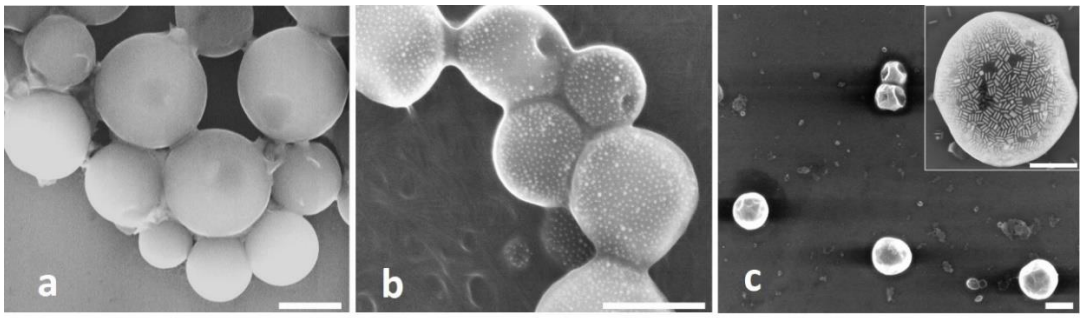

Figure 5.6. SEM images of the structures assembled from pure PS-b-PEO (a), pure AuNPs tethered PS-b-PEOs (b), and pure AuNRs tethered PS-b-PEOs (c). Sample a, b, and c were obtained at Q_{water} of 60 μL/min and Q_{THF} of 40 μL/min. All the scale bars are 1 μm.

The average diameters of the vesicles in Figure 5.4 a and b are 1.86±0.47 μm and 0.92±0.68 μm, respectively. The polymer-rich half is nearly flat while the AuNRs-rich half remains arched, largely due to enhanced Young's modulus arising from the rigid inorganic NPs. The interior of the JVs is hollow, as clearly indicated by the occasional broken JV (inset image in Figure 5.4 a). The relative surface ratio of polymer-rich domain to NP-rich domain in JVs can be tuned by controlling the ratio of individual building blocks in the mixture. With the increase of free polymer concentration from 0.1 to 0.3 mg/mL, the percentage of polymer-rich domain coverage increased from 15.4% to 40.4% (Figure 5.7)

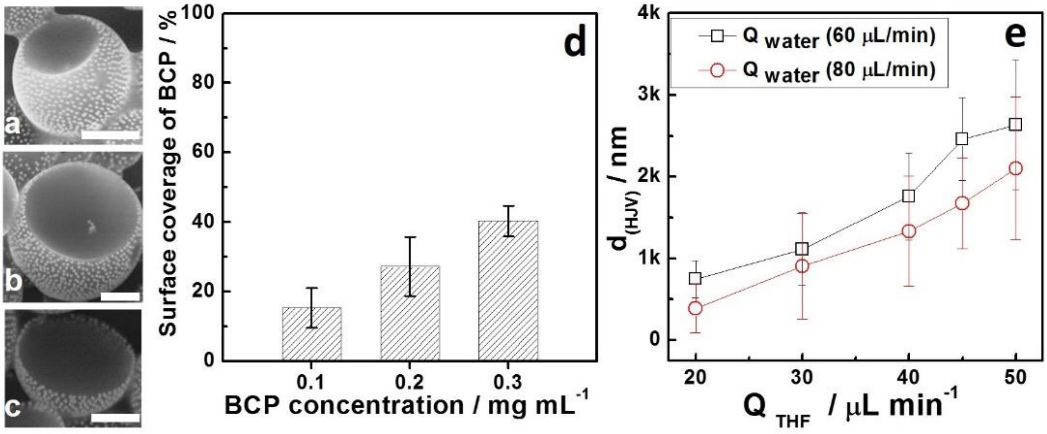

Figure 5.7. The control over the domains of the phase separated vesicles. (a-c) SEM images of JVs obtained from assembly system containing 0.1 mg/mL (a), 0.2 mg/mL (b) and 0.3 mg/mL (c) free BCP of PEO_{45}-*b*-PS_{455} and ~0.2 mg/mL NPs. The flow

conditions are: Q_{H2O}=60 μL/min and Q_{THF}=40 μL/min. The scale bars are 500 nm. (d) A histogram plot of the percentage of AuNPs-rich domain as a function of free BCP concentration. (e) The average overall diameter (d_{JV}) of JVs as a function of the flow rates of THF phase.

Because the JVs are created in a microfluidic system rather than in a batch process, the average overall diameter (d_{JV}) of Janus vesicles can be controlled dynamically by tuning the flow rates of the fluids. At Q_{H_2O} = 60 μL/min, the d_{JV} increases from 749.2 ± 228.3 to 2634.2 ± 795.3 nm with the increase of Q_{THF} from 20 to 50 μL/min (Figure 5.7 e). We believe that the relatively broad size distribution of JVs is due to the flow velocity distribution in the channel, i.e. the flow velocity near the channel walls is slower than the central of the channel. A similar trend was also observed for assembly at Q_{H_2O} = 80 μL/min. The d_{JV} increased from 388.5 ±294.2 nm to 2104.3 ±872.5 nm with the increase of Q_{THF} from 20 to 50 μL/min. At the same Q_{THF}, the larger d_{JV} obtained at Q_{H_2O} = 60 μL/min than that at Q_{H_2O} = 80 μL/min can be explained by enhanced mixing of two streams at a higher Peclet number ($\boldsymbol{Pe} \propto Q_{total} = Q_{H_2O} + Q_{THF}$).[200]

The assembly kinetics and hence the dependence of d_{JV} on the flow rates in MFFDs is largely determined by how fast the building blocks diffuse to interact with water, that is, the mixing time (t_{mix}).[201,202] The t_{mix} is defined as:[202]

$$t_{mix} \sim \frac{w_f^2}{4D} \approx \frac{w^2}{9D(1+1/R)^2} \qquad \text{(Eq. 5.1)}$$

where w_f, w, D and R are the width of the central stream, the width of the downstream

channel, the diffusion coefficient of water-THF, and the flow-rate ratio of the THF-to-water stream (R = Q_{THF}/Q_{H_2O}), respectively. At small t_{mix}, the building blocks can interact quickly with water, resulting in a fast quenching of the assembly process to form JVs with smaller d_{JV}. A small large t_{mix} allows the continuous recruitment of building blocks to form larger JVs. For instance, keeping Q_{H_2O} as a constant, an increase in Q_{THF} (central flow) increases w_f, thus leading to a longer t_{mix} and hence the formation of larger vesicles.

5.3.3 JVs as catalytic motors

The introduction of PtNPs into one half of JVs allows the vesicles to self-propel in the presence of hydrogen peroxide (H_2O_2). The catalytic decomposition of H_2O_2 at one side of JVs drives the movement of vesicular motors (Figure 5.8).[172,174,203] Optical images in Figure 5.8 a and b show the obvious autonomous propulsion of a JV motor (red circle) in a 10% H_2O_2 aqueous solution.

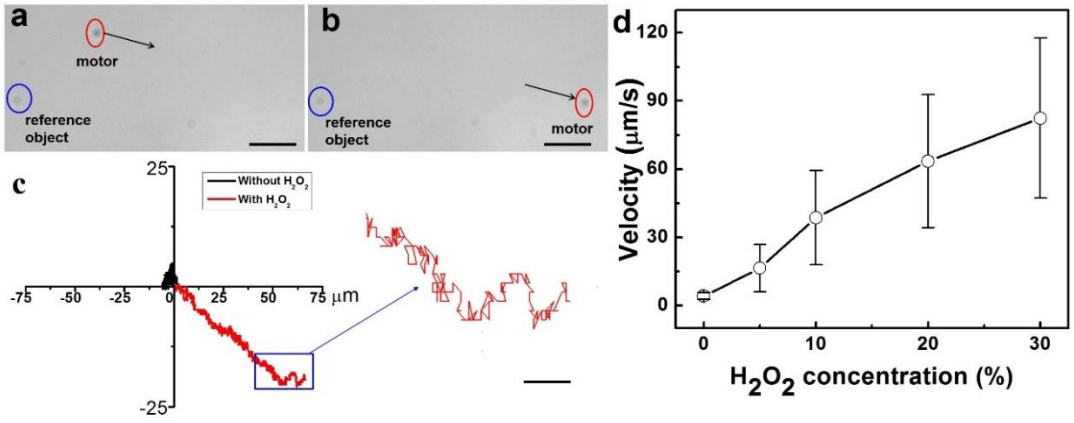

Figure 5.8. Motion of JVs asymmetrically integrated with PtNPs as catalytic motors. (a, b) The snapshots of the movement of vesicular motor (red circle) in the presence

of 10% hydrogen peroxide. Few polymer microbeads were added as reference objects (blue circle). The scale bars are 20 μm. (c) The trajectory of vesicular motor with (black) and without (red) the addition of hydrogen peroxide as chemical fuel. Scale bar is 4 μm. (d) The average velocity of the JV motors as a function of the concentration of hydrogen peroxide (more than 20 motors were analyzed for each point).

A microsphere (blue circle) was intentionally introduced into the system to serve as reference point. The motion trajectories of the motor with (red plot) and without (black plot) the addition of H_2O_2 as fuel further confirmed the directional movement of the Janus vesicle (Figure 5.8 c). In the absence of fuel, the vesicle showed a typical random walk behavior as a result of Brownian motion. The trajectory of motion was random and localized within a small area. When H_2O_2 was added, the motion of the catalytic vesicular motor was relatively directional. The motion velocity of the motor can be controlled by adjusting the concentration of H_2O_2. The average velocity of the Janus motor increased from ~2 μm/s at 0% H_2O_2 to ~90 μm/s at 30% H_2O_2, as a result of faster catalytic decomposition of H_2O_2 (Figure 5.8 d).

5.3.4 Controlled release of RB

In addition to autonomous motion, we further demonstrate the effective encapsulation and delivery of compounds using JVs. As a proof of concept, we encapsulated rhodamine B (RB) in JVs containing AuNRs and PtNPs in the NP half (Figure 5.9). The controlled release of payload from JVs was achieved by the irradiation with NIR light, due to the photothermal effect of AuNRs in the vesicular

membranes. After the encapsulation of RB in JVs during self-assembly, the samples were centrifuged to remove free (unloaded) RB. Upon the irradiation of NIR light (808 nm, 60 mW), the intense localized heating disrupted the membranes of JVs, thus triggering the release of encapsulated RB from the vesicles into water. The fluorescence intensity of the sample increased linearly as a function of irradiation time, and reached a plateau after about 70 min (Figure 5.10 b).

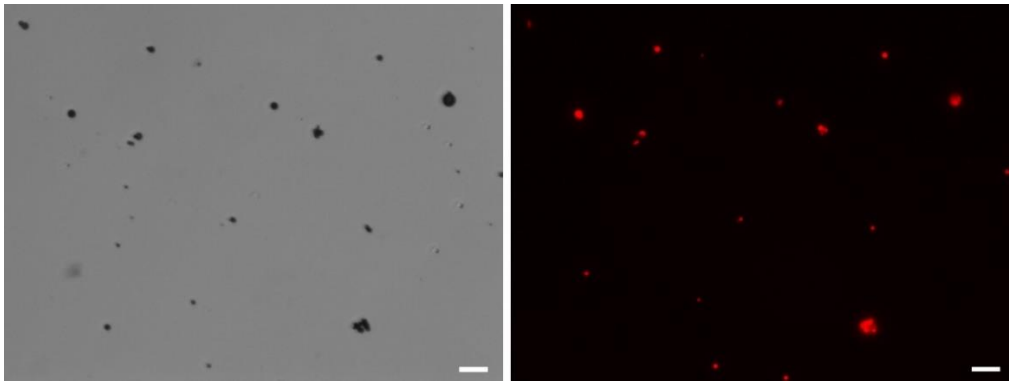

Figure 5.9. Optical and fluorescence images of JVs encapsulated with RB. Scale bars are 10 μm.

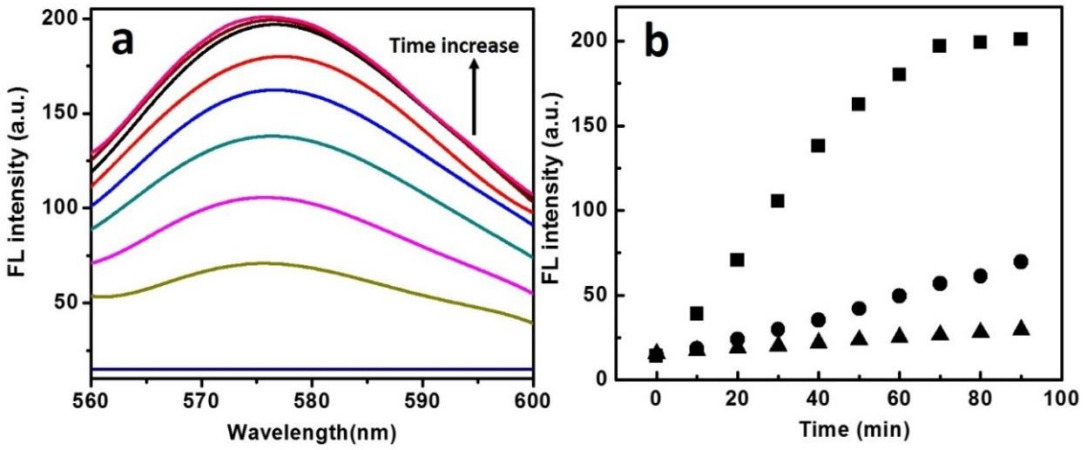

Figure 5.10. NIR-triggered release of encapsulated rhodamine B (RB) from JVs. a)

Fluorescence spectra of the release of RB (excitation at 540 nm) from JVs upon the irradiation of 808 nm laser at a 10 min interval. b) The release profiles of JVs encapsulated with RB as a function of time with laser on (■). Both vesicles with full coverage of AuNRs (▲) and JVs (●) with laser off were used as control groups

In contrast, the florescence intensity of control groups (with laser off) only showed a slight increase, which can be ascribed to the leakage of RB from vesicles due to osmotic pressure difference across the vesicle membranes. This result confirmed that NIR irradiation can significantly accelerate the release of encapsulated compounds. A comparison of SEM images of the same vesicle before and after irradiation showed that the AuNRs in the vesicular membrane melted and possibly fused into AuNPs with broad size distribution, as a result of the intense localized heating (Figure 5.11). Through the demonstrations above, we can see there is a great potential for the combination of the controlled movement and localized release, which we are going to conduct in the near future.

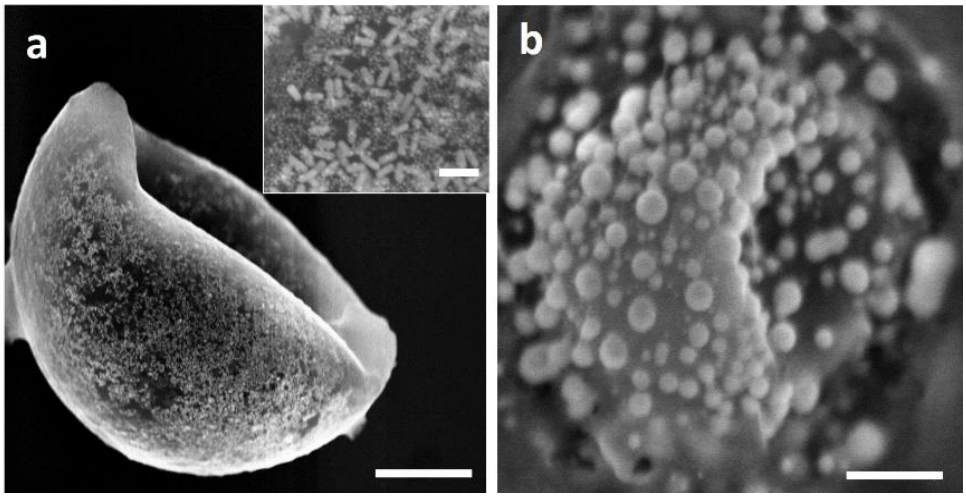

Figure 5.11. SEM images of JV containing AuNRs/PtNPs before (a) and after (b) laser irradiation. The inset in (a) is a low magnification SEM image of the membrane of JV. Scale bars are 500 nm in (a, b), and 100 nm in inset of (a).

5.4 Conclusions

In summary, we have developed a simple strategy for the continuous self-assembly of JVs with distinct halves of NP-rich domain and polymer-rich domain. Various inorganic NPs (*i.e.*, AuNPs, AuNRs, and PtNPs) can be selectively introduced to the vesicle membrane, thus imparting the vesicles with multifunctionality. The average diameter of JVs and the relative portion of the NP-rich domain can be tuned by controlling the flow rates of fluids and the relative concentration of individual building blocks. The JVs uniquely combined the capability of autonomous propulsion and externally controlled delivery of encapsulated payload. The velocity of such vesicular motors can be controlled by the concentration of chemical fuel of hydrogen peroxide, while the release of payload can

be externally triggered by NIR light on demand. The multifunctional JV-based motors may find applications in the separation of biomolecules or bacteria[173-175], drug delivery[183,184] and as micro-reactors.[204]

Chapter 6: Conclusions and Future work

6.1 Conclusions

The objective of this dissertation was to understand the self-assembly of NPAMs for better creation of inorganic/polymeric hybrid materials with biomedical applications. First, we investigated the effect of polymer density on the formation of hybrid vesicles with defined spatial arrangement of NPAMs in the membrane and the impact of NPAM arrangement on the performance of hybrid vesicles in photothermal imaging. We found that higher polymer density on the surfaces of NPs led to vesicles with NPs uniformly distributed within the polymer membrane, while lower polymer density on the surfaces of NPs led to vesicles containing chains of NPs within the membrane. By controlling the polymer grafting densities, we can tune the LSPR coupling between AuNPs to achieve the NIR absorption for bioapplications. Second, we studied the concurrent self-assembly of NPAMs with neat BCPPs and with a mixture of neat BCPs and hydrophobic MNPs. The concurrent self-assembly produced a range of spherical and non-spherical hybrid vesicles with different morphologies including patchy vesicles, homogeneous vesicles, and Janus vesicles with spherical, hemispherical, and disk-like shapes, by changing core size of NPAMs and length of BCPs. It was found that the maximization of the conformational entropy of the free BCPs drives the phase separation between constituent building blocks in the membrane. Moreover, the morphologies of assembled vesicles could be controlled by addition of hydrophobic NPs. The concurrent self-assembly enabled us to build hybrid vesicles containing multiple types of inorganic NPs. Third, we developed a

microfluidic approach for the continuous fabrication of Janus-like vesicles that can serve as micro-motors with autonomous propulsion driven by the decomposition of hydrogen peroxide. Fourth, we have demonstrated the application of assembled hybrid vesicles in PA imaging, MRI, photothermal therapy, and drug delivery. This systematic study will help us gain deeper understanding of the self-assembly of NPAMs into controllable nanostructures. By doing so, we will be able to control the collective properties of NP ensembles for various applications. This research will also provide new insights into the fundamental questions that must be overcome before the hybrid materials can be utilized in effective cancer imaging and treatment.

6.2 Future work

6.2.1 Self-assembly direction

As we have discussed in previous chapters, control over assembly kinetics offers a powerful strategy for the generation of hierarchical nanostructures by using NPAMs as assembly building blocks. However, the influence of kinetics also poses challenges in achieving complex structures with no or less defects, high reproducibility, and high uniformity. In order to achieve high-quality assembly structures, it is crucial to develop new assembly approaches for better control over the kinetics of assembly process. More efforts should be made to develop new analytical or characterization tools for real-time monitoring the assembly process and assembled structures as a function of time.

New NPAMs with complex inorganic NP cores should be designed for self-

assembly study. The shape and crystal facets of inorganic NPs will influence the distribution of polymer ligands on the surfaces of NPs. The uneven distribution of polymer ligands on NP surfaces can facilitate the step-wise hierarchical assembly of NPAMs into complex structures with various applications. However, both characterization and controlling of distribution of polymer ligands on the surfaces of NPs remain as challenges. One possible starting point is to use Janus or patchy particles as cores of NPAMs, Different polymer ligands can be functioned separately to their surfaces due to the different chemical compositions of Janus or patchy NPs. The NPAMs with Janus or patchy particle cores resemble molecular amphiphiles, as they can self-assemble into a variety of structures in solution and or at the interface of gas/liquid or liquid/liquid. For instance, Pine et al. used patchy particles with defined valences as 'colloidal molecules' with different bonding symmetries for self-assembly.[205] The self-assembly of anisotropic NPs demands alignment of NPs in desired direction that will increase the complexity of assembly structures.

6.2.2 Bioapplication directions

For successful clinical translation, at least the following challenges need to be resolved. First, we need to further decrease the size of hybrid materials while not sacrificing the physical properties (*e.g.*, LSPR) of the assembled structures. The preferred size of hybrid materials is below 100 nm, in order to facilitate long-term circulation and tumor targeting.[206] For example, The Ijiro group have successfully prepared the sub-100 nm AuNP vesicles.[207] However, small AuNPs had to be used to reduce the size of vesicles, leading to the weak LSPR coupling of assemblies. Second,

more efforts should be made in designing responsive hybrid materials to facilitate the release of payload or enhance therapeutic efficacy. For example, hybrid materials that are responsive to enzymatic, pH or temperature stimuli can drastically improve the specificity of targeted drug delivery to tumors and effectively reduced the side effect of chemotherapy. Third, guaranteeing long-term safety of nanomaterials in terms of clearance and toxicity is one of the major obstacles for their in vivo biomedical applications. To solve the above-mentioned problems, the cooperation between researchers from different fields are needed.

Appendices

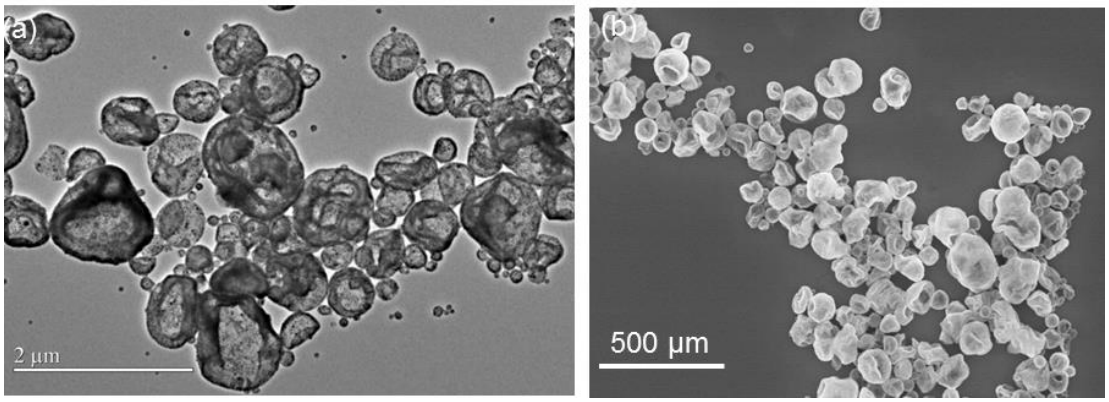

Figure 2.S1. Large area (a) TEM and (b) SEM images of the chain vesicles

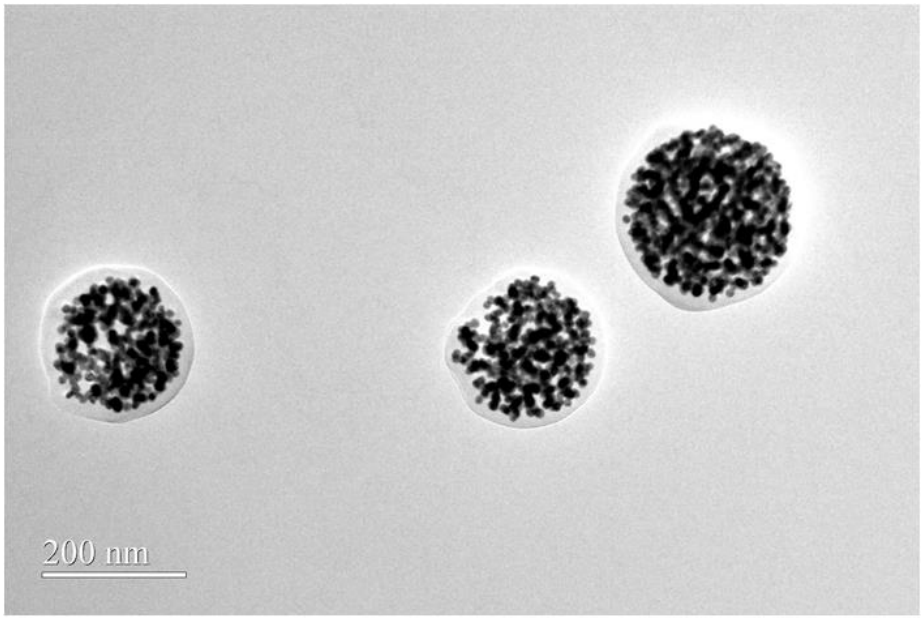

Figure 2.S2. TEM image of the chain vesicles made from BCP-AuNPs (13) with a grafting density of 0.03 chain/nm^2 when water content reached 20% in volume.

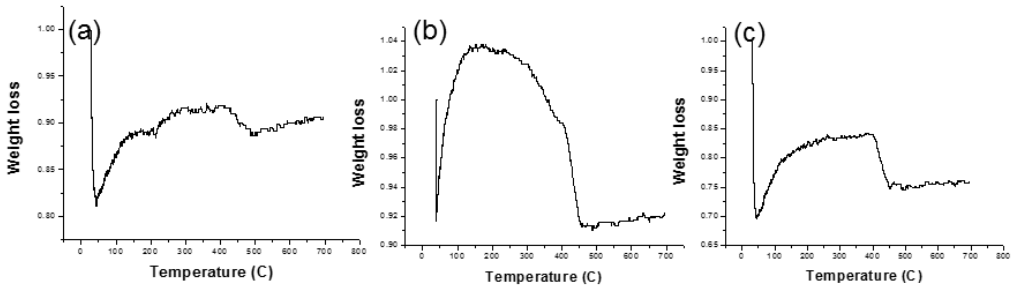

Figure 2.S3. The TGA results obtained for the δ of BCP-AuNPs that are able to form chain vesicles and non-chain vesicles. The δ for three samples are (a) 0.03 chain/nm^2, (b) 0.05 chian/nm^2, and (c) 0.08 chain/nm^2.

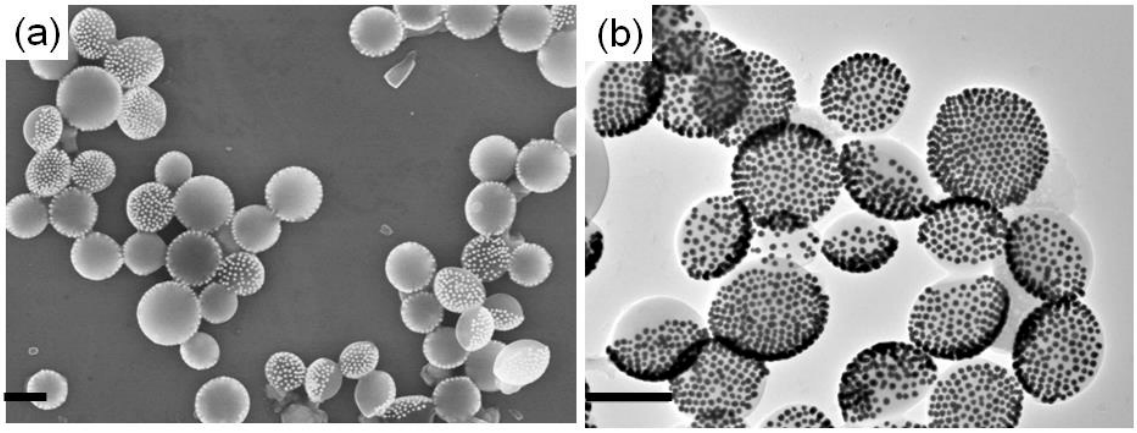

Figure 3.S1. (a) SEM and (b) TEM image of hybrid JVs with disk-like shape assembled from Au-40-PS_{455}-b-PEO_{45}/PS_{307}-b-PEO_5. Scale bars: 600 nm

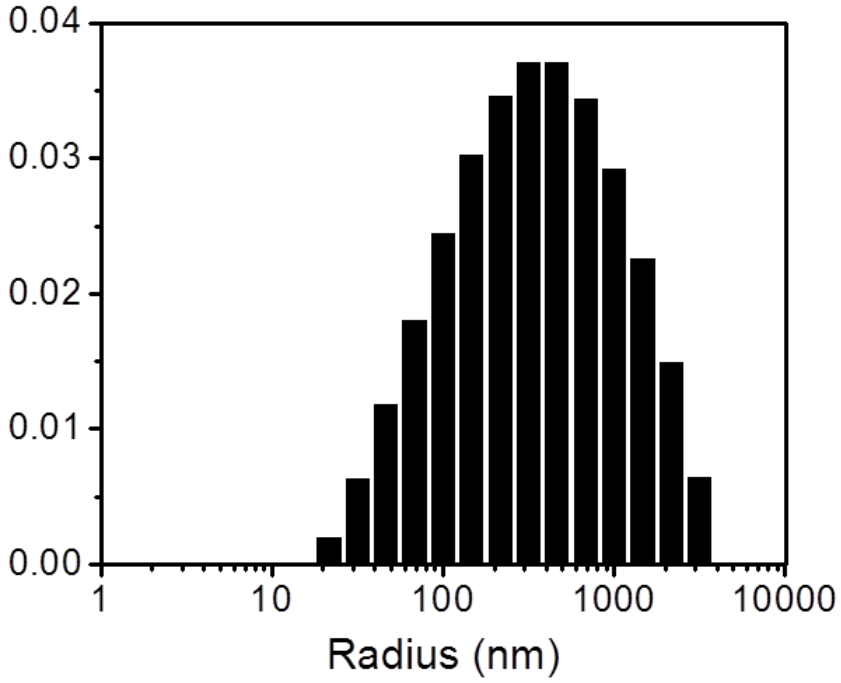

Figure 3.S2. DLS analysis of hybrid JVs with disk-like shape assembled from Au-40-PS_{455}-*b*-PEO_{45}/PS_{307}-*b*-PEO_5 indicates that the hydrodynamic radius is ca. 307.3 nm

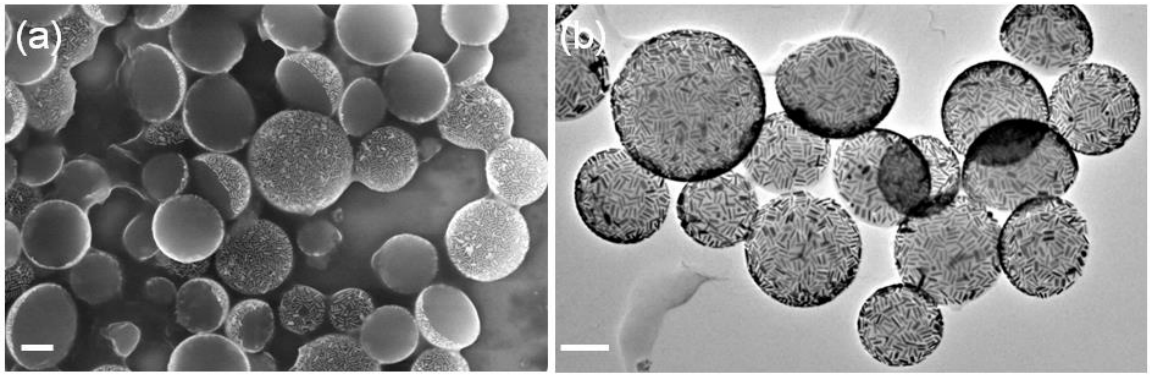

Figure 3.S3. (a) SEM and (b) TEM image of HJVs with disk-like shape assembled from Au(NR)-40-PS_{455}-*b*-PEO_{45}/PS_{307}-*b*-PEO_5. Scale bars: 400 nm

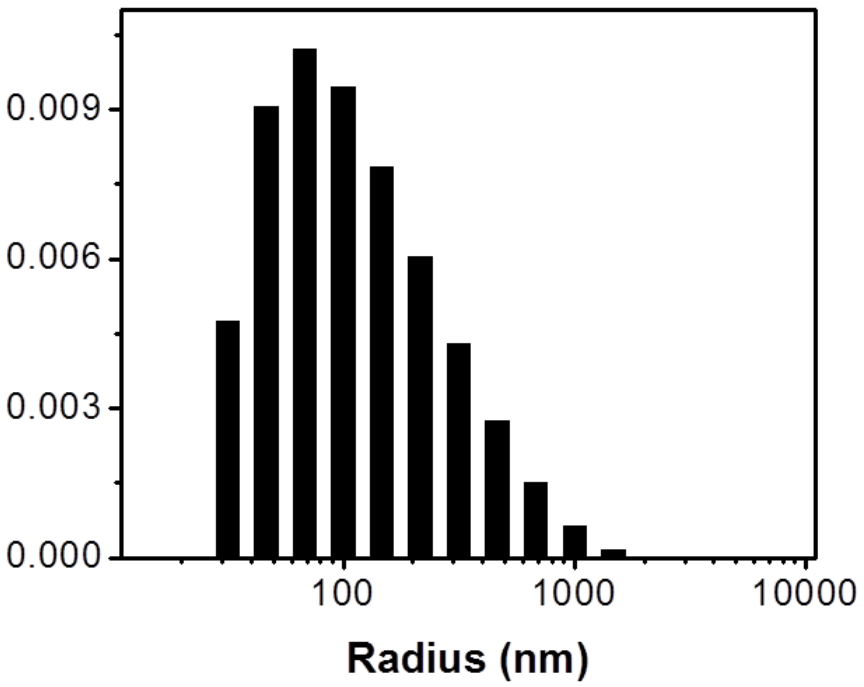

Figure 3.S4. DLS analysis of hybrid JVs with disk-like shape assembled from Au(NR)-40-PS_{455}-*b*-PEO_{45}/PS_{307}-*b*-PEO_5 indicates that the hydrodynamic radius is ca. 204.5 nm

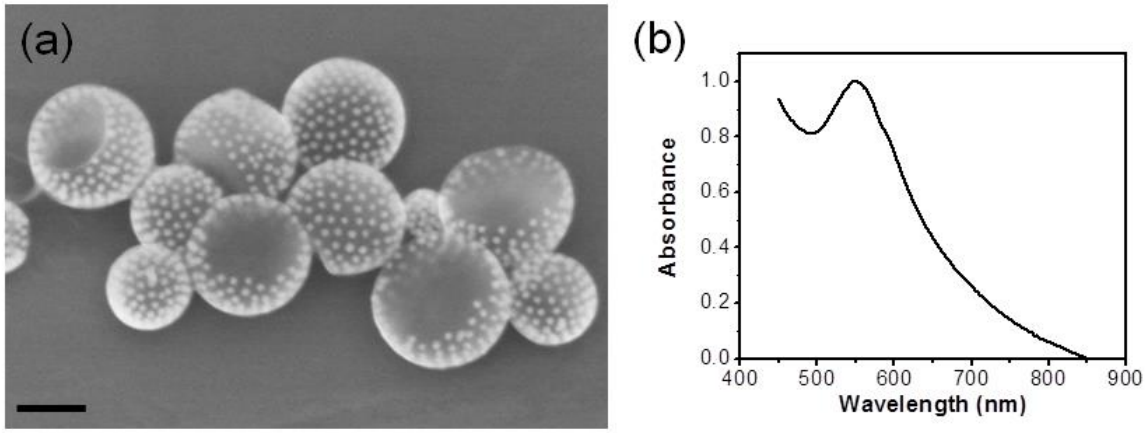

Figure 3.S5. SEM image and corresponding UV-vis spectra of JVs. (a) SEM image

of hybrid JVs with hemispherical shape assembled from Au-19-PS_{211}-*b*-PEO_{45}/PS_{307}-*b*-PEO_5. Scale bar: 150 nm. (b) The corresponding UV-vis spectra of the hybrid JVs.

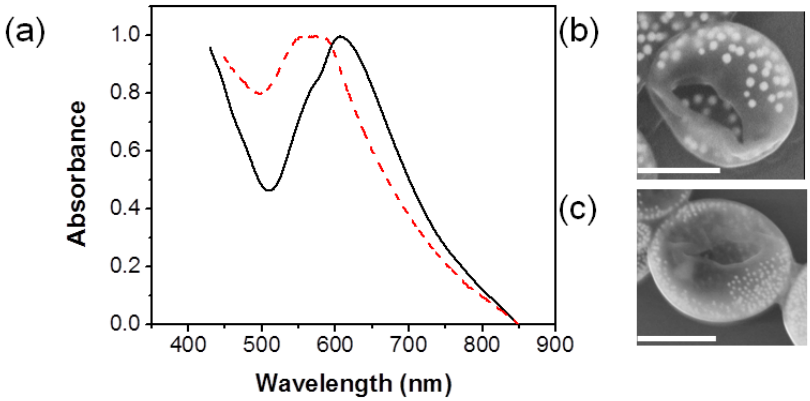

Figure 3.S6. UV-vis spectra and SEM of hybrid JVs composed of NPAMs with different cores. (a) UV-vis spectra of hybrid JVs with 19 nm (dash) and 40 nm (solid) AuNPs as the cores of the NPAMs. The results indicate that the assembly of AuNPs within vesicular membranes led to the red-shift of plasmonic band, due to the coupling between AuNPs. (b) SEM image of hybrid JVs with spherical shape assembled from Au-40-PS_{455}-*b*-PEO_{45}/PS_{307}-*b*-PEO_{45}. (c) SEM image of hybrid JVs with spherical shape assembled from Au-19-PS_{211}-*b*-PEO_{45}/PS_{307}-*b*-PEO_{45}.

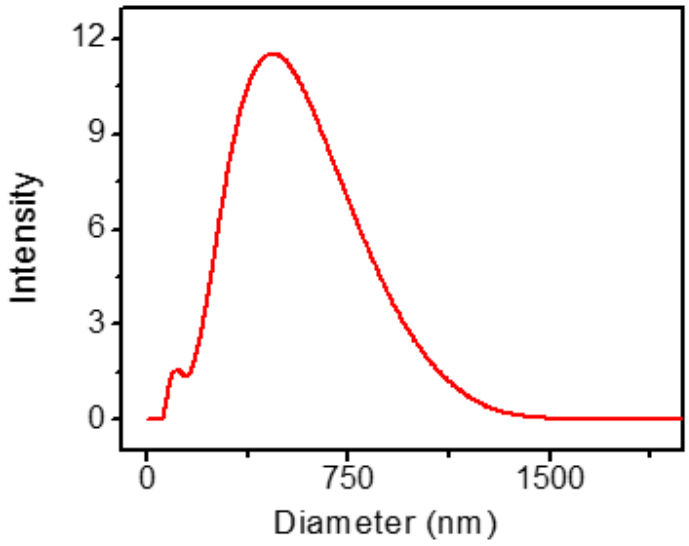

Figure 4.S1. DLS data of the JSVs made from NPAMs with 50 nm cores, PS_{107}-*b*-PAA_4, and 15 nm MNPs. The average diameter of the hybrid vesicles form DLS is 570.8 ± 93.2 nm

.

List of my publications

1. Y. Liu, Y.J. Liu, J,J Yin, Z.H. Nie, Self-assembly of amphiphilic block polymer-tethered nanoparticles: a new approach to nanoscale design of functional materials, *Macromol. Rapid Commun.* **2015**, 36, 711−725

2. Y.J Liu, B. Liu, Z.H. Nie, Concurrent self-assembly of molecular and colloidal amphiphiles into nanoarchitectures with increasing complexity, *Nano Today* **2015**, 136, 2602-2610.

3. L. Wang, Y.J. Liu (co-first author), J. He, M. J. Hourwitz, J. Athas, Y.l. Yang, J. T. Fourkas, X.J. Han,and Z.H. Nie, Continuous microfluidic self-assembly of hybrid Janus-like vesicular motors: Autonomous propulsion and controlled release, *Small* **2015**, doi: 10.1002/smll.201500527

4. Y.J. Liu, Y.C. Li, J. He, K. Duelge, Z.Y. Lu, and Z.H. Nie, Entropy-driven pattern formation of hybrid vesicular assemblies of binary molecular and nanoparticle amphiphiles, *J. Am. Chem. Soc.* **2014**, 136, 2602-2610

5. J. He, X.L. Huang, Y.C. Li, Y.J. Liu, T. Babu, M.A. Aronova, S.J. Wang, Z.Y. Lu, X.Y. Chen, Z.H. Nie, Self-assembly of amphiphilic plasmonic micelle-like nanoparticles in selective solvents, *J. Am. Chem. Soc.* **2013**, 135, 7974–7984.

6. J. He, Y.J. Liu, T. C. Hood, P. Zhang, J.L. Gong, Z.H. Nie, Asymmetric polymer-inorganic hybrid nanoparticles: synthesis, characterization and applications, *Nanoscale*, **2013**, 5, 5151-5166.

7. J. He, T. Babu, Y.J. Liu, P. Zhang, J.L. Gong, Z.H. Nie, Near-infrared light-responsive vesicles of Au nanoflowers , *Chem. Comm*. **2013**, 49, 576-578

8. J. He, Y.J. Liu, T. Babu, Z.J. Wei, Z.H. Nie, Self-assembly of inorganic nanoparticle vesicles and tubules driven by tethered linear block copolymers, *J. Am. Chem. Soc.* **2012**, 134, 11342−11345.

9. J. He, M. T. Perez, Y.J. Liu, P. Zhang, J.L. Gong, Z.H. Nie, A general approach to synthesize asymmetric hybrid nanoparticles by interfacial reactions, *J. Am. Chem. Soc.* **2012**, 134, 3639−3642.

10. J. He, B. Y. Yu, M. J. Hourwitz, Y.J. Liu, M. T. Perez, J.Yang, Z.H. Nie*, Wet-chemical synthesis of amphiphilic rodlike silica particles and their molecular-mimetic assembly in selective solvents, *Angew. Chem. Int. Ed*. **2012**, 51, 3628 –3633.

11. J. He, M.J. Hourwitz, Y.J. Liu, M. T. Perez, Z.H. Nie, One-pot facile synthesis of Janus particles with tailored shape and functionality, *Chem Comm*. **2011**,47, 12450-

12452.

12. H. Ma, M. Zhang, R. Huang. Y. Zhao, H. Yang, Y.J. Liu, X.C. Weng, Y. Zhou, M.G. Deng. L. Xu, X. Zhou, Pyridyl-substituted corrole isomers: synthesis and their regulation to G-quadruplex structures, *Chem. Asian J.* **2010**, 5, 114 – 122

References

(1) Whitesides, G. M.; Grzybowski, B. *Science* **2002**, *295*, 2418.

(2) Service, R. F. *Science (New York, N.Y.)* **2005**, *309*, 95.

(3) Kotov, N.; Weiss, P. *Acs Nano* **2014**, *8*, 3103

(4) Fahy, E.; Subramaniam, S.; Murphy, R. C.; Nishijima, M.; Raetz, C. R.; Shimizu, T.; Spener, F.; van Meer, G.; Wakelam, M. J.; Dennis, E. A. *J. Lipid Res.* **2009**, *50*, S9.

(5) Mashaghi, S.; Jadidi, T.; Koenderink, G.; Mashaghi, A. *Int. J. Mol. Sci.* **2013**, *14*, 4242.

(6) Subramaniam, S.; Fahy, E.; Gupta, S.; Sud, M.; Byrnes, R. W.; Cotter, D.; Dinasarapu, A. R.; Maurya, M. R. *Chem. Rev.* **2011**, *111*, 6452.

(7) Israelachvili, J. N.; Mitchell, D. J.; Ninham, B. W. *J. Chem. Soc. Faraday Trans.* **1976**, *72*, 1525.

(8) Israelachvili, J. N.; Mitchell, D. J.; Ninham, B. W. *Biochim. Biophys. Acta.* **1977**, *470*, 185.

(9) Hocine, S.; Li, M.-H. *Soft Matter* **2013**, *9*, 5839.

(10) Mai, Y.; Eisenberg, A. *Chem. Soc. Rev.* **2012**, *41*, 5969.

(11) Zhang, L. F.; Eisenberg, A. *J. Am. Chem. Soc.* **1996**, *118*, 3168.

(12) Hawker, C. J.; Wooley, K. L. *Science* **2005**, *309*, 1200.

(13) Cui, H.; Chen, Z.; Zhong, S.; Wooley, K. L.; Pochan, D. J. *Science* **2007**, *317*, 647.

(14) Blokzijl, W.; Engberts, J. *Angew. Chem. Int. Edit.* **1993**, *32*, 1545.

(15) Atkins, P. W.; De Paula, J. *Atkins' Physical chemistry*; W.H. Freeman: New York, **2006**.

(16) Israelachvili, J. N. *Intermolecular and surface forces*; Academic: San Diego, Calif.; London, **2003**.

(17) Jwleung Wikipedia, **2008**. https://commons.wikimedia.org/wiki/File:HydrophobicOrdering.jpg

(18) Jwleung Wikipedia, **2008**. https://commons.wikimedia.org/wiki/File:Micelles.jpg

(19) Meyers, D. *Surfaces, interfaces, and colloids : principles and applications*; VCH Publishers: New York, N.Y., **1991**.

(20) Bhargava, P.; Zheng, J. X.; Li, P.; Quirk, R. P.; Harris, F. W.; Cheng, S. Z. D. *Macromolecules* **2006**, *39*, 4880.

(21) Yu, Y. S.; Zhang, L. F.; Eisenberg, A. *Macromolecules* **1998**, *31*, 1144.

(22) Nie, Z.; Petukhova, A.; Kumacheva, E. *Nat. Nanotechnol.* **2010**, *5*, 15.

(23) Caswell, K. K.; Wilson, J. N.; Bunz, U. H. F.; Murphy, C. J. *J. Am. Chem. Soc.* **2003**, *125*, 13914.

(24) D. Howes, P.; Rana, S.; M. Stevens, M. *Chem. Soc. Rev.* **2014**, *43*, 3835.

(25) Hickey, R. J.; Koski, J.; Meng, X.; Riggleman, R. A.; Zhang, P.; Park, S.-J. *ACS Nano* **2013**, *8*, 495.

(26) Jain, P. K.; Eustis, S.; El-Sayed, M. A. *J. Phys. Chem. B.* **2006**, *110*, 18243.

(27) Choi, I.; Song, H. D.; Lee, S.; Yang, Y. I.; Kang, T.; Yi, J. *J. Am. Chem. Soc.* **2012**, *134*, 12083.

(28) Gandra, N.; Abbas, A.; Tian, L.; Singamaneni, S. *Nano Lett.* **2012**, *12*, 2645.

(29) Grzelczak, M.; Sánchez-Iglesias, A.; Mezerji, H. H.; Bals, S.; Pérez-Juste, J.; Liz-Marzán, L. M. *Nano Lett.* **2012**, *12*, 4380.

(30) Li, H.; Kanaras, A. G.; Manna, L. *Acc. Chem. Res.* **2013**, *46*, 1387.

(31) Li, W.; Zhang, P.; Dai, M.; He, J.; Babu, T.; Xu, Y.-L.; Deng, R.; Liang, R.; Lu, M.-H.; Nie, Z.; Zhu, J. *Macromolecules* **2013**, *46*, 2241.

(32) Marek Grzelczak, J. V., Eric M. Furst, and Luis M. Liz-Marza´n *Acs Nano*

2009, *12*, 4380

(33) Ye, X.; Millan, J. A.; Engel, M.; Chen, J.; Diroll, B. T.; Glotzer, S. C.; Murray, C. B. *Nano Lett.* **2013**, *13*, 4980.

(34) Choueiri, R. M.; Klinkova, A.; Thérien-Aubin, H. s.; Rubinstein, M.; Kumacheva, E. *J. Am. Chem. Soc.* **2013**, *135*, 10262.

(35) Dreaden, E. C.; Alkilany, A. M.; Huang, X.; Murphy, C. J.; El-Sayed, M. A. *Chem. Soc. Rev.* **2012**, *41*, 2740.

(36) Doane, T. L.; Burda, C. *Chem. Soc. Rev.* **2012**, *41*, 2885.

(37) Xu, L.; Ma, W.; Wang, L.; Xu, C.; Kuang, H.; Kotov, N. A. *Chem. Soc. Rev.* **2013**, *42*, 3114.

(38) Phan-Quang, G. C.; Lee, H. K.; Phang, I. Y.; Ling, X. Y. *Angew. Chem. Int. Edit.* **2015**.

(39) Song, J.; Cheng, L.; Liu, A.; Yin, J.; Kuang, M.; Duan, H. *J. Am. Chem. Soc.* **2011**, *133*, 10760.

(40) Yang, F.; Jin, C.; Subedi, S.; Lee, C. L.; Wang, Q.; Jiang, Y.; Li, J.; Di, Y.; Fu, D. *Cancer Treat. Rev.* **2012**, *38*, 566.

(41) Zhang, Z.; Wang, J.; Chen, C. *Theranostics* **2013**, *3*, 223.

(42) Song, J.; Zhou, J.; Duan, H. *J. Am. Chem. Soc.* **2012**, *134*, 13458.

(43) Liu, Y.; Liu, Y.; Yin, J.-J.; Nie, Z. *Macromol. Rapid Commun.* **2015**, *36*, 711-25.

(44) Xu, M.; Wang, L. V. *Rev. Sci. Instrum.* **2006**, *77*, 041101.

(45) Lin, J.; Wang, S. J.; Huang, P.; Wang, Z.; Chen, S. H.; Niu, G.; Li, W. W.; He, J.; Cui, D. X.; Lu, G. M.; Chen, X. Y.; Nie, Z. H. *Acs Nano* **2013**, *7*, 5320.

(46) Willets, K. A. *Chem. Soc. Rev.* **2014**, *43*, 3854.

(47) Guerrini, L.; Graham, D. *Chem. Soc. Rev.* **2012**, *41*, 7085.

(48) Gong, J.; Li, G.; Tang, Z. *Nano Today* **2012**, *7*, 564.

(49) Lee, A.; Andrade, G. F. S.; Ahmed, A.; Souza, M. L.; Coombs, N.; Tumarkin, E.; Liu, K.; Gordon, R.; Brolo, A. G.; Kumacheva, E. *J. Am. Chem. Soc.* **2011**, *133*,

7563.

(50) Stewart, A. F.; Lee, A.; Ahmed, A.; Ip, S.; Kumacheva, E.; Walker, G. C. *Acs Nano* **2014**, *8*, 5462.

(51) Polavarapu, L.; Perez-Juste, J.; Xu, Q.-H.; Liz-Marzan, L. M. *J. Mater. Chem. C* **2014**, *2*, 7460.

(52) Liu, D.; Wang, Z.; Jin, A.; Huang, X.; Sun, X.; Wang, F.; Yan, Q.; Ge, S.; Xia, N.; Niu, G.; Liu, G.; Hight Walker, A. R.; Chen, X. *Angew. Chem. Int. Ed.* **2013**, *52*, 14065.

(53) Ye, E.; Win, Y.; Tan, H.R.; Lin, M.; Teng, C.P.; Mlayah, A.; Han, M.Y.; *J. Am. Chem. Soc.*, **2011**, *133*, 8506–8509

(54) Nam, J.; Won, N.; Jin, H.; Chung, H.; Kim, S. *J. Am. Chem. Soc.* **2009**, *131*, 13639.

(55) Huang, P.; Lin, J.; Li, W.; Rong, P.; Wang, Z.; Wang, S.; Wang, X.; Sun, X.; Aronova, M.; Niu, G.; Leapman, R. D.; Nie, Z.; Chen, X. *Angew. Chem. Int. Ed.* **2013**, *52*, 13958.

(56) Song, J.; Pu, L.; Zhou, J.; Duan, B.; Duan, H. *Acs Nano* **2013**, *7*, 9947.

(57) Arruebo, M.; Fernández-Pacheco, R.; Ibarra, M. R.; Santamaría, J. *Nano Today* **2007**, *2*, 22.

(58) Perez, J. M.; O'Loughin, T.; Simeone, F. J.; Weissleder, R.; Josephson, L. *J. Am. Chem. Soc.* **2002**, *124*, 2856.

(59) Lee, N.; Hyeon, T. *Chem. Soc. Rev.* **2012**, *41*. 2575

(60) Hickey, R. J.; Haynes, A. S.; Kikkawa, J. M.; Park, S.-J. *J. Am. Chem. Soc.* **2011**, *133*, 1517.

(61) Lee, N.; Hyeon, T. *Chem. Soc. Rev.* **2012**, *41*, 2575.

(62) Xi, C.; Facal, P. M.; Xia, H.; Wang, D. *Soft Matter* **2015**.

(63) Jaganathan, H.; Ivanisevic, A. *J. Mater. Chem.* **2011**, *21*, 939.

(64) Serantes, D.; Simeonidis, K.; Angelakeris, M.; Chubykalo-Fesenko, O.; Marciello, M.; Morales, M. d. P.; Baldomir, D.; Martinez-Boubeta, C. *J. Phys. Chem. C* **2014**, *118*, 5927.

(65) Wang, H.; Mararenko, A.; Cao, G.; Gai, Z.; Hong, K.; Banerjee, P.; Zhou, S.

ACS Appl. Mater. Interfaces **2014**, *6*, 15309.

(66) Nakata, K.; Hu, Y.; Uzun, O.; Bakr, O.; Stellacci, F. *Adv. Mater.* **2008**, *20*, 4294.

(67) Gao, B.; Arya, G.; Tao, A. R. *Nat. Nanotechnol.* **2012**, *7*, 433.

(68) Gao, B.; Rozin, M. J.; Tao, A. R. *Nanoscale* **2013**, *5*, 5677.

(69) He, J.; Liu, Y.; Hood, T. C.; Zhang, P.; Gong, J.; Nie, Z. *Nanoscale* **2013**, *5*, 5151.

(70) Liu, K.; Zhao, N. N.; Kumacheva, E. *Chem. Soc. Rev.* **2011**, *40*, 656.

(71) Kao, J.; Thorkelsson, K.; Bai, P.; Rancatore, B. J.; Xu, T. *Chem. Soc. Rev.* **2013**, *42*, 2654.

(72) Willets, K. A.; Duyne, R. P. *Annu. Rev. Phys. Chem.* **2007**, *58*, 267.

(73) Ribeiro, T.; Prazeres, T. J. V.; Moffitt, M.; Farinha, J. P. S. *J. Phys. Chem. C* **2013**, *117*, 3122.

(74) Hardman, R. *Environ. Health Perspect.* **2006**, *114*, 165.

(75) Moffitt, M. *J. Phys. Chem. Lett.* **2013**, *4*, 3654.

(76) He, J.; Huang, X.; Li, Y.-C.; Liu, Y.; Babu, T.; Aronova, M. A.; Wang, S.; Lu, Z.; Chen, X.; Nie, Z. *J. Am. Chem. Soc.* **2013**, *135*, 7974.

(77) Nie, Z.; Fava, D.; Kumacheva, E.; Zou, S.; Walker, G. C.; Rubinstein, M. *Nat. Mater.* **2007**, *6*, 609.

(78) He, J.; Liu, Y.; Babu, T.; Wei, Z.; Nie, Z. *J. Am. Chem. Soc.* **2012**, *134*, 11342.

(79) He, J.; Wei, Z. J.; Wang, L.; Tomova, Z.; Babu, T.; Wang, C. Y.; Han, X. J.; Fourkas, J. T.; Nie, Z. H. *Angew. Chem. Int. Ed.* **2013**, *52*, 2463.

(80) Guo, Y.; Harirchian-Saei, S.; Izumi, C. M. S.; Moffitt, M. G. *Acs Nano* **2011**, *5*, 3309.

(81) Hu, J.; Wu, T.; Zhang, G.; Liu, S. *J. Am. Chem. Soc.* **2012**, *134*, 7624.

(82) He, J.; Zhang, P.; Babu, T.; Liu, Y.; Gong, J.; Nie, Z. *Chem. Commun.* **2013**, *49*, 576.

(83) Min, Y. J.; Akbulut, M.; Kristiansen, K.; Golan, Y.; Israelachvili, J. *Nat. Mater.* **2008**, *7*, 527.

(84) Nie, Z. H.; Fava, D.; Rubinstein, M.; Kumacheva, E. *J. Am. Chem. Soc.* **2008**, *130*, 3683.

(85) Fava, D.; Nie, Z.; Winnik, M. A.; Kumacheva, E. *Adv. Mater.* **2008**, *20*, 4318.

(86) Liu, K.; Lukach, A.; Thérien-Aubin, H.; Kumacheva. E.; *Angew. Chem. Int. Ed.* **2014**, *53*, 2648–2653

(87) Nie, Z.; Fava, D.; Kumacheva, E.; Zou, S.; Walker, G. C.; Rubinstein, M. *Nat. Mater.* **2007**, *6*, 609.

(88) Nikolic, M. S.; Olsson, C.; Salcher, A.; Kornowski, A.; Rank, A.; Schubert, R.; Frömsdorf, A.; Weller, H.; Förster, S. *Angew. Chem. Int. Ed.* **2009**, *48*, 2752.

(89) Yu, X.; Zhong, S.; Li, X.; Tu, Y.; Yang, S.; Van Horn, R. M.; Ni, C.; Pochan, D. J.; Quirk, R. P.; Wesdemiotis, C.; Zhang, W.-B.; Cheng, S. Z. D. *J. Am. Chem. Soc.* **2010**, *132*, 16741.

(90) Yu, X.; Zhang, W.-B.; Yue, K.; Li, X.; Liu, H.; Xin, Y.; Wang, C.-L.; Wesdemiotis, C.; Cheng, S. Z. D. *J. Am. Chem. Soc.* **2012**, *134*, 7780.

(91) Wang, B.; Li, B.; Dong, B.; Zhao, B.; Li, C. Y. *Macromolecules* **2010**, *43*, 9234.

(92) He, J.; Babu, T.; Liu, Y.; Zhang, P.; Gong, J.; Nie, Z.; *Chem. Comm*. **2013**, *49*, 576-578

(93) Zubarev, E. R.; Xu, J.; Sayyad, A.; Gibson, J. D. *J. Am. Chem. Soc.* **2006**, *128*, 15098.

(94) He, J.; Wang, L.; Wei, Z.; Yang, Y.; Wang, C.; Han, X.; Nie, Z. *ACS Appl. Mater. Interfaces* **2013**, *5*, 9746.

(95) Zhang, Z.; Ma, R.; Shi, L. *Acc. Chem. Res.* **2014**, *47*, 1426.

(96) Wang, H.; Song, X.; Liu, C.; He, J.; Chong, W. H.; Chen, H. *ACS Nano* **2014**, *8*, 8063.

(97) Cai, C.; Li, Y.; Lin, J.; Wang, L.; Lin, S.; Wang, X.-S.; Jiang, T. *Angew. Chem. Int. Ed.* **2013**, *52*, 7732.

(98) Xu, X.; Yuan, H.; Chang, J.; He, B.; Gu, Z. *Angew. Chem. Int. Ed.* **2012**, *51*,

3130.

(99) Liu, Y.; Li, Y.; He, J.; Duelge, K. J.; Lu, Z.; Nie, Z. *J. Am. Chem. Soc.* **2014**, *136*, 2602.

(100) Mai, Y.; Eisenberg, A. *J. Am. Chem. Soc.* **2010**, *132*, 10078.

(101) Urban, A. S.; Shen, X.; Wang, Y.; Large, N.; Wang, H.; Knight, M. W.; Nordlander, P.; Chen, H.; Halas, N. J. *Nano Lett.* **2013**, *13*, 4399.

(102) Chen, H. Y.; Abraham, S.; Mendenhall, J.; Delamarre, S. C.; Smith, K.; Kim, I.; Batt, C. A. *ChemPhysChem.* **2008**, *9*, 388.

(103) Moffitt, M.; Vali, H.; Eisenberg, A. *Chem, Mater.* **1998**, *10*, 1021.

(104) Mai, Y. Y.; Eisenberg, A. *Macromolecules* **2011**, *44*, 3179.

(105) Mai, Y. Y.; Eisenberg, A. *Acc. Chem. Res.* **2012**, *45*, 1657.

(106) Zhu, J.; Hayward, R. C. *J. Am. Chem. Soc.* **2008**, *130*, 7496.

(107) Park, J.; An, K.; Hwang, Y.; Park, J.-G.; Noh, H.-J.; Kim, J.-Y.; Park, J.-H.; Hwang, N.-M.; Hyeon, T. *Nat. Mater.* **2004**, *3*, 891.

(108) Dabbousi, B. O.; Rodriguez-Viejo, J.; Mikulec, F. V.; Heine, J. R.; Mattoussi, H.; Ober, R.; Jensen, K. F.; Bawendi, M. G. *J. Phy. Chem. B* **1997**, *101*, 9463.

(109) Kang, Y.; Taton, T. A. *Angew. Chem. Int. Ed.* **2005**, *44*, 409.

(110) Kang, Y.; Taton, T. A. *Macromolecules* **2005**, *38*, 6115.

(111) Li, W.; Liu, S.; Deng, R.; Wang, J.; Nie, Z.; Zhu, J. *Macromolecules* **2013**, *46*, 2282.

(112) Sanchez-Gaytan, B. L.; Cui, W.; Kim, Y.; Mendez-Polanco, M. A.; Duncan, T. V.; Fryd, M.; Wayland, B. B.; Park, S.-J. *Angew. Chem. Int. Ed.* **2007**, *46*, 9235.

(113) Chen, T.; Yang, M.; Wang, X.; Tan, L. H.; Chen, H. *J. Am. Chem. Soc.* **2008**, *130*, 11858.

(114) Wang, H.; Chen, L.; Shen, X.; Zhu, L.; He, J.; Chen, H. *Angew. Chem. Int. Ed.* **2012**, *51*, 8021.

(115) Xu, J.; Wang, H.; Liu, C.; Yang, Y.; Chen, T.; Wang, Y.; Wang, F.; Liu, X.; Xing, B.; Chen, H. *J. Am. Chem. Soc.* **2010**, *132*, 11920.

(116) Gao, X. H.; Cui, Y. Y.; Levenson, R. M.; Chung, L. W. K.; Nie, S. M. *Nat. Biotechnol.* **2004**, *22*, 969.

(117) Sung, J.; Jo, P. S.; Shin, H.; Huh, J.; Min, B. G.; Kim, D. H.; Park, C. *Adv. Mater.* **2008**, *20*, 1505.

(118) Zhang, H.; Liu, Y.; Yao, D.; Yang, B. *Chem. Soc. Rev.* **2012**, *41*, 6066

(119) Lin, S.; Li, M.; Dujardin, E.; Girard, C.; Mann, S. *Adv. Mater.* **2005**, *17*, 2553.

(120) Ghosh, S. K.; Pal, T. *Chem. Rev.* **2007**, *107*, 4797.

(121) Wang, L.; Zhu, Y.; Xu, L.; Chen, W.; Kuang, H.; Liu, L.; Agarwal, A.; Xu, C.; Kotov, N. A. *Angew. Chem. Int. Ed.* **2010**, *49*, 5472.

(122) Klinkova, A.; Thérien-Aubin, H.; Ahmed, A.; Nykypanchuk, D.; Choueiri, R. M.; Gagnon, B.; Muntyanu, A.; Gang, O.; Walker, G. C.; Kumacheva, E. *Nano Lett.* **2014**, *14*, 6314.

(123) Chen, G.; Wang, Y.; Yang, M.; Xu, J.; Goh, S. J.; Pan, M.; Chen, H. *J. Am. Chem. Soc.* **2010**, *132*, 3644.

(124) Jana, N. R.; Gearheart, L.; Murphy, C. J. *Langmuir* **2001**, *17*, 6782.

(125) Li, J.; Stoliarov, S. I. *Polym. Degrad. Stab.* **2014**, *106*, 2.

(126) Li, J.; Gong, J.; Stoliarov, S. I. *Int. J. Heat Mass Transfer* **2014**, *77*, 738.

(127) Li, J.; Stoliarov, S. I. *Combust. Flame* **2013**, *160*, 1287.

(128) Mhike, W.; Ferreira, I. V. W.; Li, J.; Stoliarov, S. I.; Focke, W. W. *J. Appl. Polym. Sci.* 2015, *132*,

(129) Yang, M.; Chen, G.; Zhao, Y.; Silber, G.; Wang, Y.; Xing, S.; Han, Y.; Chen, H. *Phys. Chem. Chem. Phys.* 2010, *12*, 11850.

(130) Zhang, H.; Wang, D. *Angew. Chem. Int. Ed.* **2008**, *120*, 4048.

(131) Critchfield, F. E.; Gibson, J. A.; Hall, J. L *J. Am. Chem. Soc.* **1953**, *75*, 6044.

(132) Rubinstein, M.; Colby, R. H. *Polymer physics*; Oxford University Press: Oxford; New York, **2003**.

(133) Rasband, W.S., ImageJ, U. S. National Institutes of Health, Bethesda, Maryland, USA, http://imagej.nih.gov/ij/, 1997-2014.

(134) Subramaniam, A. B.; Guidotti, G.; Manoharan, V. N.; Stone, H. A. *Nat. Mater.* **2013**, *12*, 128.

(135) Discher, D. E.; Eisenberg, A. *Science* **2002**, *297*, 967.

(136) Zhang, X.; Wang, C. *Chem. Soc. Rev.* **2011**, *40*, 94.

(137) Zhang, S. G. *Nat. Biotechnol.* **2003**, *21*, 1171.

(138) Lee, J.; Hernandez, P.; Lee, J.; Govorov, A. O.; Kotov, N. A. *Nat. Mater.* **2007**, *6*, 291.

(139) Huynh, W. U.; Dittmer, J. J.; Alivisatos, A. P. *Science* **2002**, *295*, 2425.

(140) Maier, S. A.; Kik, P. G.; Atwater, H. A.; Meltzer, S.; Harel, E.; Koel, B. E.; Requicha, A. A. G. *Nat. Mater.* **2003**, *2*, 229

(141) Zheng, R..; Liu, G.; Yan, X.; *J. Am. Chem. Soc.* **2005**, *127*, 15358.

(142) Christian, D. A.; Tian, A.; Ellenbroek, W. G.; Levental, I.; Rajagopal, K.; Janmey, P. A.; Liu, A. J.; Baumgart, T.; Discher, D. E. *Nat. Mater.* **2009**, *8*, 843.

(143) Groeschel, A. H.; Schacher, F. H.; Schmalz, H.; Borisov, O. V.; Zhulina, E. B.; Walther, A.; Mueller, A. H. E. *Nat. Commun.* **2012**, *3*.

(144) Rupar, P. A.; Chabanne, L.; Winnik, M. A.; Manners, I. *Science* **2012**, *337*, 559.

(145) Glotzer, S. C.; Solomon, M. J. *Nat. Mater.* **2007**, *6*, 557.

(146) Shields Iv, C. W.; Zhu, S.; Yang, Y.; Bharti, B.; Liu, J.; Yellen, B. B.; Velev, O. D.; Lopez, G. P. *Soft Matter* **2013**, *9*, 9219.

(147) Sacanna, S.; Irvine, W. T. M.; Chaikin, P. M.; Pine, D. J. *Nature* **2010**, *464*, 575

(148) Frens.G *nature physical science* **1973**, *241*, 20.

(149) Groot, R. D.; Warren, P. B. *J. Chem. Phys.* **1997**, *107*, 4423.

(150) Espanol, P.; Warren, P. *Europhys Lett.* **1995**, *30*, 191.

(151) Zhu, Y. L.; Liu, H.; Li, Z. W.; Qian, H. J.; Milano, G.; Lu, Z. Y. *J. Comput. Chem.* **2013**, *34*, 2197.

(152) Koutsos, V.; vanderVegte, E. W.; Pelletier, E.; Stamouli, A.; Hadziioannou, G.

Macromolecules **1997**, *30*, 4719.

(153) Zhu, J.; Zhang, S.; Zhang, K.; Wang, X.; Mays, J. W.; Wooley, K. L.; Pochan, D. J. *Nat. Commun.* **2013**, *4*.

(154) Hu, J.; Weikl, T. R.; Lipowsky, R. *Soft Matter* **2011**, *7*, 6092.

(155) Qian, H. J.; Lu, Z. Y.; Chen, L. J.; Li, Z. S.; Sun, C. C. *Macromolecules* **2005**, *38*, 1395.

(156) Pons-Siepermann, I. C.; Glotzer, S. C. *Soft Matter* **2012**, *8*, 6226.

(157) Swierczewska, M.; Liu, G.; Lee, S.; Chen, X. Y. *Chem. Soc. .Rev.* **2012**, *41*, 2641.

(158) Chen, J.; Yang, M.; Zhang, Q.; Cho, E. C.; Cobley, C. M.; Kim, C.; Glaus, C.; Wang, L. V.; Welch, M. J.; Xia, Y. *Adv. Funct. Mater.* **2010**, *20*, 3684.

(159) Kim, K. T.; Cornelissen, J. J. L. M.; Nolte, R. J. M.; van Hest, J. C. M. *Adv. Mater.* **2009**, *21*, 2787.

(160) Soukoulis, C. M.; Linden, S.; Wegener, M. *Science* **2007**, *315*, 47.

(161) Mueller, W.; Koynov, K.; Fischer, K.; Hartmann, S.; Pierrat, S.; Basché, T.; Maskos, M. *Macromolecules* **2008**, *42*, 357.

(162) Sanson, C.; Diou, O.; Thévenot, J.; Ibarboure, E.; Soum, A.; Brûlet, A.; Miraux, S.; Thiaudière, E.; Tan, S.; Brisson, A.; Dupuis, V.; Sandre, O.; Lecommandoux, S. *ACS Nano* **2011**, *5*, 1122.

(163) Jin, Y.; Jia, C.; Huang, S.-W.; O'Donnell, M.; Gao, X. *Nat. Commun.* **2010**, *1*, 41.

(164) Wu, C.-H.; Cook, J.; Emelianov, S.; Sokolov, K. *Adv. Funct. Mater.* **2014**, *24*, 6862.

(165) Fenske, M. T.; Meyer-Zaika, W.; Korth, H.-G.; Vieker, H.; Turchanin, A.; Schmuck, C. *J. Am. Chem. Soc.* **2013**, *135*, 8342.

(166) Liu, Y.; Liu, B.; Nie, Z. *Nano Today*. **2015**, 136, 2602-2610

(167) Azzam, T.; Eisenberg, A. *Langmuir* **2010**, *26*, 10513.

(168) Zhang, T.; Ge, J.; Hu, Y.; Yin, Y. *Nano Lett.* **2007**, *7*, 3203.

(169) Fu, A.; Wilson, R. J.; Smith, B. R.; Mullenix, J.; Earhart, C.; Akin, D.;

Guccione, S.; Wang, S. X.; Gambhir, S. S. *ACS Nano* **2012**, *6*, 6862.

(170) O'Grady, K. *J. Phys. D-Appl. Phys.* **2009**, *42*.

(171) Gao, W.; Kagan, D.; Pak, O. S.; Clawson, C.; Campuzano, S.; Chuluun-Erdene, E.; Shipton, E.; Fullerton, E. E.; Zhang, L.; Lauga, E.; Wang, J. *Small* **2012**, *8*, 460.

(172) Kagan, D.; Laocharoensuk, R.; Zimmerman, M.; Clawson, C.; Balasubramanian, S.; Kang, D.; Bishop, D.; Sattayasamitsathit, S.; Zhang, L.; Wang, J. *Small* **2010**, *6*, 2741.

(173) Balasubramanian, S.; Kagan, D.; Jack Hu, C.-M.; Campuzano, S.; Lobo-Castañon, M. J.; Lim, N.; Kang, D. Y.; Zimmerman, M.; Zhang, L.; Wang, J. *Angew. Chem. Int. Edit.* **2011**, *123*, 4247.

(174) Campuzano, S.; Orozco, J.; Kagan, D.; Guix, M.; Gao, W.; Sattayasamitsathit, S.; Claussen, J. C.; Merkoçi, A.; Wang, J. *Nano Lett.* **2011**, *12*, 396.

(175) Kagan, D.; Campuzano, S.; Balasubramanian, S.; Kuralay, F.; Flechsig, G.-U.; Wang, J. *Nano Lett.* **2011**, *11*, 2083.

(176) Manesh, K. M.; Campuzano, S.; Gao, W.; Lobo-Castanon, M. J.; Shitanda, I.; Kiantaj, K.; Wang, J. *Nanoscale* **2013**, *5*, 1310.

(177) Gao, W.; Feng, X.; Pei, A.; Gu, Y.; Li, J.; Wang, J. *Nanoscale* **2013**, *5*, 4696.

(178) Ismagilov, R. F.; Schwartz, A.; Bowden, N.; Whitesides, G. M. *Angew. Chem. Int. Edit.* **2002**, *41*, 652.

(179) Kline, T. R.; Paxton, W. F.; Mallouk, T. E.; Sen, A. *Angew. Chem. Int. Edit.* **2005**, *44*, 744.

(180) Paxton, W. F.; Kistler, K. C.; Olmeda, C. C.; Sen, A.; St. Angelo, S. K.; Cao, Y.; Mallouk, T. E.; Lammert, P. E.; Crespi, V. H. *J. Am. Chem. Soc.* **2004**, *126*, 13424.

(181) Kovtyukhova, N. I. *J. Phys. Chem. C* **2008**, *112*, 6049.

(182) Fournier-Bidoz, S.; Arsenault, A. C.; Manners, I.; Ozin, G. A. *Chem. Commun.* **2005**, *41*, 441.

(183) Wu, Z.; Wu, Y.; He, W.; Lin, X.; Sun, J.; He, Q. *Angew. Chem. Int. Edit.* **2013**, *52*, 7000.

(184) Wu, Y.; Wu, Z.; Lin, X.; He, Q.; Li, J. *ACS Nano* **2012**, *6*, 10910.

(185) Sánchez, S.; Pumera, M. *Chem. Asian J.* **2009**, *4*, 1402.

(186) Dhar, P.; Fischer, T. M.; Wang, Y.; Mallouk, T. E.; Paxton, W. F.; Sen, A. *Nano Lett.* **2005**, *6*, 66.

(187) Laocharoensuk, R.; Burdick, J.; Wang, J. *ACS Nano* **2008**, *2*, 1069.

(188) Demirok, U. K.; Laocharoensuk, R.; Manesh, K. M.; Wang, J. *Angew. Chem. Int. Edit.* **2008**, *120*, 9489.

(189) Sundararajan, S.; Lammert, P. E.; Zudans, A. W.; Crespi, V. H.; Sen, A. *Nano Lett.* **2008**, *8*, 1271.

(190) Thakur, S.; Kapral, R. *J. Chem. Phys.* **2011**, *135*. 024509

(191) Wilson, D. A.; de Nijs, B.; van Blaaderen, A.; Nolte, R. J. M.; van Hest, J. C. M. *Nanoscale* **2013**, *5*, 1315.

(192) Lecault, V.; VanInsberghe, M.; Sekulovic, S.; Knapp, D. J. H. F.; Wohrer, S.; Bowden, W.; Viel, F.; McLaughlin, T.; Jarandehei, A.; Miller, M.; Falconnet, D.; White, A. K.; Kent, D. G.; Copley, M. R.; Taghipour, F.; Eaves, C. J.; Humphries, R. K.; Piret, J. M.; Hansen, C. L. *Nat. Methods* **2011**, *8*, 581.

(193) Choi, N. W.; Cabodi, M.; Held, B.; Gleghorn, J. P.; Bonassar, L. J.; Stroock, A. D. *Nat. Materials* **2007**, *6*, 908.

(194) Skelley, A. M.; Kirak, O.; Suh, H.; Jaenisch, R.; Voldman, J. *Nat. Methods* **2009**, *6*, 147.

(195) Whitesides, G. M. *Nature* **2006**, *442*, 368.

(196) Perrault, S. D.; Chan, W. C. W., *J. Am. Chem. Soc.* **2009**, *131*, 17042

(197) Xia, Y. N.; Whitesides, G. M. *Angew. Chem. Int. Edit.* **1998**, *37*, 551.

(198) Ye, X. C.; Zheng, C.; Chen, J.; Gao, Y. Z.; Murray, C. B. *Nano. Lett.* **2013**, *13*, 765.

(199) Herricks, T.; Chen, J. Y.; Xia, Y. N. *Nano. Lett.* **2004**, *4*, 2367.

(200) Squires, T. M.; Quake, S. R. *Rev. mod. Phys.* **2005**, *77*, 977.

(201) Jahn, A.; Stavis, S. M.; Hong, J. S.; Vreeland, W. N.; DeVoe, D. L.; Gaitan,

M. *ACS nano* **2010**, *4*, 2077.

(202) Karnik, R.; Gu, F.; Basto, P.; Cannizzaro, C.; Dean, L.; Kyei-Manu, W.; Langer, R.; Farokhzad, O. C. *Nano. Lett.* **2008**, *8*, 2906.

(203) Kotov, N. A. *Science* **2010**, *330*, 188.

(204) Sims, P. A.; Greenleaf, W. J.; Duan, H.; Xie, X. S. *Nat. Methods* **2011**, *8*, 575

(205) Wang, Y.; Wang, Y.; Breed, D. R.; Manoharan, V. N.; Feng, L.; Hollingsworth, A. D.; Weck, M.; Pine, D. J. *Nature* **2012**, *491*, 51.

(206) Cabral, H; Matsumoto, Y; Mizuno, K; Chen, Q; Murakami, M; Kimura, M; Terada, Y; Kano, M. R.; Miyazono, K; Uesaka, M; Nishiyama, N; Kataoka, K *Nat. Nanotechnol.* **2011**, *6*, 815.

(207) Niikura, K.; Iyo, N.; Higuchi, T.; Nishio, T.; Jinnai, H.; Fujitani, N.; Ijiro, K. *J. Am. Chem. Soc.* **2012**, *134*, 7632.